NTNU – Trondheim
Norwegian University of
Science and Technology

Mechanical Properties of Gas Metal Arc and Friction Stir AA6082-T6 Weldments

Christina Rødsand Breivik

Materials Technology
Submission date: June 2013
Supervisor: Trond Furu, IMTE
Co-supervisor: Øystein Grong, IMT

Norwegian University of Science and Technology
Department of Materials Science and Engineering

Preface

The present report is part of an international collaboration project between Norway and Qatar, where the involved companies have been Hydro Aluminium, Qatar Petroleum and Qatalum.

The trip to Qatar in the beginning of the project was very informative and of great inspiration and motivation for the further work.

Supervisors and contacts during the work have been professor Øystein Grong [1] and Trond Furu[2]. I would like to give a special thanks to professor Øystein Grong for his thorough and constructive guidance. In addition, I would like to thank all the other individuals assisting me during the project.

Trondheim, June 2013

Christina Breivik

[1] Norwegian University of Science and Technology (NTNU), Trondheim
[2] Hydro Aluminium, Sunndalsøra

Abstract

The general purpose of the presents report is to determine the mechanical properties of AA6082-T6 subsequent to gas metal arc welding (GMAW) and friction stir welding (FSW). Hardness testing has been carried out for the weldments. In addition, tensile and Charpy V-notch testing has been carried out for the unaffected base metal, the fusion/stir zone and for the heat-affected zone (HAZ), both transverse and longitudinal to the welding/extrusion direction.

It is concluded that HAZ softening is a major problem both in the GMA and the FS weldments. Still, the total width of the HAZ in the FS weldments is smaller compared to that observed in the GMA weldments. The total strength reduction for the GMA and the FS welds was 43 and 34%, respectively. The general observations is that the FS weldments show slightly better mechanical properties compared to the GMA weldments. This is further reflected in the calculations of load-bearing capacity of the joints, showing that the FS weldments exhibit the highest capacity under otherwise identical conditions due to the combined effect of a lower HAZ strength reduction and a smaller HAZ width.

Sammendrag

Det generelle formålet med denne rapporten er å bestemme de mekaniske egenskapene til AA6082-T6 påfølgende av gassveising (GMAW) og friksjonssveising (FSW). Det har blitt foretatt hardhetsmålinger langs den varmepåvirkede sonen (HAZ). I tillegg har strekk- og skårslagstesing blitt gjennomført for det upåvirkede grunnmaterialet, for smelte/røresone, og for HAZ. Prøvene har blitt tatt ut enten på tvers eller på langs av ektruderingsretningen.

Det har blitt konkludert med at HAZ mykning er et stor problem både ved GMAW og ved FSW. Likevel blir den totale bredden av HAZ mye smalere ved FSW sammenlignet med GMAW. Den totale styrkereduksjonen ved GMAW og FSW var henholdsvis på 43 og 34%. Generelt viser FS-sveisene bedre mekaniske egenskaper sammenlignet med GMA-sveisene. Dette støttes av beregningene gjort for lastbærenede kapasitet av sveisene, som viser at FS-sveisene har større kapasitet sammenlignet med GMA-sveisene under like forhold. Dette kan forklares med den kombinerte effekten av lavere HAZ styrkereduksjon og smalere bredde på HAZ.

Contents

Chapter 1

Introduction

The aluminium industry is the largest non-ferrous metal industry in the world economy. And despite lower tensile properties compared to steel, aluminium has an excellent specific strength (strength-to-weight ratio), which is an advantage in areas where weight is a limiting factor, i.e. within the transport industry [1, 2]. The mechanical properties of aluminium can be improved by adding elements such as magnesium (Mg) and silicon (Si). And the addition of these alloying elements increases the aluminium response to heat treatment due to formation of Mg_2Si intermetalllic compounds [3]. To exploit this advantage, precipitation hardening (also called age hardening) is commonly used to increase the product properties. And the improved properties make them more attractive, especially within the transport, offshore and automotive industries because they provide good strength and toughness in engineering applications, while maintaining the low density and high corrosion resistance of aluminium [4, 5].

Welding processes are essential for the manufacture of a wide variety of products (such as frames, pressure vessels, automotive components and any product which have to be produced by welding). But the material integrity of a welded component is always poorer than that of the parent material, and this may cause problems later in the production and the application process of the alloys [4, 6, 7].

One of the most common welding techniques applied to aluminium alloys is the gas metal arc welding (GMAW) process. It offers advantage of high welding speed with versatility and ability to make high quality welds. Many improvements have been made in the performance and reliability of the equipment for this process and, especially in power sources, some major advances have occurred in the past few years [8]. But still, there are many problems associated with fusion welding of the age hardening (Al-Mg-Si) aluminium alloys. The high coefficient of thermal expansion and solidification shrinkage, combined with a relatively wide solidification-temperature range, makes these alloys susceptible to weld cracking mechanisms like solidification cracking [9, 10] and liquation cracking [11, 12]. Also, the high solubility of hydrogen in molten aluminium can result in gas porosity [13]. In addition, the degree of the heat affected zone (HAZ) degrada-

tion for these alloys may differ significantly, depending on the alloy temper and the weld processing conditions [4].

In an attempt to eliminate some of the problems associated with fusion welding, a solid state welding technique called friction stir welding (FSW) has been developed. Since this technique does not involve melting, the problems associated with the fusion zone is eliminated. Instead, this zone is replaced by a thermo-mechanically affected zone (TMAZ) [5]. FSW is defined as both a deformation and a thermal process (even though there is no bulk fusion). And unlike fusion welding, FSW also involves extremely high shear strain and strain rates, which will have a profound influence on the development of microstructures [14]. Although, some problems may be reduced or even eliminated, HAZ softening due to reversion is still a major problem, particularly in FSW of peak-aged Al-Mg-Si alloys [5].

With main focus on AA6082-T6 (a medium-strength alloy with good chemical and physical properties), Hydro Aluminium has initiated a project to get a better understanding on how these alloys respond to welding. The extruded sheets used in the project are produced and provided by Hydro and welded either by gas metal arc welding (GMAW) or friction stir welding (FSW).

The general purpose of the present report is to obtain a better understanding of the mechanical properties of alloy 6082-T6 subsequent to friction stir and gas metal arc welding. A more extensive analysis, with respect to hardness, tensile and Charpy V-notch testing, is carried out. The microstructural features of the weldments are studied by optical microscope. And the fracture surfaces of the tested tensile and Charpy V-notch specimens are analyzed in an scanning electron microscope (SEM).

Chapter 2

Theory

In the following chapters an introduction to the properties of extruded and artificially aged Al-Mg-Si alloys is provided. There will be a review on welding of these alloys with respect to gas metal arc welding (GMAW) and friction stir welding (FSW). In addition, there will be a short presentation of the different zones in a welded component, with main focus on the mechanical degradation of the thermally and mechanically affected zones.

2.1 Physical metallurgy of Al-Mg-Si alloys

The unique physical and mechanical properties of the Al-Mg-Si alloys make them attractive for a wide range of structural applications, where a high specific strength (i.e., yield strength-to-density ratio) is required [15]. The main alloying elements, Mg and Si, have a significant solid solubility in aluminium. And as shown in Figure 2.1, the solubility increases with increasing temperature [4].

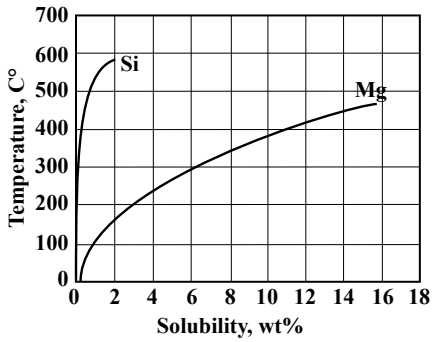

Figure 2.1: Equilibrium binary solid solubility of Mg and Si in aluminium as a function of temperature. Based on ideas of Davis and associates [4].

2.1.1 Process route

The Al-Mg-Si alloys are often used as extrusions, and the high solubility of the main alloying elements is fully utilized during solution heat-treatment, which is incorporated in the extrusion process. The process chain for production of extrusions of the Al-Mg-Si alloys is schematically shown in Figure 2.2. This process route is valid for all the heat-treatable Al-alloys.

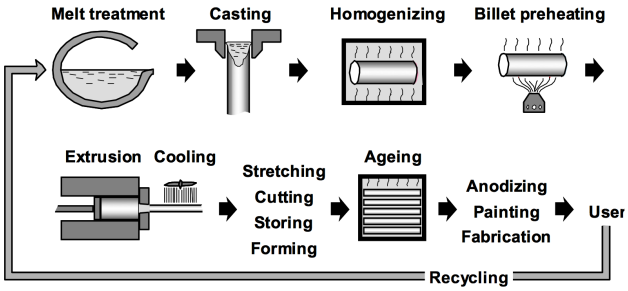

Figure 2.2: Sketch of the different process steps related to production of extrusions made from heat-treatable aluminium alloys [16].

Prior to the extrusion process (as the first step of the extrusion process), Mg and Si are introduced in the melt together with the other desirable alloying elements (that alter the alloy properties). The main alloying elements are partly dissolved in the primary α-Al matrix, and partly present in the form of intermetellic phases. And the relationship between these alloying elements, as shown in Figure 2.3, has a large influence on the amount of Mg_2Si (primary hardening phase) formed during the solidification process [17, 18].

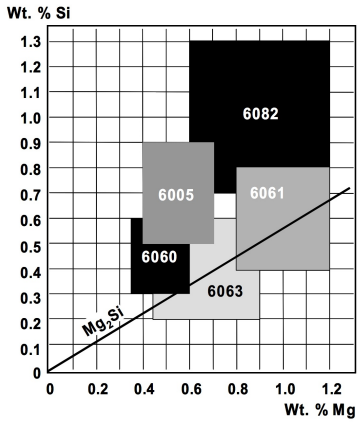

Figure 2.3: Variation of main alloying elements in different Al-Mg-Si alloys [16].

Fe is present as an impurity element in all commercial alloys, and in the casting process following the melt treatment, it may form a variety of binary and ternary intermetallic phases, such as Al-Fe and Al-Fe-Si, during solidification. In addition to intermetallic phases, the amount of Si that is not incorporated in the α-Al matrix or in the Al-Fe-Si intermetallic phases now combines with Mg to form Mg_2Si [17, 18].

After casting, the as-cast billets require a homogenization treatment to make the alloy suitable for hot extrusion. During this process, transformation of unfavorable intermetallic particles as well as dissolution of β-Mg_2Si take place. This action improves the ductility of the material and gives a maximum age hardening potential of the extruded product [19, 20].

The billets are further preheated, loaded into the extrusion chamber, and extruded through a die [21]. All the steps mentioned above have a profound influence on the nature of the intermetallic particle population, where type, size, morphology and distribution of the particles are important in determining the subsequent material properties [17]. These intermetallic phases can have a detrimental effect on the mechanical properties of the alloy, and must be controlled.

2.1.2 Grain structure and texture

Aluminium alloys can obtain different crystallographic texture depending on the process method, chemical composition and heat treatment. For instance, a fibrous grain structure can be retained by adding alloying elements that prevent recrystallization by the formation of dispersoids. For the 6xxx alloys, such as AA6082, coarser dispersoids are obtained by adding Mn. These particles will prevent recrystallization during hot working processes like extrusion [22].

The grain structure of the Al-Mg-Si alloys may be recrystallized, partly recrystallized or fibrous. And owing to the extrusion process, these alloys invariably exhibit strong crystallographic texture. The fibrous grain structure found in AA6082 gives higher strength compared to the recrystallized grain structure found in AA6063, which contains less/no Mn. The difference in grain structure between these alloys is shown in Figure 2.4.

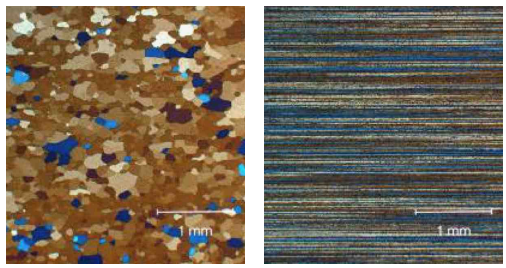

(a) Recrystallized **(b)** Non-recrystallized

Figure 2.4: Recrystallized and non-recrystallized grain structure: (a) AA6063 and (b) AA6082. (Extrusion direction is horizontal and thickness direction is vertical) [23].

The recrystallized alloys have cube texture as shown in Figure 2.4a, while in the non-recrystallized alloys a fibre texture is found, see Figure 2.4b.

2.1.3 Precipitation hardening

Precipitation hardening is often employed to the Al-Mg-Si alloys (either as a part of the extrusion process or as a separate process) to obtain better mechanical properties. As indicated in Figure 2.5, this process consist of [15, 24]:

1. *Solution heat treatment*. Heating to a prescribed elevated temperature (T_1) and soaking there for a described period of time.
2. *Quenching*. The alloy is cooled fast enough to retain the elevated temperature microstructure.
3. *Artificial aging*. The alloy is soaked at a lower temperature T_2 for a certain period of time.

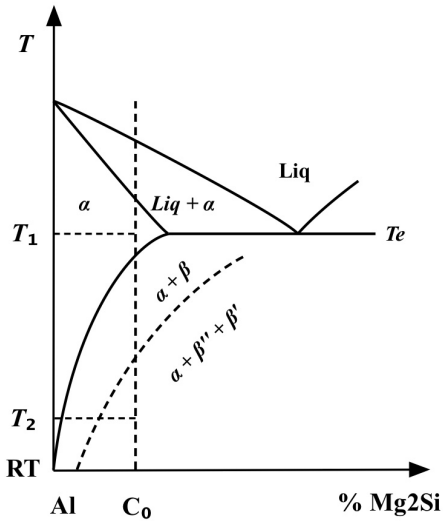

Figure 2.5: Quasi-binary section through the aluminium-rich corner of the ternary Al-Mg-Si phase diagram. Based on the ideas of Grong [5].

The solution heat treatment allows the alloying elements to form a solid solution with aluminium. And when the temperature is quickly reduced by quenching, a supersaturated solid solution is created. Artificial aging is then used to precipitate strengthening phases throughout the metal (in a controlled fashion) [4]. The precipitation sequence occurring during precipitation hardening can be summarized as follows [15, 25]:

$$ss \rightarrow GP1 \rightarrow \beta'' \rightarrow \beta'(Mg_2Si) \rightarrow \beta(Mg_2Si) \tag{2.1}$$

The most effective hardening phase, β'', are fully coherent, needle shaped precipitates lying along the $[100]_{Al}$ directions with a monoclinic crystallographic structure [26]. In addition to the fine β'' precipitates, the coarse rod-shaped β'-precipitates will also contribute to an increase in the strength.

The properties constantly evolve with ageing time at the ageing temperature. This can be seen from Figure 2.6, where strength and hardness increase with time to some peak values [24]. This condition is referred to as the peak-aged (T6) condition, where the base metal contains a mixture of the two metastable β'' and β' precipitates [5].

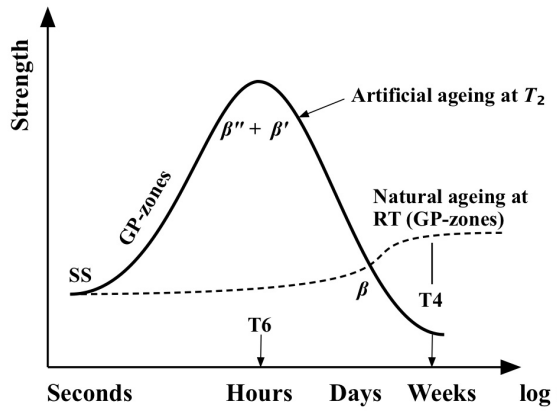

Figure 2.6: Strength evolution during artificial (and natural) ageing. Based on the ideas of Grong [5].

The resulting mechanical properties at room temperature are directly linked to the number density and size distribution of the hardening precipitates that form during artificial ageing [25]. Ageing causes precipitation within the grains, which results in an increase in strength and hardness, at the expense of ductility [24].

2.1.4 Fracture mechanisms/mechanical properties

Both chemistry and processing conditions will influence the microstructure of aluminium alloys, including constituent particles, dispersoids, amounts of elements in solid solution, age-hardening precipitates, grain size and texture [21]. Due to the complexity of the microstructure, a diversity of mechanisms for fracture can occur in the age hardening aluminium alloys. After precipitation hardening, the microstructure consists of grains with a high density of fine hardening precipitates formed homogeneously in the material during artificial ageing and lower density of larger intermetallic constituent particles [23].

Both the grain structure and the crystallographic texture can cause variation in the mechanical properties. And on a micro-scale, intermetallic constituent particles, dispersoids, precipitates and precipitate-free zones will contribute to an inhomogenous strain field and preferential fracture initiation and crack growth [23].

2.2 Gas Metal Arc Welding of Al-Mg-Si alloys

The majority of the heat-treatable aluminium alloys, like the Al-Mg-Si alloys, are easily welded by a wide variety of welding techniques. The primary methods for welding of aluminium alloys are the traditional arc welding processes, e.g. gas metal arc welding (GMAW) and gas tungsten arc welding (GTAW) [5, 27]. But despite the unique physical and chemical properties of the Al-Mg-Si alloys, application of welded components may be limited by cracking and degradation mechanisms [5].

2.2.1 The GMAW process

The GMAW process uses a metal wire as a combined electrode and filler metal in plasma arc of inert shielding gas, see Figure 2.7. Filler metal is added to the weld pool automatically and continuously. The melting electrode forms droplets, which are transferred through the arc to the pool. Electrical contact is established between the power source and the contact tube within the gas nozzle [28, 29].

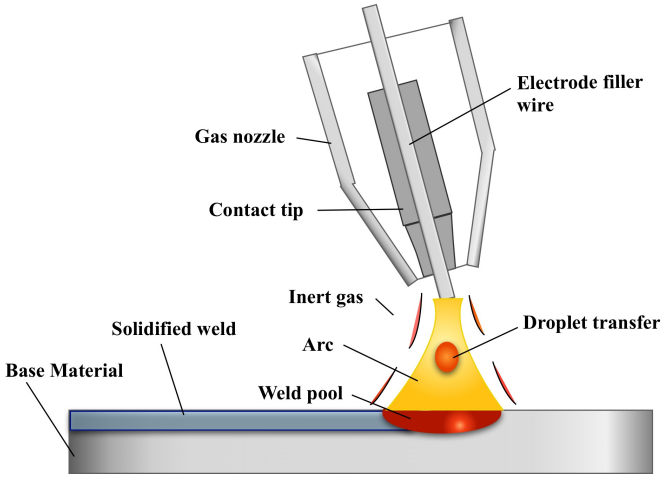

Figure 2.7: Sketch of the GMAW process. Based on the ideas of Myhr [28].

GMAW is the major high-speed production process for arc welding of aluminium. It uses positive electrode DC power, which gives it a continuous cleaning action and concentrates the arc to produce rapid melting. Because the electrode and the filler are the same, the process is a one-handed operation that is easily mechanized or adapted for robotic operations [4].

Fusion welding produces a locally modified microstructure and fluctuating mechanical properties. Different zones can be identified as a result of local alloy composition changes and/or the temperature cycle during welding. These zones are schematically shown in

Figure 2.8. Depending on the actual heat input and the geometry of the joint, the width of these zones can vary considerably [30].

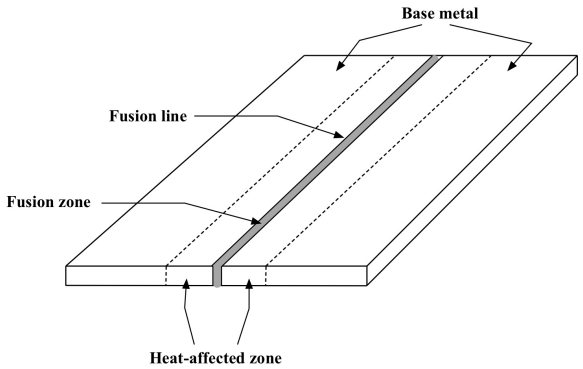

Figure 2.8: Sketch of the different zones, which form in a welded component.

Some microstructural features and degradation mechanisms for the most important zones in a welded component, as illustrated in Figure 2.8, will be presented in the following sub-chapters.

2.2.2 The fusion zone

In the fusion zone (FZ), as shown in Figure 2.9, the microstructure goes back to the as-cast state , which means that all memory of the past processing steps is lost [5]. In this zone, the microstructure depends on the solidification behavior of the weld pool, which controls the size and shape of the grains, segregation, and the distribution of inclusions and porosity [31].

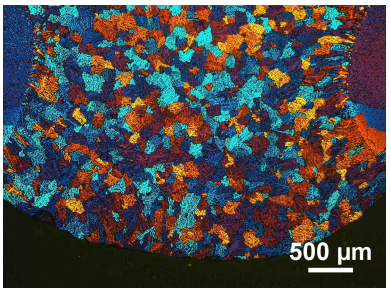

Figure 2.9: Optical micrograph showing the fusion zone of an aluminium alloy (welded with filler AA5183).

Fusion welding of aluminium alloys leads to melting and re-solidification of the fusion zone, which results in the formation of brittle inter-dendritic structure and eutectic phases.

The formation of brittle structure in the weld zone leads to the drastic decrease in the mechanical properties like hardness, strength and ductility [32].

Nucleation and growth of grains

During welding, subgrains nucleate directly from randomly oriented grains in the base metal (HAZ), which form the substrate at the fusion boundary. The driving force required for nucleation is low since the thermodynamic barrier for solidification is almost eliminated and only growth of new grains occurs [33]. New grains (crystals) nucleate by arranging atoms from the base metal (HAZ) grains without altering their existing crystallographic orientation. This is described as epitaxial growth [31], as shown in Figure 2.10.

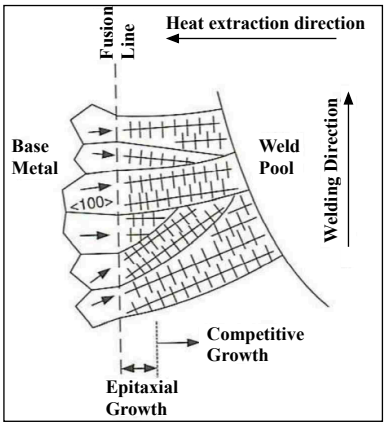

Figure 2.10: Epitaxial growth at the fusion boundary [31].

Since solidification of the weld metal proceeds spontaneously by epitaxial growth of the partially melted grains in the base metal, the FZ grain structure is mainly determined by the base metal grain structure and the welding conditions [34]. Grains tend to grow perpendicular to the pool boundary along the maximum direction of heat extraction [31]. In addition, crystallographic effects will influence grain growth by favoring growth along the easy growth direction, namely the $<100>$-direction [34] (see Figure 2.10).

Conditions for growth are optimum when one of the easy growth directions coincides with the heat-flow direction. These grains grow faster than grains less favorably oriented, and this results in formation of solidification grain boundaries at regions where these subgrains impinge (competitive growth). Without additional nucleation, this will promote a columnar grain structure [34].

Solidification modes

The weld (FZ) microstructure varies noticeably from the edge to the centerline of the weld. This is because the temperature gradient G and the growth rate R dominate the solidification microstructure. As shown in Figure 2.11, the growth rate R is low along the fusion line and increases toward the centerline. While the temperature gradient G is low at the centerline and increases toward the fusion line. The maximum temperature T_{max} is in the center of the weld pool and decreases toward the fusion line [31].

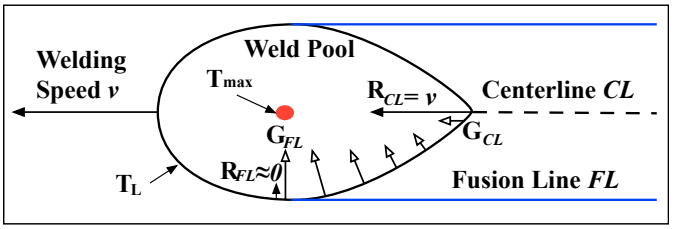

Figure 2.11: Variation of temperature gradient G and growth rate R along the weld pool boundary. Based on ideas of Udumphol [31].

Since the ratio between the temperature gradient and the growth rate G/R decreases from the fusion line toward the centerline, the solidification mode may change across the fusion zone [31]. This is shown in Figure 2.12 .

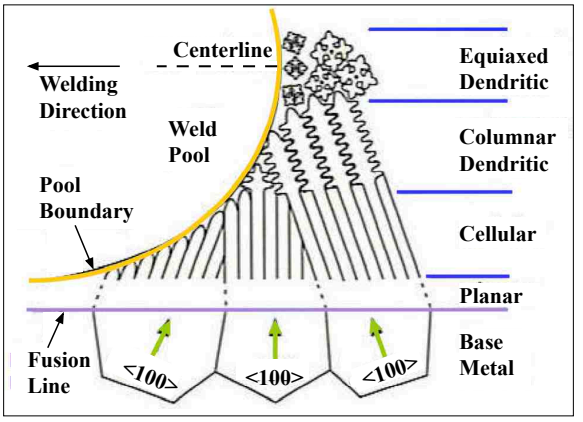

Figure 2.12: Solidification modes across the fusion line [31].

The amount of supercooling dictates the mode of solidification and the associated morphology of the solidified microstructure. As the constitutional supercooling increases, the solidification mode changes from [33, 31]:

$$Planar \rightarrow Cellular \rightarrow Columnar\,dendritic \rightarrow Equiaxed\,dendritic \tag{2.2}$$

Solidification cracking

Aluminium alloys are sensitive to solidification cracking as a result of high thermal expansion combined with a brittle structure at, and just below, the solidification temperature [29, 35]. The weld pool of GMAW aluminium alloys solidifies very fast due to the high heat conductivity [29, 36].

Solidification cracking takes place within the weld fusion zone and appears typically along the center of the weld or at termination craters [4], see Figure 2.13. The crack may occur when solidifying weld metal undergoes large tensile stress during its solidification [9].

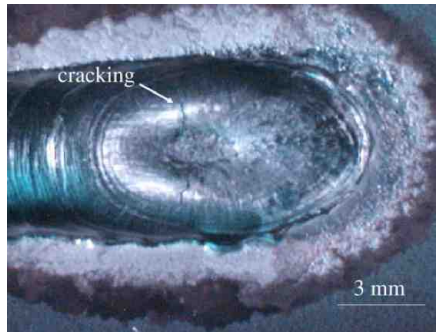

Figure 2.13: Cracking in the weld fusion zone at the end of a weld (termination crater) [29].

The weld crack sensitivity of the heat-treatable aluminium is basically affected by the weld metal composition and the welding parameters, where high heat inputs (such as high currents and slow welding speeds) are believed to contribute to weld solidification cracking [4]. The solidification structure of the FZ is highly affected by the welding speed [37]. And the solidification structure along the weld fusion boundary seems to play an important role in cracking susceptibility [33, 38].

Because of the detrimental effect of weld cracks on joint properties, the weldability of aluminium alloys is defined as its resistance to weld cracking [4].

2.2.3 The heat-affected zone

The heat-affected zone (HAZ) represents a major problem because the resulting microstructural changes lead to a permanent mechanical degradation of the base metal [5, 25].

After artificial ageing, a high density of the fine needle-shaped β'' particles is present in the matrix, see Figure 2.14 (a). These particles are thermodynamically unstable in a welding situation, so the smallest particles will start to dissolve in parts of the HAZ where the peak temperature exceeds 220°C. The larger particles continue to grow, see Figure 2.14 (b) [25].

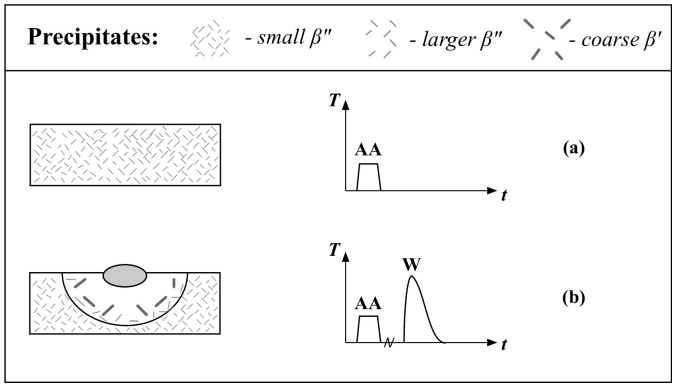

Figure 2.14: Schematic diagrams showing the microstructure evolution during thermal processing of Al-Mg-Si alloys involving artificial ageing (AA) and welding (W). Based on the ideas of Myhr et al. [25].

Close to the weld fusion line full reversion of the β'' particles is achieved. At the same time, coarse rod-shaped β' precipitates may form in the intermediate peak temperature range between 220-500°C [25]. The minimum HAZ hardness is found in the position of the HAZ that experience temperatures within this range. This zone is also referred to as the overaged zone [4]. Figure 2.15 shows a sketch of the typical HAZ strength profile for a peak-aged Al-alloy after complete natural ageing.

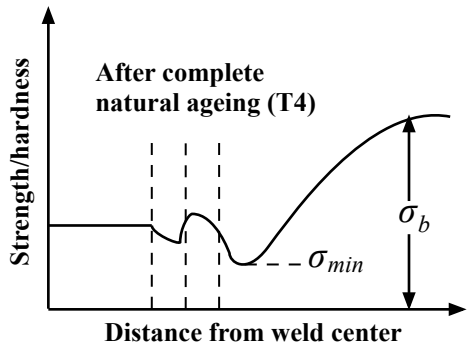

Figure 2.15: Sketch of the HAZ strength profile after complete natural ageing. Based on the ideas of Grong [5].

At higher temperatures, in positions close to the fusion line, particles are dissolved and their constituent elements go into solid solution. Upon natural ageing (cooling) subsequent to welding, this solute may precipitate as strengthening phases. This contributes to the slight increase in hardness that typically occurs near the FZ for the 6xxx series alloys [4, 39], see Figure 2.15.

2.3 Friction Stir Welding of Al-Mg-Si alloys

In addition to the primary/traditional methods for welding of aluminium, conventional solid-state joining processes like friction stir welding are being frequently used [5]. The principal advantages of FSW, being a solid-state process, are low distortion, absence of melt-related defects and high joint strength. Since the technique does not require filler, the fusion zone (FZ) with its as-cast microstructure is eliminated. Instead, this zone is replaced by a thermo-mechanically affected zone (TMAZ), which exhibits superior mechanical properties. Despite this, HAZ softening is still a major problem [5, 24].

2.3.1 The FSW process

The parts to be welded are rigidly clamped on a backing plate attached to the machine table. A rotating tool, composed of a threaded pin and a shoulder, is introduced into the material along the joint axis until the shoulder gets in contact with the upper surface of the plates. Heat generated by friction and deformation brings the material flowing from the front to the back of the tool where it cools down [26, 40], see Figure 2.16.

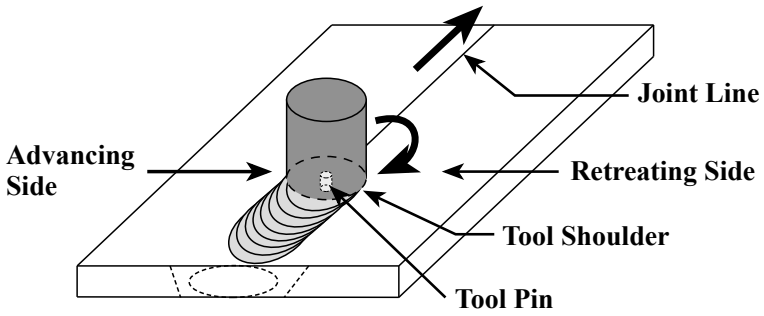

Figure 2.16: Schematic description of the friction stir welding process. Based on the ideas of Gallais et al. [41].

The side of the welding tool, where the surface motion (due to spinning) is in the same direction as the travel direction, is referred to as the *advancing side*. While the opposite side, where the surface motion opposes the travel direction, is referred to as the *retreating side* [24, 42]. The weld quality is very dependent on the welding parameters such as the speed, the advancing speed, the welding equipment, and the tool geometry [40].

Both large deformations and non-isothermal treatments contribute to the microstructure evolution and to the subsequent modification of the mechanical properties. As a result, the mechanical properties of the joint are highly heterogeneous. As shown in Figure 2.17, the FSW joint is divided into various regions based on the distance from the welding tool (joint center line) [41].

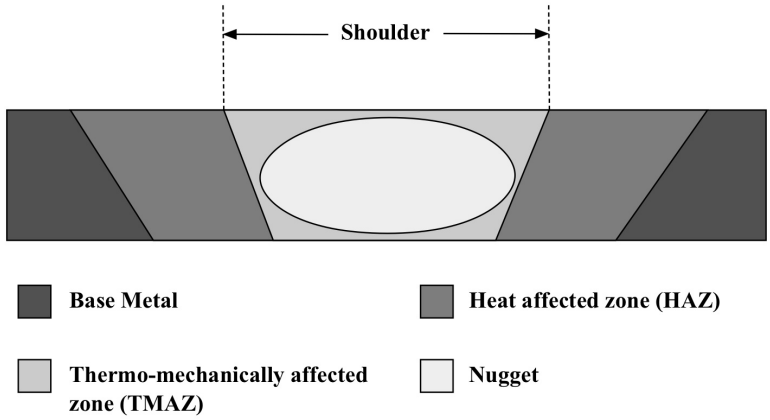

Figure 2.17: Sketch of a butt joint profile. Based on the ideas of Khaled [24].

The different regions shown in Figure 2.17 will be shortly presented in the following subchapters.

2.3.2 Nugget/stir zone (SZ)

The central region of a FSW joint is called the weld nugget (or the stir zone). In this region, the dislocation density is low compared to the thermo-mechanically affected zone (TMAZ) because of recrystallization. The nugget is described as the dynamically recrystallized region of the TMAZ, where the deformation and the maximum temperature and strain are larger than for the other regions of the joint. The temperature and strain distribution across the joint are shown in Figure 2.18 [26, 41, 43].

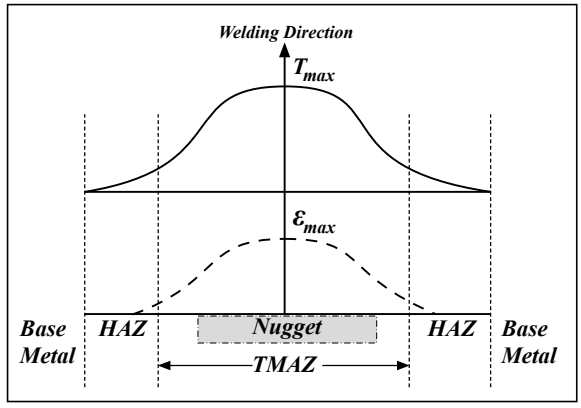

Figure 2.18: Maximum temperature and strain associated with the FSW process. Based on the ideas of Gallais et al. [41].

Since the nugget is fully recrystallized during welding, this zone exhibits a fine equiaxed grain structure with grains much smaller compared to the base material. The grain size of the nugget has a second order effect on its hardness in age-hardenable Al alloys [26, 41, 43].

2.3.3 Thermo-mechanically affected zone

The TMAZ is like the nugget, highly deformed by the material rotational flow [26, 43]. In this region the material is affected both by non-isothermal heat treatment and plastic deformation. It is possible to generate considerable plastic strain in this region without recrystallization, therefore, this zone exhibits elongated and deformed grains. As shown in Figure 2.19, there is a distinct boundary between the recrystallized (nugget) and deformed zones of the TMAZ [14, 41].

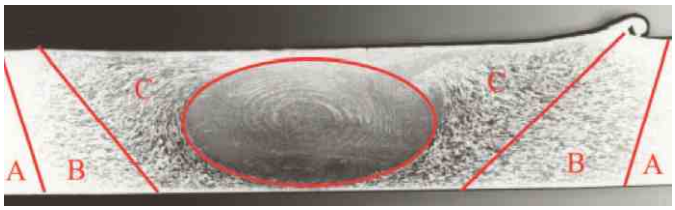

Figure 2.19: Microstructural zone classification in a friction stir weld [14].

The TMAZ microstructure evolves mainly through the dissolution and/or coarsening of the hardening phases [14, 41].

2.3.4 The FSW heat-affected zone

As shown in Figure 2.17, the heat-affected zone (HAZ) is the zone most distant from the joint centre line. It is not deformed during the process but the microstructure evolves due to the welding thermal cycles, influencing the mechanical properties [26, 43]. No apparent plastic deformation is detected by light microscope, but it is recognized that some plastic deformation may occur, as is typically the case in any weld HAZ [14].

The different zones presented above correspond to different mechanical properties. Usually, a significant drop in hardness is observed at the TMAZ/HAZ interface, which, associated with a low or moderate strain hardening capacity, constitutes the locus for the localization of plastic deformation and damage accumulation [41]. The typical hardness evolution of a FS welded component is shown in Figure 2.20.

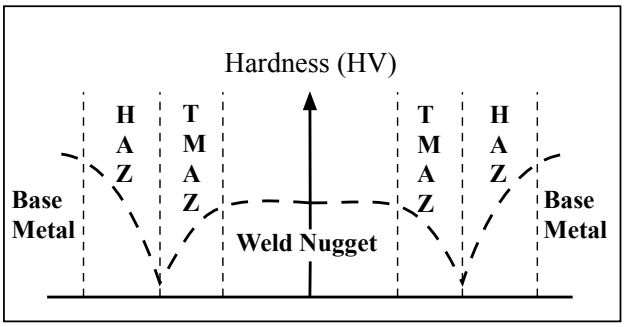

Figure 2.20: Sketch of the typical hardness evolution in FS welded material. Based on the ideas of Gallais et al. [41].

Both coarsening and dissolution lead to a drop in hardness, but strength recovery only occurs following dissolution. Therefore, the hardness profiles are consistent with precipitate coarsening being dominant in the HAZ (lower peak temperatures) and dissolution in the nugget (peak temperatures above the solvus of the initial precipitates), followed by natural ageing. The greatest recovery in strength is observed in the nugget [26, 44].

2.3.5 Mechanical properties of friction stir welds

As a contrast to fusion welding, the absence of fusion in FSW removes much of the thermal contraction associated with solidification and cooling, leading to a significant reduction in distortion [14, 45]. Instead, the metal flow and heat generation in the softened material around the tool are fundamental to the friction stir process. Material deformation generates and redistributes heat, producing the temperature field in the weld [14].

Since the microstructure across a friction stir weld is highly non-uniform, the yield strength, tensile strength and ductility may change considerably over very short distances. Very different results can be obtained whether the welds have been tested longitudinal or transverse of the weld [14].

In cross-weld tensile testing, as shown in Figure 2.21, the stress-strain behavior is dependent on the width of the specimen, which will determine the retained residual stresses, and the length of the specimen, which will determine the average ductility/overall elongation, stress at offset yield, etc. [14].

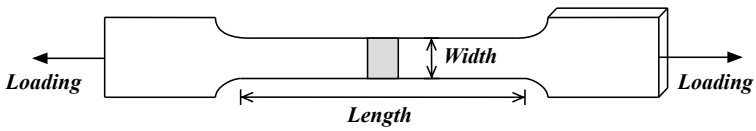

Figure 2.21: Sketch of a cross-weld tensile specimen.

For the heat-treatable alloys (irrespective of the heat treatment condition), tensile testing transverse of the the weld orientation normally fail at the side of the nugget, at or close to the HAZ/TMAZ boundary. Failures can occur on advancing and retreating sides, although for a series of welds they will usually all fail on one side or all fail on the other side (the failure mechanism is a ductile shear failure, showing 45°facets) [14, 46].

The elongation found in tensile specimens transverse of the weld orientation, is almost invariably less than found in the parent (base) material. This is in many cases not due to low ductility, as confirmed by the significant reduction in area and substantial necking. Instead, the strain will have concentrated in a very small part of the gauge length where a locally softer microstructure may have formed [14].

In contrast, test samples cut from larger plates may retain a significant portion of the weld stresses, which may compromise tensile strength measurements. Only when the cross-weld specimen width is less than the size of the tensile zone (approximately the width of the HAZ) the residual stress is negligibly small. Tensile strength is typically about the same as found in the parent material [14, 47].

As opposed to the hardness and the static strength, the Charpy impact energy (and CTOD) in the friction stir welds are much higher than those corresponding to the parent (base) metal or the HAZ. The microstructural factors play a determining role in fracture toughness. This typically concerns the FSW nugget zone, where a higher toughness compared to the parent material have been found [14, 48].

2.4 Load-bearing capacity of welded components

Despite some differences in microstructural features and mechanical properties, HAZ softening is still of great concern in case of FSW and GMAW. In engineering design, this strength loss must be taken into concideration [49].

The measured HAZ hardness profile can be used to calculate the yield stress across the HAZ by using the relationship [49]:

$$\sigma_{\mathrm{y}}(MPa) = 3.0HV - 48 \tag{2.3}$$

By inserting the minimum value from the HAZ hardness profile into Equation 2.3, the corresponding minimum HAZ yield strength σ_{min} can be found. If the loading is perpendicular to the weld, as shown in Figure 2.22, the load-bearing capacity *P* can be calculated by using the relationship [50]:

$$\sigma_{\mathrm{min}} = \frac{P}{dW} \tag{2.4}$$

from which:

$$P(kN) = \sigma_{\min}(dW) \tag{2.5}$$

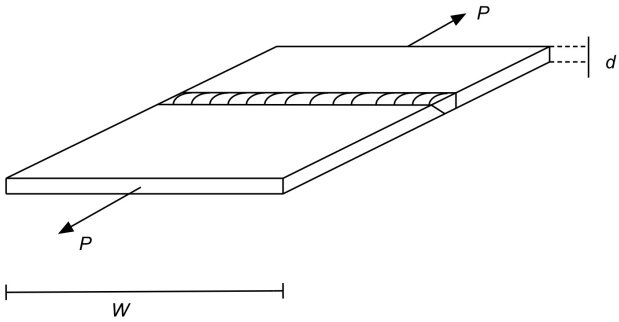

Figure 2.22: Loading perpendicular to the weld. Based on the ideas of Myhr et al. [49].

where P is the maximum tensile (or compressive) force that can be applied perpendicular to the axis of the weld, d is the plate thickness and W is the width of the component.

In engineering design, $\sigma_{\min}$ has a direct physical meaning, since it is the key parameter determining the joint strength when the loading is perpendicular to the weld [49].

If the loading is parallel to the weld, as shown in Figure 2.23, the calculations of the design stress become more complex.

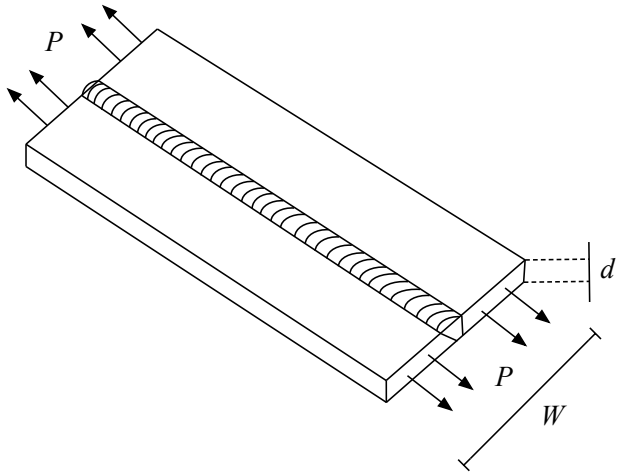

Figure 2.23: Loading parallel to the weld. Based on the ideas of Myhr et al. [49].

In this approach, Mazzolani [50] introduces the so-called reduced cross-sectional area A_{red} as a basis for calculating the design stress. Figure 2.24 is a sketch showing how the equivalent half width of reduced strength zone y_{red}^{eq} of minimum strength σ_{min} is related to an assumed yield strength profile across the weld.

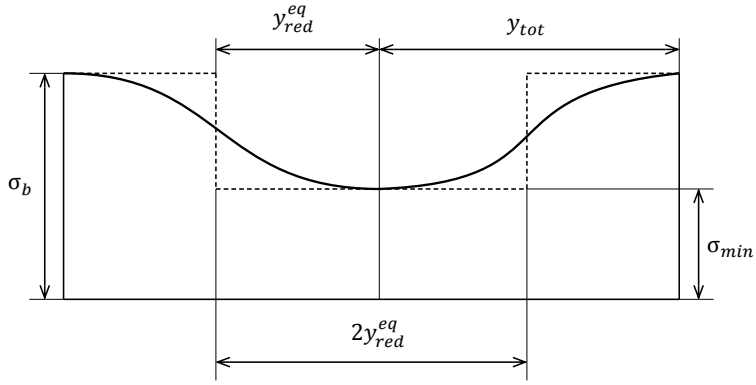

Figure 2.24: Idealized yield strength profile. Based on the ideas of Mazzolani [50] and Myhr et al. [49].

Acording to Figure 2.24, the reduced cross-sectional area A_{red} can be written as:

$$A_{red} = A - 2y_{red}^{eq} d(1 - \beta) \tag{2.6}$$

where A is the total cross-sectional area of the joint, y_{red}^{eq} is the equivalent half width of the reduced strength zone (including the weld metal) of minimum strength σ_{min}, while β is a metallurgical efficiency factor that takes into account the degree of softening occurring due to welding ($\beta \leqslant 1$). The β-factor is defined as:

$$\beta = \frac{\sigma_{min}}{\sigma_b} \tag{2.7}$$

The equivalent half width of the reduced strength zone y_{red}^{eq} of strength σ_{min} can be calculated by solving the integral [50]:

$$y_{red}^{eq} = \frac{\int_0^{y_{tot}} \sigma \, dy}{\sigma_{min}} \tag{2.8}$$

where the upper integration limit y_{tot} refers to the half width of the reduced strength zone (including the weld metal). In summary, when the loading is parallel to the weld, the design stress $\sigma_{\parallel}$ can be calculated on the basis of A_{red}, using Equations 2.6 and 2.7.

Chapter 3

Experimental

3.1 Base material

3.1.1 Chemical composition

Aluminium alloy 6082 was used in the experimental work. The chemical composition of the base metal is shown in Table 3.1.

Table 3.1: Chemical composition of AA6082 used as base metal [51].

Alloying element [wt%]										
Fe	**Si**	**Mg**	**Mn**	**Ca**	**Cu**	**Ga**	**Na**	**Ti**	**Zn**	**Al**
0.2	1.02	0.67	0.53	0.0006	0.003	0.01	0.00008	0.01	0.006	Bal.

3.1.2 Casting and homogenization conditions

The material was DC cast into billets of Ø 203 mm in diameter and 3.25 m of length at Hydro Research and Technology Development (RTD) Centre in Sunndalsøra. After the casting procedure the billets were homogenized as shown in Table 3.2.

Table 3.2: The homogenization process applied to AA6082 [51].

Heating rate [°C/h]	**Holding temp. [°C]**	**Holding time [h]**	**Cooling rate [°C/h]**
200	580	2	300-350

3.1.3 Extrusion and heat-treatment

After the homogenization process, the extrusion of the billets was carried out in an industrial extrusion press. The extruded sheets were subsequently solution heat-treated, rapidly quenched into water and then artificially aged to obtain the T6 temper condition. The ageing conditions can be found in Table 3.3.

Table 3.3: Artificial ageing of the AA6082 sheets prepared for welding.

Heating rate [°C/h]	Holding temp. [°C]	Holding time [h]	Cooling
200	185	5	Air cooling to room temp.

3.2 Welding of the sheets

After artificial ageing, as described in Section 3.1, the same base metal was used both for gas metal arc welding (GMAW) and friction stir welding (FSW).

3.2.1 Gas metal arc welding

Extruded and heat treated sheets with dimensions 3x200x400 mm was used for GMAW. A sketch of the single sheets is shown in Figure 3.1.

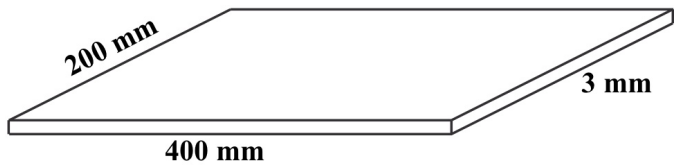

Figure 3.1: Schematic illustration of the extruded sheets used for GMAW.

The weld deposition was carried out at SINTEF in an I-groove with 1 mm root opening in one pass, using fully automatic GMAW process with AA5183 as filler wire. Welding parameters can be found in Table 3.4.

Table 3.4: Welding parameters used in GMAW of AA6082.

Welding parameters			
Current [A]	Voltage [A]	Travel speed [mm/s]	Shielding gas
165-170	22	10	Ar 4.6

Two-and-two sheets were welded together. Figure 3.2 shows a photograph of the GMA welded sheets received from SINTEF.

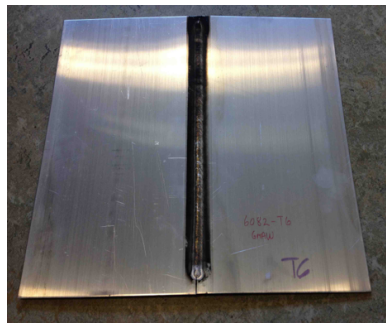

Figure 3.2: Photograph of the GMA welded sheets received from SINTEF.

3.2.2 Friction stir welding

Friction stir welding was performed by standard procedures at Marine Aluminium, Karmøy. The dimensions of the FS welded sheets were 3x400x900 mm. Figure 3.3 shows photographs of the FS welded sheets received from Marine Aluminium.

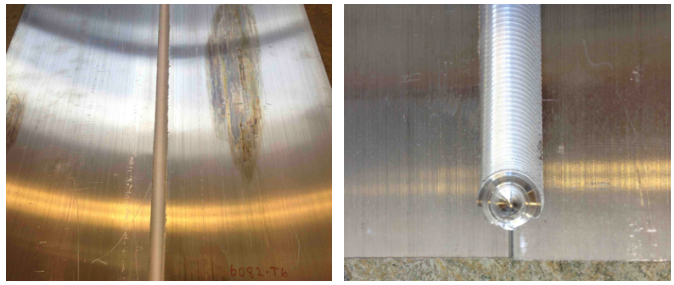

Figure 3.3: Photographs of the FS welded sheets received from Marine Aluminium.

In addition to an overview of the FS welded sheets, a close-up of the exit-hole of the pin is included in the figure.

3.3 Sample preparation and metallographic examination

Samples were cut from the end and the middle of the welded sheets and prepared for grain structure investigation and hardness testing. Specimens used for hardness testing were cut so that the HAZ and HAZ/TMAZ degradation on both sides could be measured, see Figure

3.4. They were ground down to a finish of 2400, prior to polishing using diamond paste (suspension) of 3 μm.

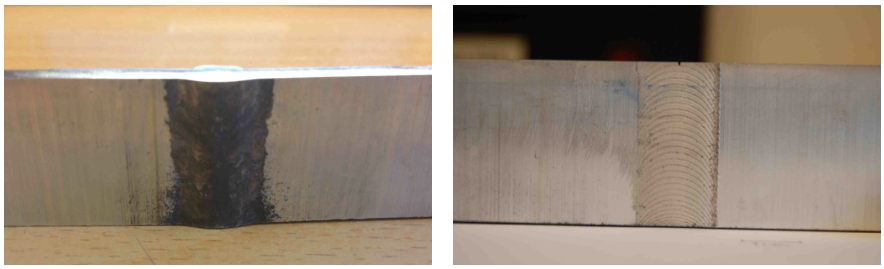

(a) **(b)**

Figure 3.4: Specimens cut from the sheets being used for hardness testing: (a) GMA welded sheets and (b) FS welded sheets.

The specimens used for the microscope examination was embedded in epoxy (cold mounting), ground to 4000 mesh, polished with diamond paste (suspension) of 3 μm and chemically polished with OP-S, corresponding to a surface finish of 1 μm. Before examination in the optical microscope, the specimens were anodized in an electrolyte containing HF (due to the high content of Si) to unveil the grain structure.

3.3.1 Optical microscopy

The ground, polished and anodized samples for both the FS and GMA welded specimens were examined in a Leica MeF4M optical microscope. A lens of 2.5x magnification was used to capture most of the structure in the weld zone.

3.3.2 Hardness testing

Transverse hardness testing was performed to establish changes occurring during welding. The Vickers hardness HV_1 (1 kg load) was measured for the GMA welded sheets with hardness tester Duramin-A2500, while the Vickers hardness HV_5 was measured for the FS welded sheets with Matzusawa hardness tester. The hardness was measured on both sides of the weld, out to a certain distance, where the base metal hardness was obtained. Photographs of both types of weld samples are shown in Figure 3.5.

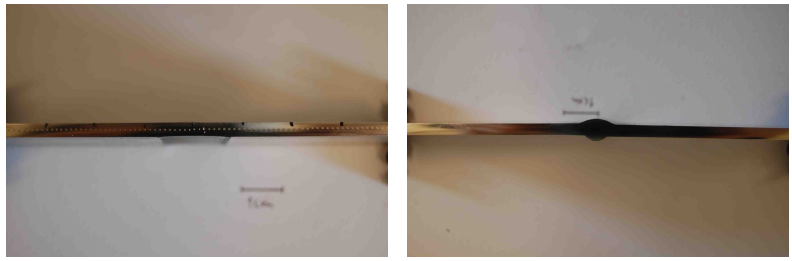

(a) **(b)**

Figure 3.5: Photographs of weld samples used in the hardness testing: (a) FS welded sheets and (b) GMA welded sheets.

3.4 Tensile testing

Tensile testing was carried out both transverse and longitudinal to the welding/extrusion direction. Figure 3.6 shows a schematic illustration of the tensile specimen locations and orientations. In addition, more precise sketches of the GMA and FS tensile specimens can be found in Figures A.1 and A.2, respectively, in the Appendix.

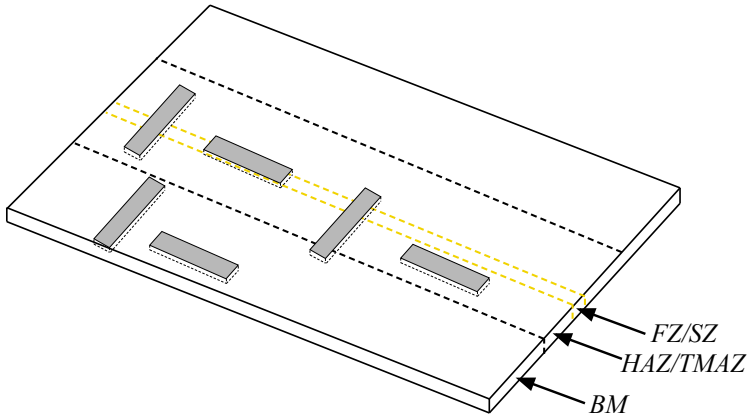

Figure 3.6: Schematic illustration of the location of the tensile specimens.

The specimens were cut from these different locations, transverse or longitudinal to the welding/extrusion direction, to generate specific data for the different weld regions. The labelling of the tensile specimens (for further use in the results), can be found in Table 3.5.

Table 3.5: Labelling of the GMAW and FSW tensile specimens.

Location/direction	Specimen name	
Base metal	**GMAW**	**FSW**
Transverse	BM-T	BM-T
Longitudinal	BM-L	BM-L
FZ/SZ		
Transverse	FZ-T	SZ-T
Longitudinal	FZ-L	SZ-L
HAZ/TMAZ		
Transverse	HAZ-T	HAZ/TMAZ-T
Longitudinal	HAZ-L	HAZ/TMAZ-L

The HAZ and HAZ/TMAZ tensile specimens were supposed to collect information about the weakest parts of the weldments.

The specimen configurations and the test used for both FSW and GMAW test specimens are similar. The tests were done in a MTS servo-hydraulic tensile machine. During testing, the axial elongation was measured using an extensometer with 50 mm gauge length. The basic dimensions of the tensile test specimens are shown in Figure 3.7.

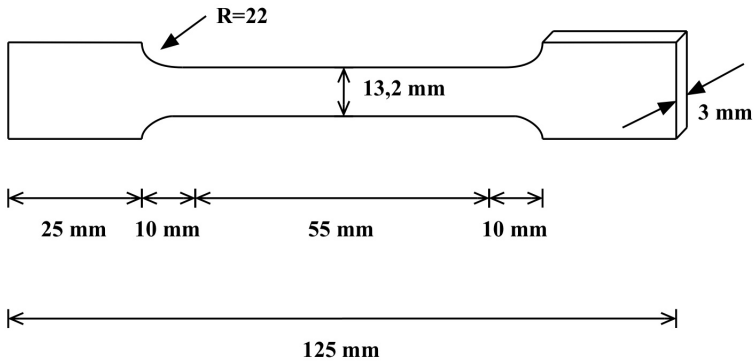

Figure 3.7: Basic dimensions of the tensile test specimens.

Some adjustments were made to the dimensions of the specimens to adjust for distortions and excess weld in the weld zones. This was of great concern, particularly with the GMA welded specimens.

The total number of tensile specimens tested are listed in Table 3.6.

Table 3.6: Total number of tensile specimens machined from the GMA and FS weldments.

Location/orientation	**Total number of specimens**	
Base metal	**GMAW**	**FSW**
Transverse	3	3
Longitudinal	3	3
FZ/SZ		
Transverse	3	3
Longitudinal	3	3
HAZ/TMAZ		
Transverse	3	3
Longitudinal	3	3
	18	18

3.5 Impact testing

Impact data was collected using the Charpy V-notch test. This test was used to get information about the energy absorbed during impact. The Charpy specimens were prepared for the base metal, fusion/stir zone and HAZ in the same direction and orientation as the tensile test specimens (see Figures A.1 and A.2 in the Appendix). In addition, Figure 3.8 shows the orientation of the V-notch in relation to the welding/extrusion direction.

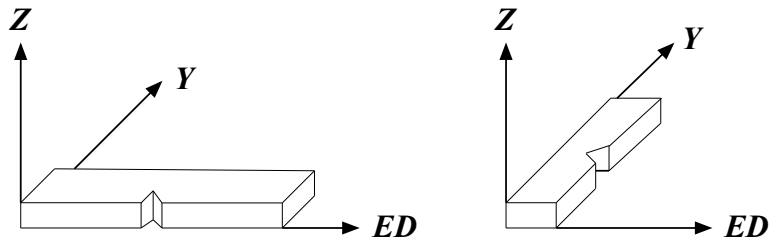

Figure 3.8: Orientations of the V-notch and the Charpy test specimens in relation to the welding/extrusion direction (ED - extrusion direction).

The specimens taken transverse to the welding/extrusion direction had a longitudinal notch, while the longitudinal specimens had a transverse notch.

The dimensions of the Charpy V-notch specimens can be found in Figure 3.9.

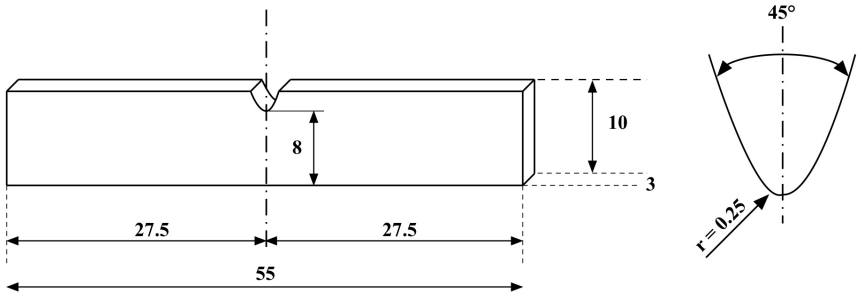

Figure 3.9: Dimensions of the Charpy-V test specimen (in mm).

The base metal specimens were tested both transverse and longitudinal to the extrusion direction, while the FZ/SZ and HAZ/TMAZ specimens were either tested in the longitudinal or the transverse direction. The total number of specimens used in the Charpy V-notch test can be found in Table 3.7. The orientations in the figure refer to the specimen orientation (not the notch).

Table 3.7: Total number of Charpy V-notch specimens machined from the GMA and FS weldments (transverse and longitudinal specimens).

Location/orientation	**Total number of specimens**	
Base metal	**GMAW**	**FSW**
Transverse	3	3
Longitudinal	3	3
FZ/SZ		
Transverse	3	3
Longitudinal	...	...
HAZ/TMAZ		
Transverse	...	...
Longitudinal	3	3
	12	12

The Charpy V-notch test was carried out at room temperature, in a pendulum impact testing machine located at SINTEF in Trondheim, Department of Materials Testing. The absorbed energy was measured on each sample tested.

3.6 Fracture surface analysis in the Scanning Electron Microscope (SEM)

The fracture surface of selected tensile and Charpy V-notch test specimens (for both for types of weldments) was examined in the scanning electron microscope (SEM) Zeiss SUPRA 55VP. The fracture surface examinations were performed with an acceleration voltage of 20 kV. To obtain sufficient depth of field on the rough surfaces, the working distance and aperture was set to 20 mm and 30 μm, respectively.

Chapter 4

Results

In the following sub-chapters, the results from the experimental part will be presented. Optical micrographs and the HAZ hardness profiles can be found for the welds. In addition, the obtained mechanical properties for a selection of the tensile and Charpy V-notch test specimens will presented for both the GMA and the FS weldments.

4.1 Optical micrographs of GMA and FS welds

Figure 4.1 shows an overview and a close-up of the fusion zone microstructure in the GMA weld.

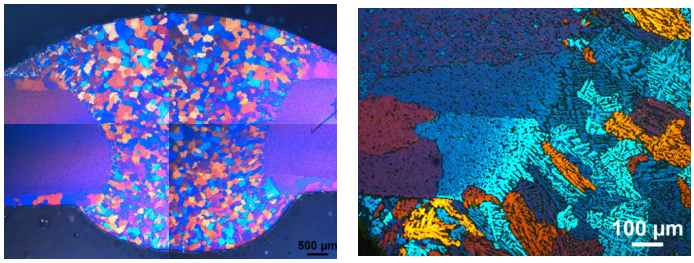

(a) **(b)**

Figure 4.1: Optical micrographs showing an overview and a close-up of the fusion zone microstructure in the GMA weld.

As shown in Figure 4.1a, the grain structure in the fusion zone consists of small eqiuaxed grains with different orientations. Since the image represents the material transverse to the extrusion direction, the fibrous grain structure of the alloy is not visible. The only grain structure evident in the base metal HAZ is the elongated equiaxed grains at the surface,

due to hot working and recrystallization occurring during extrusion. The grains at the fusion line appear to have a more columnar appearance. (The image consists of several individual microscope images, so there are some differences in contrast and brightness in the micrograph).

Figure 4.1b shows the intersection between the base metal HAZ and the fusion zone. Some evidence of epitaxial growth of columnar grains can be observed along the fusion line. These grains descend from the equiaxed grains at the surface of the extruded base material. The FZ basically exhibits an equiaxed dendritic grain structure.

Figure 4.2 shows an overview of the stir zone (SZ) in the FS weld. The image is made from several different microscope images. Therefore, the contrast in the resulting image varies, but the stir zone is still entirely visible.

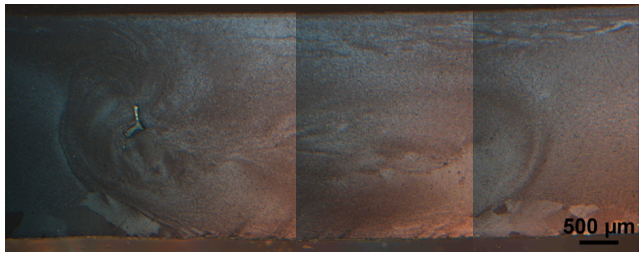

Figure 4.2: Optical micrograph showing the metallography of the stir zone (nugget) in the FS weld.

Figure 4.2 shows the extent of the stir zone, where the material has been plastically deformed by the FSW tool. The figure also shows the differences in material flow between the two opposing sides of the stir zone. The only visible sign of grain structure is observed at the lower surface of the welded sheets.

Figure 4.3 shows the base metal microstructure of AA6082. The extrusion direction is horizontal and the thickness direction is vertical. The figure shows the fibrous texture of the alloy and the recrystallized grain structure at the surface.

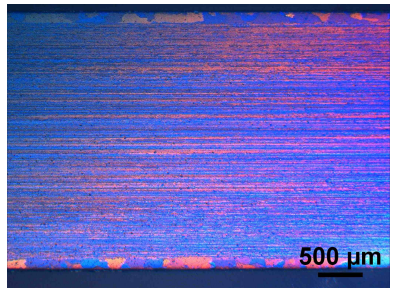

Figure 4.3: Optical micrograph showing the base metal microstructure of AA6082.

4.2 Hardness profiles of GMA and FS welds

Figure 4.4 shows the resulting hardness profile for the GMA weldments. The hardness profile is linked to a macro image of the hardness specimen.

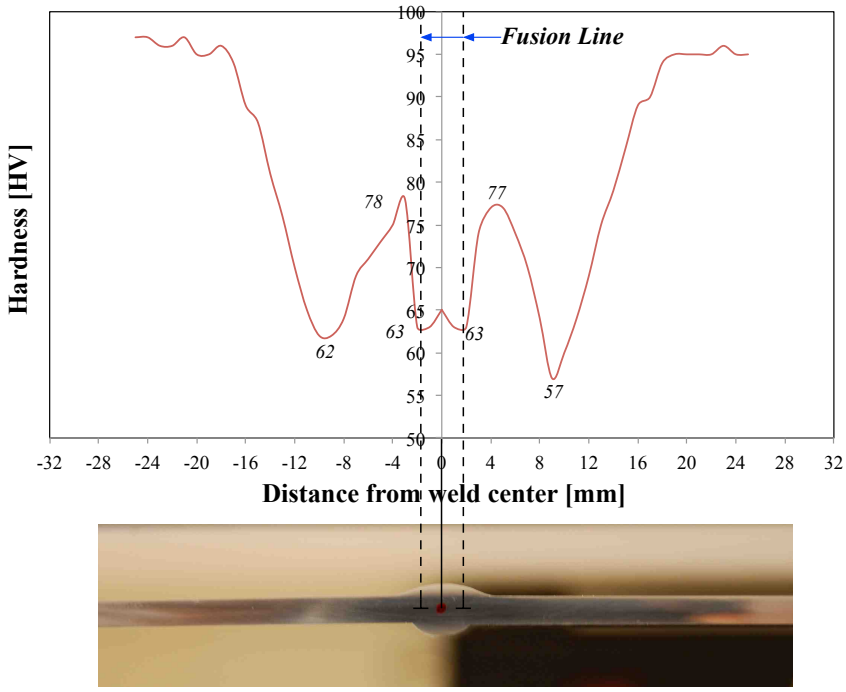

Figure 4.4: Hardness profiles for the GMA weldment, including a macro image of the hardness specimen.

According to the hardness profile, the minimum HAZ hardness can be found 9 mm from the center of the weld on both sides. The minimum HAZ hardness was measured to 62 and 57 HV, respectively. In addition, a small drop in hardness can observed at the fusion line. Full recovery of the base metal hardness is observed approximately 19 mm from the center of the weld. All the individual hardness measurements can be found in Table A.1 in the Appendix.

FS welds usually reveal some hardness differences between the advancing and the retreating side. Since the information on the direction of the welding tool was not available, the different sides have been defined as advancing and retreating to mark the difference. Figure 4.5 shows the resulting hardness profile for the FS welds. The hardness profile is linked to a macro image of the hardness specimen.

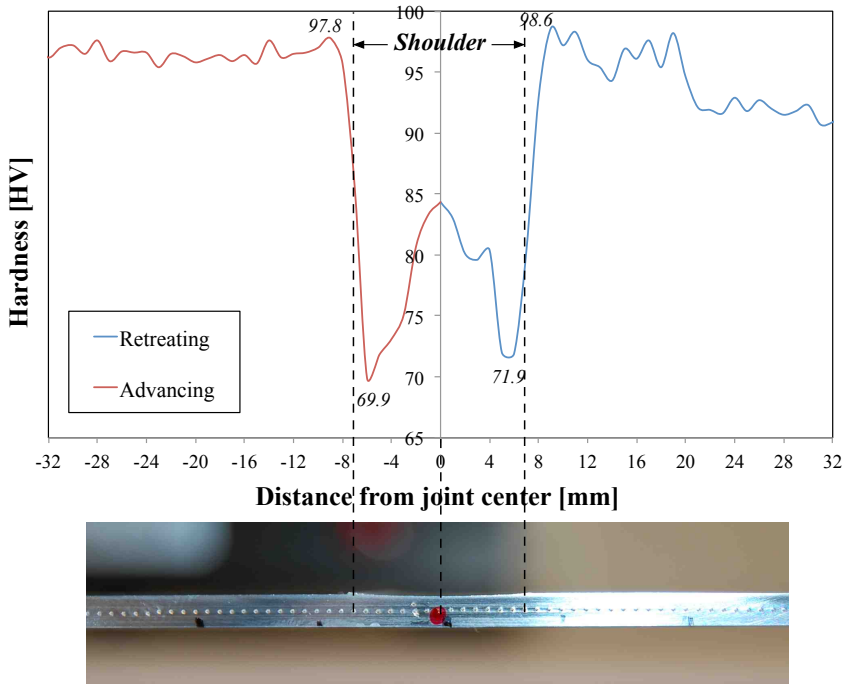

Figure 4.5: Hardness profiles of the FS weldment, including a macro image of the hardness specimen.

The minimum hardness can be found close to the shoulder on both sides, 6 mm from the center of the joint. The minimum hardness on the advancing and retreating side was measured to 70 and 72 HV, respectively. The base metal hardness is approximately 97-98 HV on both sides, but there is a slight drop in hardness on the retreating side further away from the center of the joint. All the individual measurements can be found in Table A.2 in the Appendix.

4.3 Tensile test results

4.3.1 GMAW

As explained in the experimental part, the tensile specimens have been cut from the base metal (BM), the fusion zone (FZ) and the heat-affected zone (HAZ), both transverse (T) and longitudinal (L) to the welding/extrusion direction. Figure 4.6 shows macro images of a selection of the BM, FZ and HAZ tensile specimens tested transverse to the welding/extrusion direction.

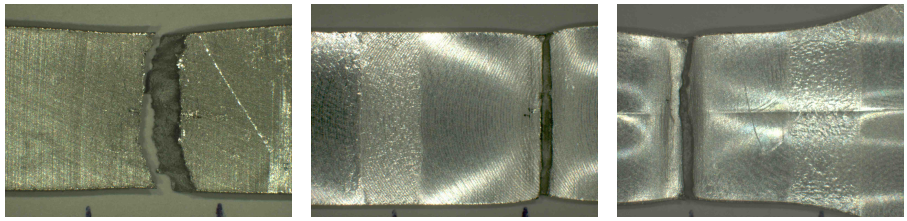

(a) Base metal **(b)** Fusion zone **(c)** HAZ

Figure 4.6: Macro images of the tensile specimens tested transverse to the welding/extrusion direction.

The BM tensile specimen, from Figure 4.6a, has a fairly rough fracture appearance with fibrous pull-out. Some contraction in the thickness can be observed. The FZ and the HAZ tensile specimens from Figures 4.6b and 4.6c appear to have the same course of fracture, where fracture is located at a certain distance from the fusion zone. Small contraction in thickness can also be observed for these specimens.

Figure 4.7 shows macro images of a selection of the BM, FZ and HAZ tensile specimens tested longitudinal to the welding/extrusion direction.

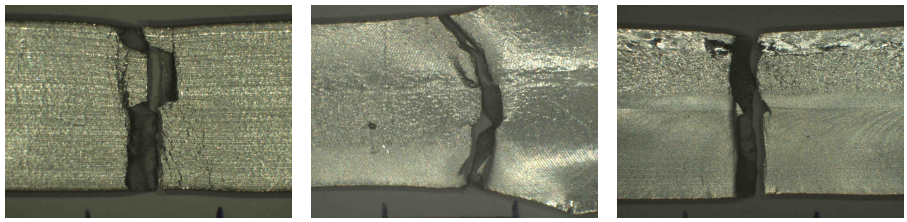

(a) Base metal **(b)** Fusion zone (FZ) **(c)** HAZ

Figure 4.7: Macro images of the tensile specimens tested longitudinal to the welding/extrusion direction.

The BM tensile specimen from Figure 4.7a has a relatively uneven fracture appearance, with visible signs of small cracks close to the origin of the fracture. For the FZ tensile specimen, shown in Figure 4.7b, the fracture occurs outside its gauge length, i.e. in the grip region close to where the extensometer was placed/attached. For the HAZ specimen, shown in Figure 4.7c, the fusion zone is visible in the upper part of the specimen. This part of the specimen has contracted more than the rest of the specimen, and there are visible signs of flaking. In addition, there is a point on the specimen, apparently close to the fusion line, where the material has undergone a slightly different course of fracture.

Figure 4.8 shows the corresponding stress-strain curves for the tensile specimens presented above. The stress-strain curves for all the parallels from the different regions, in addition to macro images of the tested tensile specimens, can be found in Figures A.3 - A.8 in the Appendix.

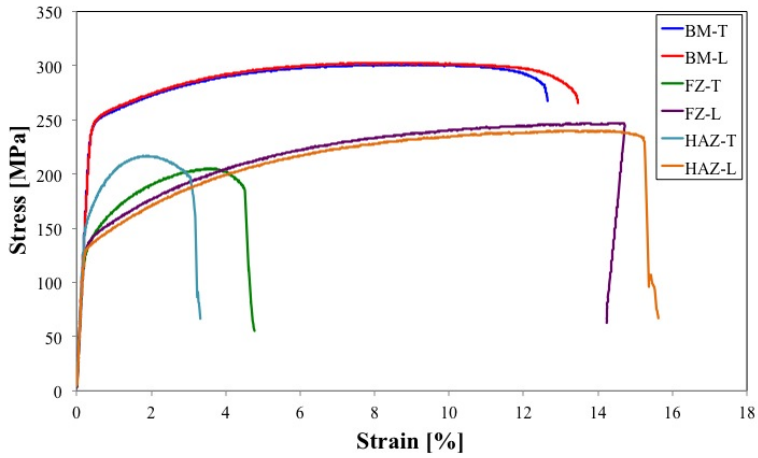

Figure 4.8: Measured stress-strain curves for a selection of tensile test specimens representing different regions (BM, FZ and HAZ) transverse and longitudinal to the welding/extrusion direction.

The stress-strain curves obtained for the BM specimens from both orientations are quite similar. For the FZ and the HAZ specimens, on the contrary, there is a large difference between the specimens tested transverse and longitudinal to the weld. The FZ specimen transverse of the weld is more similar to the HAZ specimen transverse of the weld, while the FZ specimen longitudinal to the weld is more similar to the HAZ specimen in the same orientation.

The resulting stress at offset yield (measured by the extensometer during testing) for the stress-strain curves presented above, is shown in Figure 4.9. In addition, the stress at offset yield for all the tensile specimens tested can be found in Table A.3 in the Appendix.

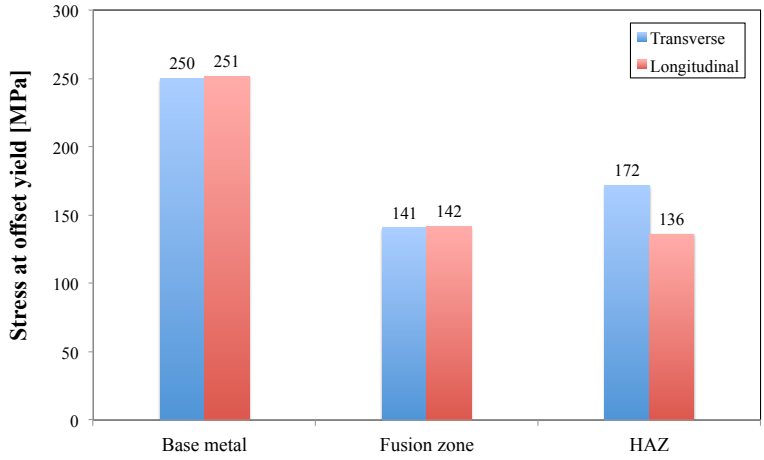

Figure 4.9: Stress at offset yield, as measured from the stress-strain curves presented in Figure 4.8.

The BM tensile specimens in both orientations start to yield at approximately 250 MPa, which is a much higher yield stress compared to the specimens from the other regions. There is almost a factor of 2 between the BM specimens and the FZ specimens. The HAZ tensile specimens are the only specimens that reveal a noticeable difference in stress at offset yield between the two orientations.

Figure 4.10 shows the resulting tensile strength (measured by the extensometer during testing) of the tensile test specimens referred to previously. In addition, the tensile strength for all the tensile specimens tested can also be found in Table A.3 in the Appendix, together with the yield stress measurements.

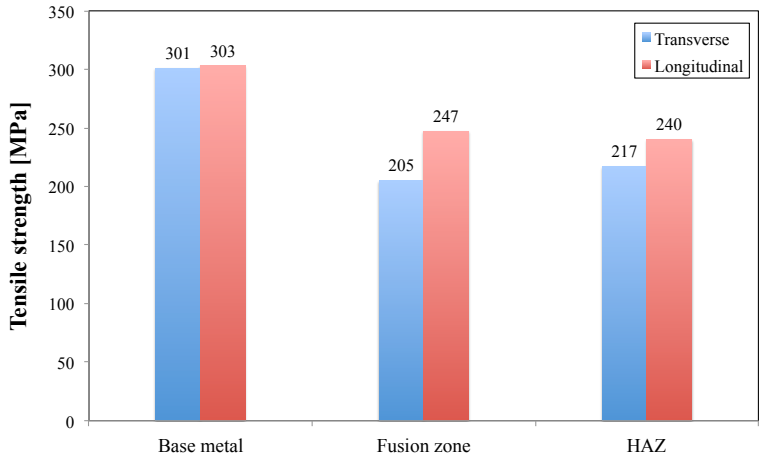

Figure 4.10: Tensile strengths, as measured from the stress-strain curves presented in Figure 4.8.

Figure 4.10 shows that the BM tensile specimens in both orientations reach values above 300 MPa before fracture. Overall, the FZ and the HAZ tensile specimens have lower tensile strength, where the FZ and the HAZ tensile specimens transverse of the weld are slightly weaker than the corresponding specimens in the longitudinal orientation. As shown in Figures 4.6b and 4.7c, these specimens had the same course of fracture close to the fusion zone, which probably corresponds to the weakest part of the HAZ.

Strain at fracture for the tensile specimens is shown in Figure 4.11. The last measured value of strain has been used in the figure for comparison, since many of the specimens had an undefined value for the strain at fracture. All the measurements can be found in Table A.4 in the Appendix. In addition, the corresponding values for the strain at fracture, measured by the extensometer during testing, can be found in the same table for a selection of the samples.

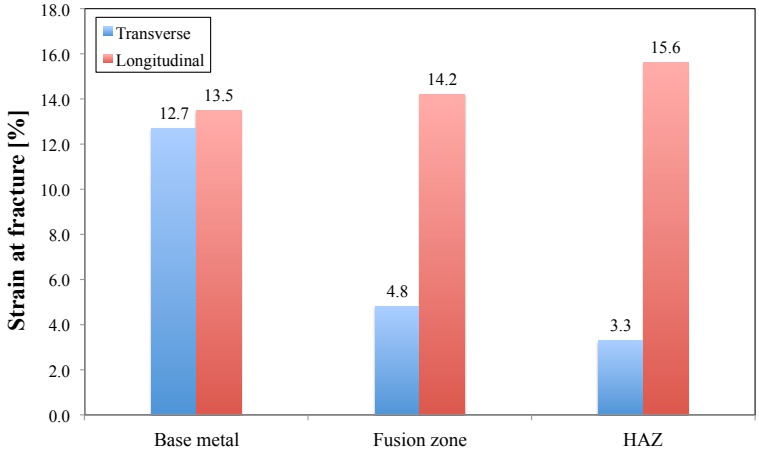

Figure 4.11: Strain at fracture, as measured from the stress-strain curves shown in Figure 4.8.

In strain at fracture from Figure 4.11, the base metal specimens appear to have similar strain at fracture both in the transverse and longitudinal directions. In contrast, the FZ and HAZ tensile specimens reveal large differences in strain at fracture between the two orientations. As assumed, the strain at fracture is observed to be quite low for the FZ tensile specimen representing the transverse direction. The HAZ tensile specimen representing the transverse direction fractured first. Both the FZ and the HAZ tensile specimens tested in the transverses direction represented the weakest part of the weldment.

In addition to the results obtained from the tensile testing, the reduction in area after fracture has been calculated from the following relation:

$$R_{\mathrm{A}} = \frac{A_{\mathrm{i}} - A_{\mathrm{f}}}{A_{\mathrm{i}}} \tag{4.1}$$

where A_i is the initial cross-sectional area and A_f is the cross-sectional area at the point of fracture (see Figure 4.12 for details). Calculated values for the reduction in area of all the tensile specimens tested can be found in Table A.5 in the Appendix.

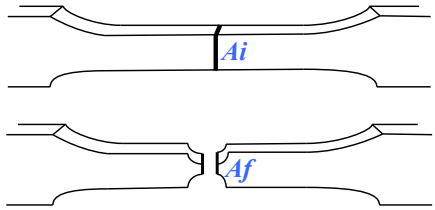

Figure 4.12: Sketch of the initial cross-sectional area A_i and the cross-sectional area at the point of fracture A_f.

Figure 4.13 shows the calculated reduction in area for the tensile specimens presented in Figure 4.8.

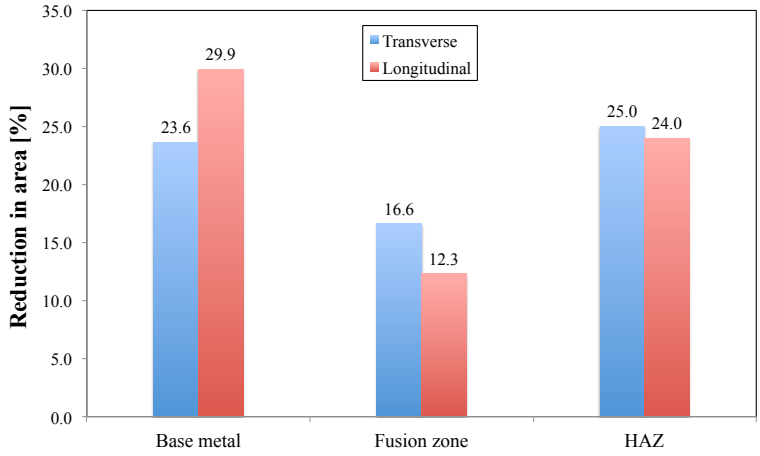

Figure 4.13: Reduction in area, as calculated from the tensile test specimens shown in Figure 4.8.

Both the BM and the HAZ tensile specimens reveal a relatively high reduction in area. In contrast, considering the FZ tensile specimens the reduction in area is below 20% for both orientations. For the FZ tensile specimen representing the transverse direction, the reduction in area correlates well with the measured strain at fracture. The low reduction in area observed for the FZ tensile specimen representing the longitudinal direction, can be a result of the location of the fracture (being close to the exstensometer). And as shown in Figure 4.7b, the fracture of this specimen occurred at the end of the specimen gage, where some of the area from the specimen grip shaft may have altered the resulting reduction in area.

When comparing strain at fracture and reduction in area, which both are a measure of ductility, it is evident that the strain at fracture does not account for the reduction that may take place in the thickness direction of the specimens. In addition, the tensile specimens may react differently to loading due to the pertinent differences in the initial cross-sectional

area. Some of the specimens, especially the FZ tensile specimens, had a much smaller cross-sectional area before testing compared to the others.

4.3.2 FSW

In the tensile test results for the FS weldments, the nugget has been referred to as the stir zone (SZ). Figure 4.14 shows macro images of a selection of the BM, the SZ and the HAZ/TMAZ tensile specimens tested transverse to the welding/extrusion direction.

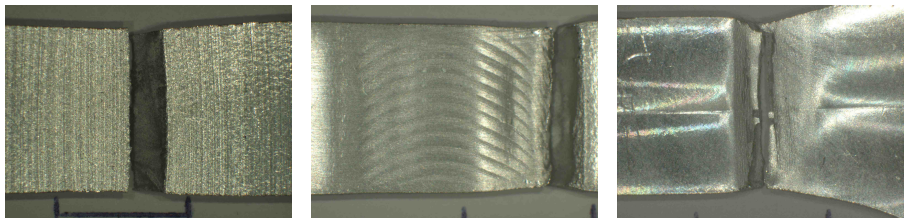

(a) Base metal **(b)** Stir zone (SZ) **(c)** HAZ/TMAZ

Figure 4.14: Macro images of the tensile specimens tested transverse to the welding/extrusion direction.

Considering the BM tensile specimen in Figure 4.14a, the fracture appears to have occurred along the extrusion direction. And there are no visible signs of fibrous pull out from the specimen surface. The stir zone in visible both in Figure 4.14b and 4.14c (not that evident in the case of the HAZ/TMAZ specimen). These specimens appear to have the same course of fracture, except that the the stir zone of the HAZ/TMAZ specimen is located at the end of the gage length, i.e. where the specimen grip shaft starts.

Figure 4.15 shows macro images of a selection of the BM, the SZ and the HAZ/TMAZ tensile specimens tested longitudinal to the welding/extrusion direction.

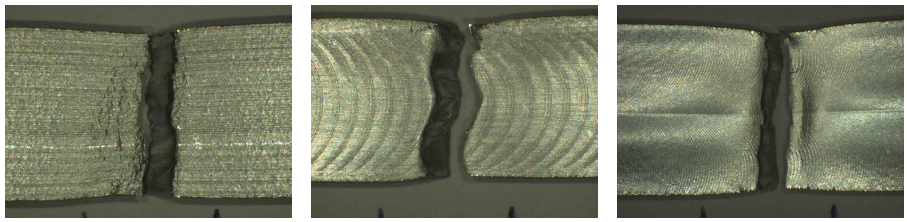

(a) Base metal **(b)** Stir zone (SZ) **(c)** HAZ/TMAZ

Figure 4.15: Macro images of the tensile specimens tested longitudinal to the welding/extrusion direction.

The BM tensile specimens in Figure 4.15a, shows slightly different course of fracture compared to the BM tensile specimens representing the transverse direction. Some minor superficial cracks can be observed close to the fracture. The SZ tensile specimen shown in Figure 4.15b, appears to have a uneven course of fracture, where the center of the stir zone stands out. The difference between the two sides of the stir zone (advancing and retreating as defined in the hardness profiles), where one of the sides have a lower strength, appears to be visible by eye. The HAZ/TMAW tensile specimen from Figure 4.15c, appears to have the same course of fracture as that observed for the HAZ/TMAZ tensile specimen representing the transverse direction.

Figure 4.16 shows the corresponding stress-strain curves of the tensile specimens presented above. The stress-strain curves for all the parallels tested in the different regions, in addition to images of the tested tensile specimens, can be found in Figures A.9 - A.14 in the Appendix.

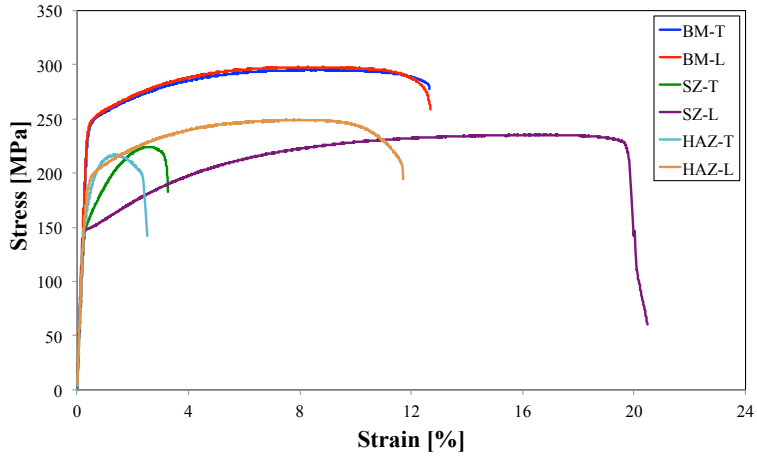

Figure 4.16: Measured stress-strain curves for a selection of tensile test specimens representing different regions (BM, SZ and HAZ/TMAZ) transverse and longitudinal of the welding direction (extrusion direction).

The stress-strain curves for the base metal of the FS weldments are similar. In contrast, large differences can be observed for the SZ specimens from both directions. Also, the HAZ/TMAZ specimens reveal a visible difference in tensile behavior between the two orientations. It appears that the SZ specimen transverse to the weld is more similar to the HAZ/TMAZ specimen transverse to the weld, while the SZ specimen longitudinal to the weld is more similar to the HAZ/TMAZ specimen in the same orientation. This agrees well with the observations made from the GMA stress-strain curves in Figure 4.8.

The resulting stress at offset yield (measured by the extensometer during testing) for the stress-strain curves presented above is shown in Figure 4.17. In addition, the stress at offset yield for all the tensile specimens tested can be found in Table A.6 in the Appendix.

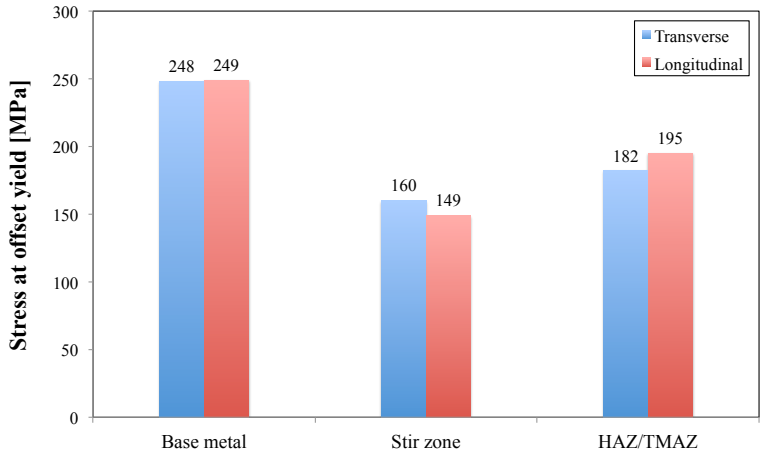

Figure 4.17: Stress at offset yield, as measured from the stress-strain curves shown in Figure 4.16.

The BM tensile specimens in both orientations start to yield at approximately 250 MPa, which is consistent with the observations for the GMA BM tensile specimens. The SZ tensile specimens representing both directions show poor properties compared to the BM tensile specimens, with yield stress between 150 and 160 MPa. The HAZ/TMAZ specimens also reveal lower yield stress compared to the BM tensile specimens.

The resulting tensile strength (measured by the extensometer during testing) for the tensile test specimens is shown in Figure 4.18. In addition, the tensile strength for all the tensile specimens tested can also be found in Table A.6 in the Appendix.

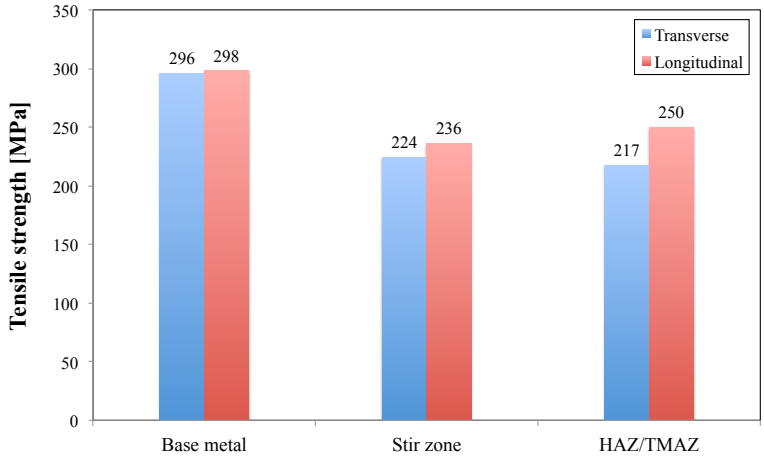

Figure 4.18: Tensile strength, as measured from the stress-strain curves shown in Figure 4.16.

From Figure 4.18, it appears that the tensile strength for the BM tensile specimens is approaching 300 MPa. The difference in strength between the BM tensile specimens and the SZ and the HAZ/TMAZ tensile specimens are not as evident as observed in the yield strength measurements. In addition, there are no major differences between the specimens tested from the same regions.

The corresponding strain at fracture for the tensile test specimens is shown in Figure 4.19. As for the GMA weldments, the last measured value of strain has been used for comparison. All the measurements can be found in Table A.7 in the Appendix, together with the values given by the extensometer for the strain at fracture (not all specimens had measurements of strain at fracture given by the extensometer).

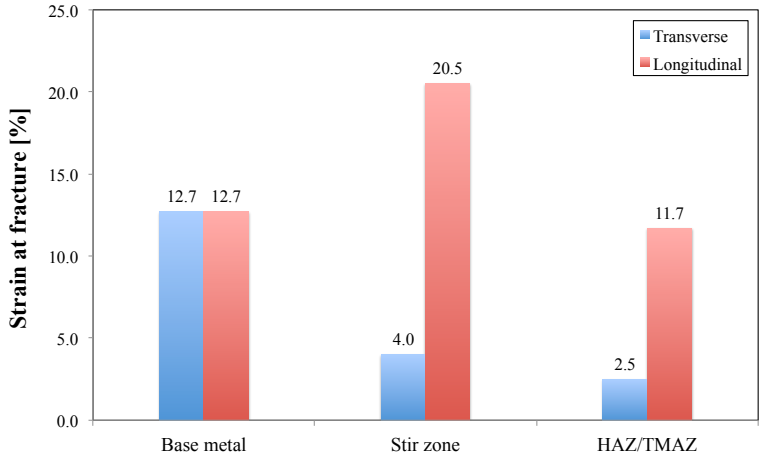

Figure 4.19: Strain at fracture, as measured from the stress-strain curves shown in Figure 4.16.

As shown in Figure 4.19, the measured strain at fracture for the BM tensile specimens are similar in both directions, which is consistent with the observations from the tensile properties. On the contrary, the strain at fracture observed for the SZ and the HAZ/TMAZ tensile specimens is extremely scattered. There is almost a factor of 5 between the fracture strain observed for the two SZ tensile specimens. The same is also true for the HAZ/TMAZ specimens.

Moreover, Equation 4.1 has been used to calculate the reduction in area of the FS tensile specimens. The results are presented in Figure 4.20. In addition, the reduction in area for all the tested specimens can be found in Table A.8 in the Appendix.

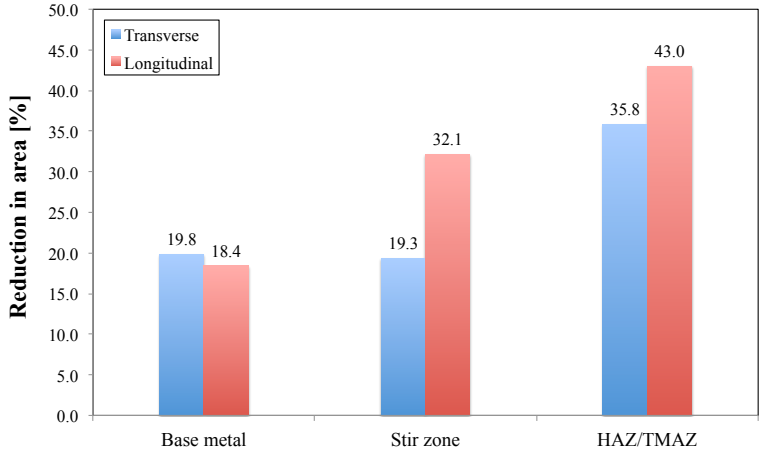

Figure 4.20: Reduction in area, as measured for the FS tensile test specimen.

It is evident from Figure 4.20, that these results are not consistent with the fracture strain data. The reduction in area of the HAZ/TMAZ tensile specimens is about 40 %, while the reduction in area for the BM tensile specimens is close to 20 %. The HAZ/TMAZ tensile specimens representing the transverse direction, of which fracture occurred at an early stage during tensile testing, appear to have experienced a severe reduction in area. This observation is surprising and cannot readily be explained.

4.4 Fractography of the tensile specimens

4.4.1 GMAW

The results from the fractographic examination of the base metal, FZ and HAZ (longitudinal) tensile specimens are presented below. The HAZ tensile specimens transverse of the welding direction had the same characteristic features as the FZ tensile specimens in the same direction.

Figure 4.21 shows the fracture surfaces of the BM tensile specimens representing the transverse and longitudinal direction at low and high magnification, respectively. In the overviews of the fracture surfaces only one side of the specimen is presented. Additional SEM images can be found in Figure A.15 in the Appendix.

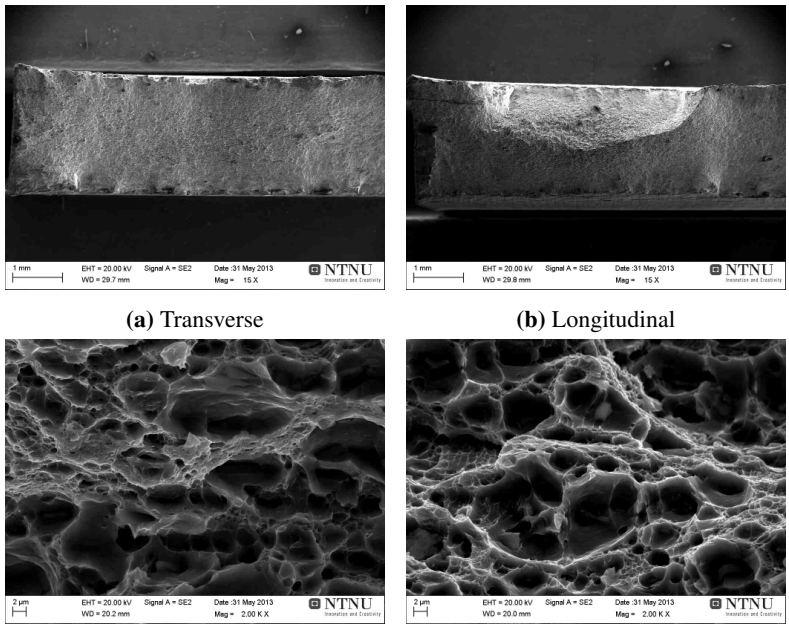

(a) Transverse **(b)** Longitudinal

(c) Transverse. High magnification **(d)** Longitudinal. High magnification

Figure 4.21: Fracture surfaces of the BM tensile specimens representing the transverse and longitudinal extrusion direction.

The overview in Figure 4.21a shows that the BM-T tensile specimen has an overall plane fracture surface. Although not visible at low magnification, a line pattern can be observed across the specimen. This pattern reflects the fibrous grain structure. Figure 4.21c shows the same specimen at high magnification. The fracture surface is covered by larger dimples (5-10 μm) and an amount of smaller dimples in-between the large ones.

For the longitudinal BM specimen, shown in Figure 4.21b, the fracture surface has some uneven areas. This indicates that the specimen has a varying ductility across the fracture surface. Figure 4.21d represents the part of the specimen where the surface is elevated. The fracture surface is covered by relatively large dimples (5-10 μm), where smaller dimples can be seen in-between the large ones. It appears that the BM-L specimen has a higher density of small dimples compared to the BM-T specimen.

Figure 4.22 shows the fracture surfaces of the FZ tensile specimens transverse and longitudinal to the welding direction at low and high magnification, respectively. Additional SEM images of the fracture surface overviews can be found in Figure A.16 in the Appendix.

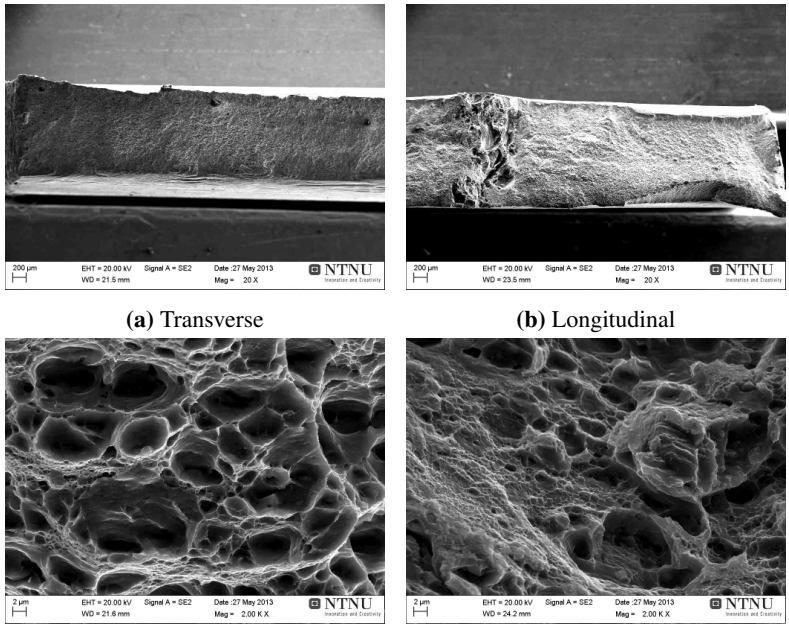

(a) Transverse **(b)** Longitudinal

(c) Transverse. High magnification **(d)** Longitudinal. High magnification

Figure 4.22: Fracture surfaces of the FZ tensile specimens representing the transverse, and the longitudinal direction.

Figure 4.22a represents the fracture surface of the weakest part of the HAZ. The overview shows that the specimen surface is slightly uneven. In this case the fracture surface appears to consist of both ductile and somewhat brittle (darker parts of the specimen) areas. The brittle parts especially concern the edges of the tensile specimen, confirmed by less contraction in area (see Figure A.16a in the Appendix for a overview of the other specimen edge). According to Figure 4.22c, the fracture surface is covered by relatively large dimples with a faceted appearance and smaller dimples in-between the large ones. In addition, some of the facets are surrounded by a high density of small dimples less than 1 μm.

Figure 4.22b represents the fracture surface of the fusion zone. The overview shows some signs of contraction at the edges on both sides (see Figure A.16b in the Appendix for a overview of the opposite specimen edge). In addition to the contracted parts of the specimen, the joint between the two sheets is visible in the center of the specimen (uneven fracture surface to the left in the image). According to Figure 4.22d, the fracture surface contains some medium to small dimples (2-5 μm) with faceted appearance. A high density of small dimples is covering the largest part of the fracture surface.

Figure 4.23 shows the fracture surface of the FZ tensile specimen representing the longitudinal direction, including a close-up of the fracture surface in the center of the fusion zone. This shows evidence of crack propagation in the center of the fusion zone.

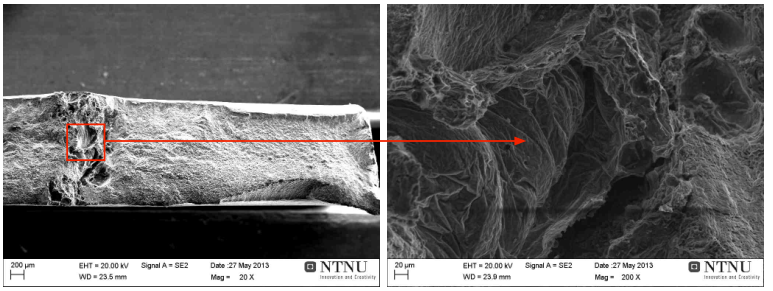

Figure 4.23: FZ tensile specimen representing the longitudinal direction, showing the fracture surface in the center of the fusion zone.

From the fracture surface image of the FZ-L tensile specimen, shown in Figure 4.23, it appears that the specimen has cracked in the middle of the fusion zone, where the columnar grains meet. The fracture surface has a brittle appearance, with only a small amount of small dimples. The brittle appearance is also confirmed by the low reduction in area in this part of the specimen compared to the contraction at the specimen edges.

Figure 4.24 shows the fracture surface of the HAZ tensile specimen orientated longitudinal to the welding direction. This specimen represents both the HAZ and some parts of the fusion zone.

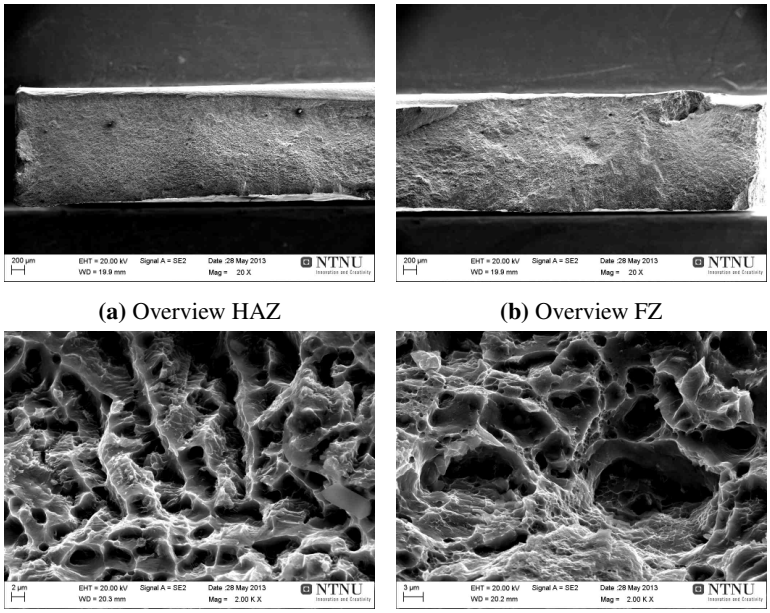

(a) Overview HAZ **(b)** Overview FZ

(c) HAZ. High magnification **(d)** Fusion zone. High magnification

Figure 4.24: Fracture surfaces of the HAZ tensile specimen orientated longitudinal to the welding direction.

The overview in Figure 4.24a represents the heat-affected zone of the HAZ tensile specimen. This part of the specimen has a relatively even fracture surface with some contraction at the specimen surface towards the fusion zone. According to Figure 4.24c, a line pattern reflecting the fibrous grain structure can be seen.

The overview in Figure 4.24b represents the fusion zone of the HAZ tensile specimen. The fracture surface is rough with some elevated areas at the specimen surface. According to Figure 4.24d, the fracture surface is covered by large dimples with a high density of small dimples in-between the large ones. It appears that the fracture surface is a combination of the fracture surfaces found for the FZ tensile specimens representing the transverse and longitudinal direction (Figures 4.22c and 4.22d, respectively).

4.4.2 FSW

The base metal used in the tensile testing was AA6082-T6 for both welding techniques. But due to some unknown differences in the mechanical properties, fractography of the base metal have been performed for both the FS and the GMA tensile specimens.

Figure 4.25 shows the fracture surfaces of the BM tensile specimens representing the transverse and the longitudinal direction. In the overviews of the fracture surfaces only one side of the specimen is presented. Additional overview of the opposite sides can be found in Figure A.17 in the Appendix.

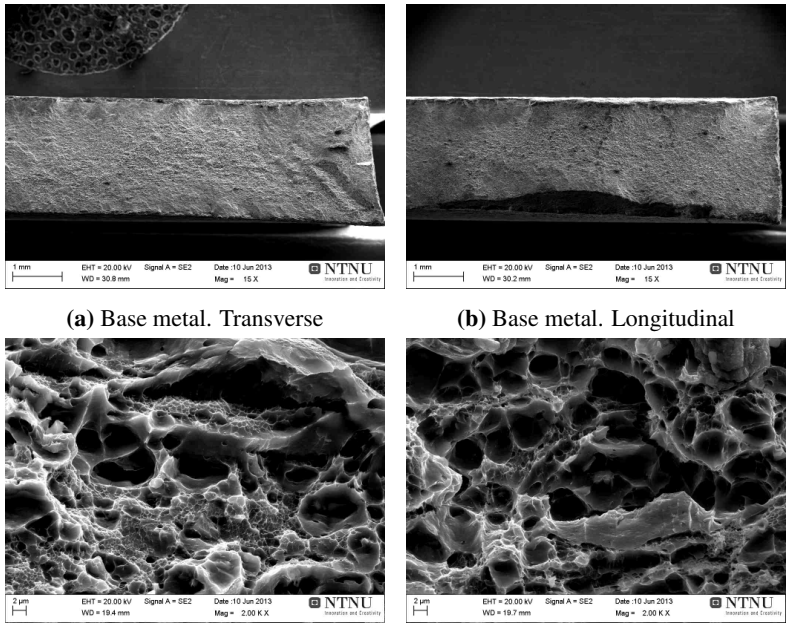

(a) Base metal. Transverse

(b) Base metal. Longitudinal

(c) BM-T. High magnification

(d) BM-L. High magnification

Figure 4.25: Fracture surfaces of the BM tensile specimens representing the transverse and the longitudinal direction.

Figure 4.25a represents the BM tensile specimen transverse to the welding/extrusion direction. The specimen surface has an overall plane appearance, with only small variations in the area reduction towards the edges. The specimen surface seems to be less ductile compared to the other parts of the specimen. This is confirmed by Figure A.18 in the Appendix, which show signs of less plastic deformation. According to Figure 4.25c, the fracture surface in the center of the specimen is covered with three different types of dimples. A small amount of large dimples are surrounded by smaller dimples. In addition, there is a high density of very small dimples less than 1 μm.

Figure 4.25b represents the BM tensile specimen orientated longitudinal to the welding/extrusion direction. The specimen surface is more uneven (fibrous) compared to that of the BM-T tensile specimen. In addition, this specimen appears to have a larger area at the specimen surface with less ductility (plastic deformation). This also concerns other parts of the specimen, as shown in Figure 4.26, which includes a close-up of the outlined area from the center of the specimen.

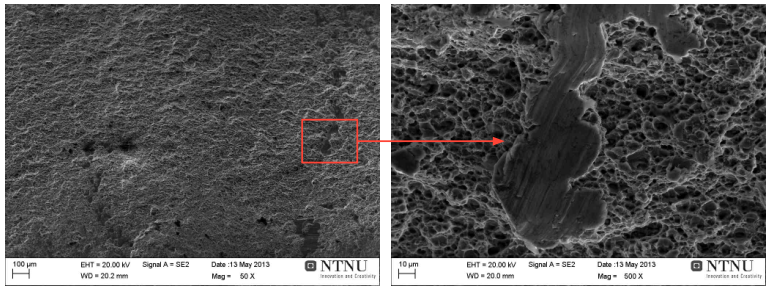

Figure 4.26: Outlined area in the BM tensile specimen representing the longitudinal direction. The outlined part shows signs of less plastic deformation compared to the surrounding material.

From Figure 4.26, a line pattern with less plastic deformation, compared to the surrounding material, can be observed. This line pattern goes through the whole width of the specimen. Several similar observations have been found across the fracture surface.

Figure 4.27 shows the fracture surfaces of the SZ tensile specimens representing the transverse and the longitudinal direction. In the overviews of the fracture surfaces only one side of the specimen is presented. Additional SEM images of the opposite sides can be found in Figure A.19 in the Appendix.

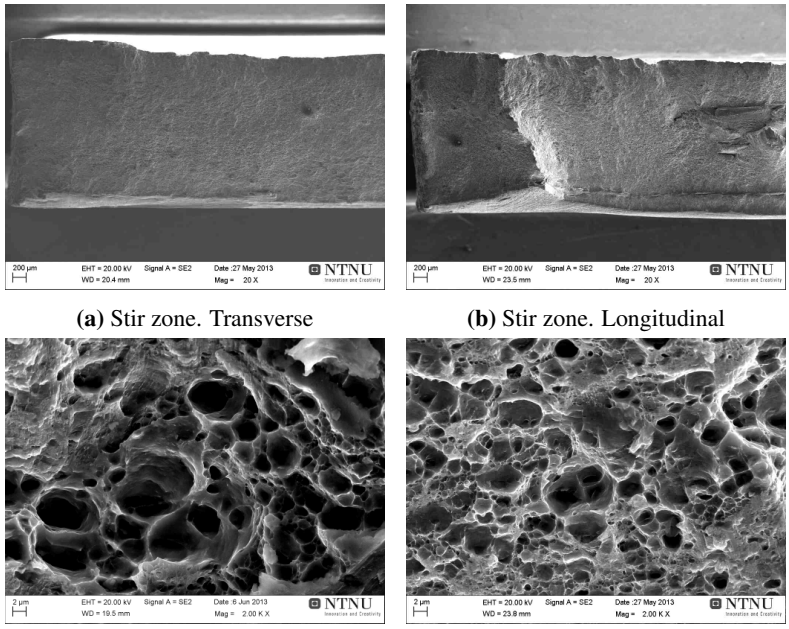

(a) Stir zone. Transverse

(b) Stir zone. Longitudinal

(c) SZ-T high magnification

(d) SZ-L high magnification

Figure 4.27: Fracture surfaces of the SZ tensile specimens transverse and longitudinal to the welding/extrusion direction.

Figure 4.27a represents the fracture surface overview of the weakest part of the HAZ/TMAZ region. The only contraction observed is in the center of the specimen. According to Figure 4.27c, the fracture surface is covered by a relatively large amount of large dimples being decorated with smaller dimples in-between. Some areas with less plastic deformation can be observed in-between the dimples.

Figure 4.27b represents the fracture surface overview of the stir zone (SZ) and parts of the HAZ/TMAZ region (at the edges). The fracture surface show signs of shear failure at the edges, which corresponds to the HAZ/TMAZ region. This region appears to be less ductile compared to the other part of the specimen. According to Figure 4.27d, the fracture surface is covered by some medium large dimples (2-5 μm) with a higher density of smaller dimples in-between. This specimen has an overall higher density of dimples in the fracture surface compared to the SZ-T specimen.

In the center of the tensile specimen, where the stir zone is very visible, the fracture surface is rough and uneven due to severe plastic deformation. Figure 4.28 shows the stir zone of the tensile specimen representing the longitudinal direction, including outlined close-ups of the different regions found within the stir zone.

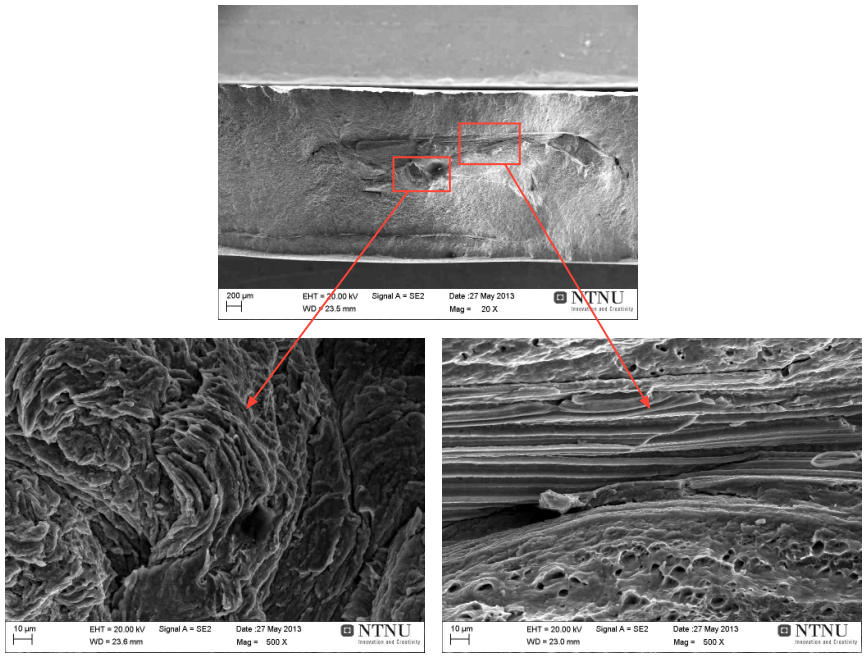

Figure 4.28: Close-ups of the fracture surfaces in the stir zone.

From Figure 4.28 the stir zone appears to consist of different structures. In the close-up at the bottom left in the figure, the material has been stirred together. There are no signs of dimples. In the close-up at the bottom right in the figure, the fibrous structure of the alloy is still visible. Some small dimples can be observed above and below the lamellar

structure. Additional images of the fracture surfaces observed in the stir zone can be found in Figure A.20 in the Appendix.

Figure 4.29 shows the fracture surface of the HAZ/TMAZ tensile specimen representing the longitudinal direction. This specimen also includes some parts of the stir zone.

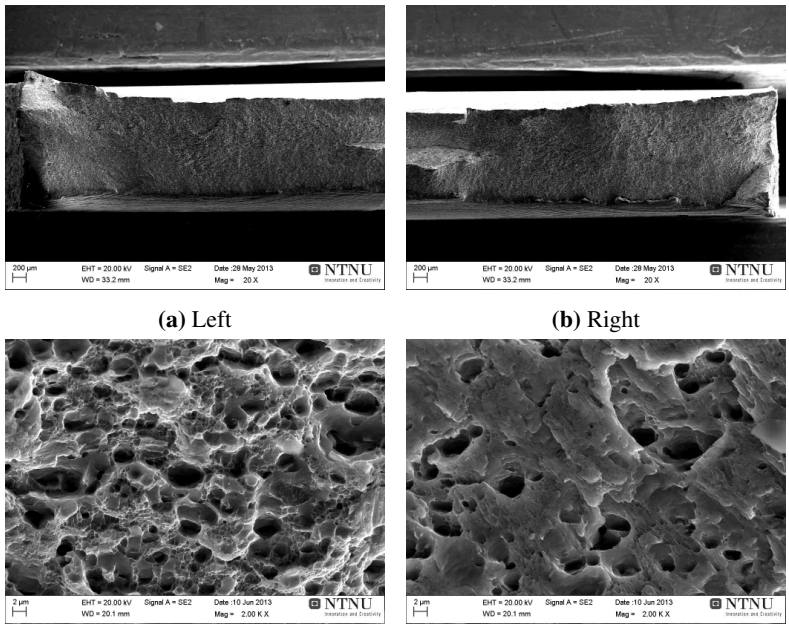

(a) Left **(b)** Right

(c) High magnification **(d)** Edge. High magnification

Figure 4.29: Fracture surfaces of the HAZ/TMAZ tensile specimen representing the longitudinal direction.

Figures 4.29a and 4.29b show overviews of the HAZ/TMAZ tensile specimen orientated longitudinal to the welding/extrusion direction. The edges and the center of the specimen show signs of shear failure. And the specimen surface has contracted more towards the center. According to Figure 4.29c the overall fracture surface is covered with medium large dimples with smaller dimples in-between.

Figure 4.29d represents the fracture surface at the edges and in the center of the specimen, where the material has experienced a different course of fracture. These parts appear to be less ductile compared to the rest of the specimen due to the low density of dimples.

4.5 Charpy V-notch test results

4.5.1 GMAW

Figure 4.30 shows macro images of a selection of the GMAW Charpy V-notch specimens. The figure includes images of the base metal specimens representing the transverse and longitudinal specimen orientations, a FZ specimen with notch orientation in the center of the fusion zone, and a HAZ specimen representing the longitudinal specimen orientation.

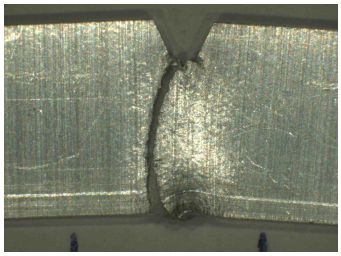

(a) Base metal. Transverse specimens orientation.

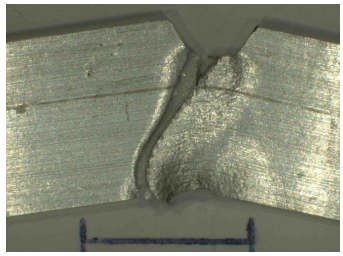

(b) Base metal. Longitudinal specimen orientation.

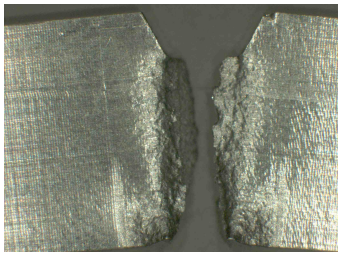

(c) Fusion zone

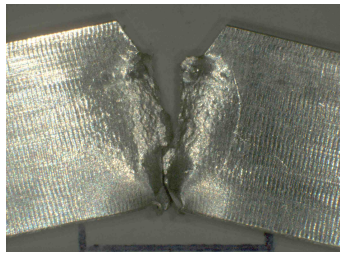

(d) HAZ

Figure 4.30: Macro images of the GMAW Charpy V-notch specimens after testing.

As seen from Figure 4.30, all the Charpy V-notch specimens appear to have a different course of fracture. The transverse BM specimen in Figure 4.30a has a fracture path, which is essentially parallel to the extrusion direction. While the longitudinal BM specimen in Figure 4.30b has a form for cup-and-cone fracture, where the fracture propagates diagonally to the extrusion direction. Both the FZ and the HAZ specimen seem to have a more rough fracture appearance. These specimens also show signs of some macroscopic deformation.

Figure 4.31 shows the energy absorption of the same GMA Charpy specimens presented above obtained using the Charpy V-notch test. The numerical values can be found in Table A.9 in the Appendix together with the results for the other specimens tested.

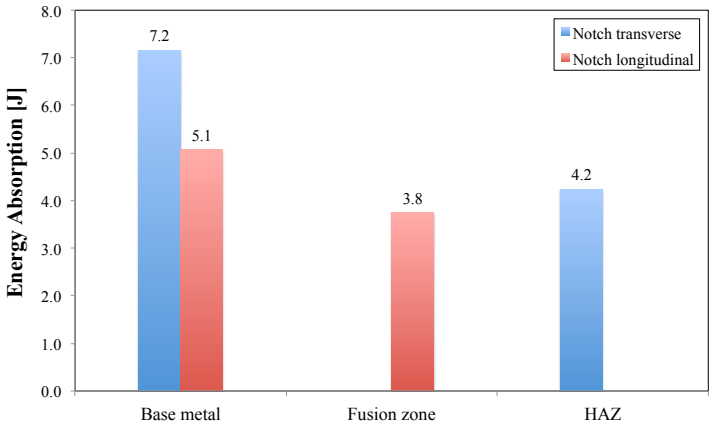

Figure 4.31: Energy absorption of the GMAW Charpy specimens presented in Figure 4.30.

It follows from Figure 4.31 that the BM specimen with the notch transverse to the extrusion direction absorbed most energy, followed by the BM specimen with the notch orientated longitudinal to the extrusion direction. The measured values was 7.2 and 5.1 J, respectively. Significantly lower values are observed for the FZ and HAZ specimens. These results are also supported by the macro images, where the FZ and HAZ specimens seem to behave more brittle.

Figures 4.32 to 4.35 show the fracture surfaces of the Charpy specimens (as presented above) after testing. The figures include an overview of the fracture surfaces and an outlined area at higher magnification. This area corresponds to the notch, where fracture is initiated.

Figure 4.32 shows an overview of the BM Charpy specimen representing the transverse specimen orientation.

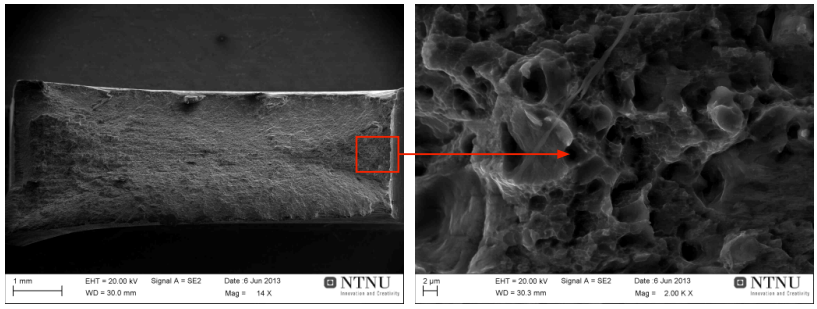

Figure 4.32: Fracture surface of the BM specimen representing the transverse specimen orientation, including an outlined area at higher magnification. The crack propagates from right to left. (The scale bars in the lower left corner are 1 mm and 2 μm, respectively).

The overview of the BM-T specimen fracture surface, shown in Figure 4.32, indicates a larger area where the crack has propagated. This area is visible in the image to the left, and it has a triangular appearance. The fracture surface at the crack opening (close to the notch) shows signs of some medium large dimples with smaller dimples in-between. The dimples are not as distinctive as those found in the tensile test specimens.

Figure 4.33 shows the an overview of the BM Charpy specimen representing the longitudinal specimen orientation.

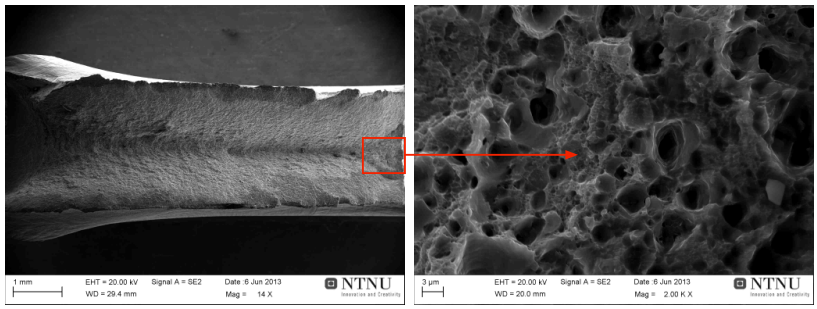

Figure 4.33: Fracture surface of the BM specimen representing the longitudinal specimen orientation, including an outlined area at higher magnification. The crack propagates from right to left. (The scale bars in the lower left corner are 1 mm and 3 μm, respectively).

The overview of the BM-L specimen in Figure 4.33 shows that the surface is V-shaped and there is some signs of fibrous pull out at the specimen surface. The thickness of the specimen has contracted more compared to the BM-T specimen, due to more compression at the end of the crack. This observation is also consistent with the energy absorption measurements, where the BM-L specimen obtained higher impact values. The fracture surface of the specimen is covered with relatively small dimples (2 μm), with even smaller dimples (less than 1μm) in between.

Figure 4.34 shows an overview of the FZ Charpy specimen representing the fusion zone.

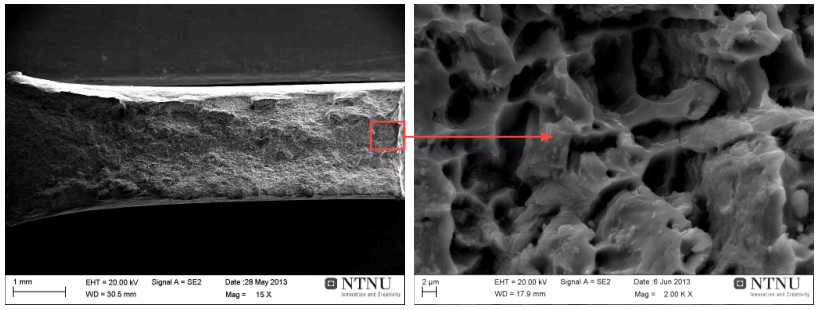

Figure 4.34: Fracture surface of the FZ specimen, including an outlined area at high magnification. The crack propagates from right to left. (The scale bars in lower left corner are 1mm and 2 μm, respectively).

The overview of the FZ specimen fracture surface in Figure 4.34 indicates that the fracture has propagated in a more brittle manner compared to the BM specimens. Still, there are some visible signs of compression at the edge of the crack. The point where fracture is initiated does not have the same characteristics as for the BM specimens. The rough surface indicates that the weldment has a different extent of ductility throughout the specimen. At the initiation point of the crack, small dimples, as observed in the fracture surface of the BM specimens, are no longer present. This is consistent with the energy absorption measurements, where this specimen absorbed less energy compared to the other specimens tested.

Figure 4.35 shows an overview of the HAZ Charpy specimen representing the longitudinal specimen orientation. The figure includes a close-up of the fracture surface adjacent to the notch.

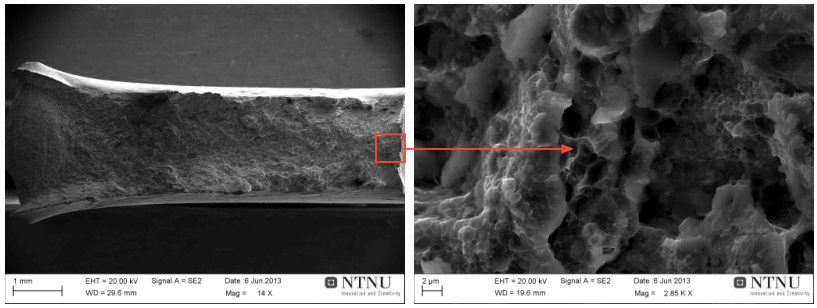

Figure 4.35: Fracture surface of the HAZ specimen, including an outlined area at high magnification. The crack propagates from right to left. (The scale bars in lower left corner are 1mm and 2 μm, respectively).

The fracture surface overview of the HAZ Charpy specimen in Figure 4.35 appears to be quite similar to the FZ specimen, where an overall rough fracture surface can be observed. This is also consistent with the energy absorption measurements. Still, there are some small differences in the close-up of the fracture surfaces. In this case the HAZ specimen shows more distinctive signs of smaller dimples.

All the fracture surface observations are consistant with ductile fracture, although there are some differences in density of dimples and nature of the crack propagation.

Figure 4.36 shows fracture surface images at high magnification of the GMAW Charpy V-notch specimens presented above. The images represent the fracture surfaces in the center of the specimens, a certain distance away from the notch.

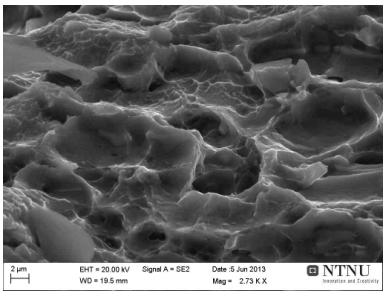

(a) Base metal. Notch longitudinal to extrusion direction

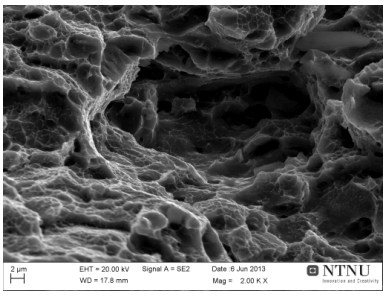

(b) Base metal. Notch normal to extrusion direction

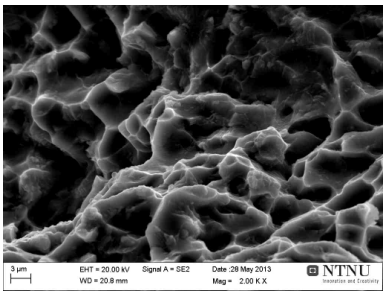

(c) Fusion zone

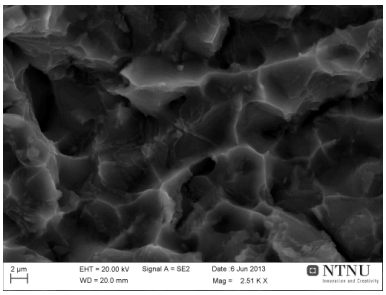

(d) HAZ

Figure 4.36: Fracture surfaces of the GMAW Charpy V-notch specimens.

The close-ups of the fracture surfaces of the Charpy specimens in Figure 4.36 represent the fracture surfaces approximately in the center of the specimens. The fracture surface images support the previous observations that the BM Charpy specimens have higher ductility compared to the FZ and the HAZ specimens. This is based on a consideration of the density of dimples and the measured energy absorption.

4.5.2 FSW

Figure 4.37 shows macro images of a selection of the FSW Charpy V-notch specimens after testing. The figure includes images of base metal specimens representing the transverse and the longitudinal specimen orientations, a SZ specimen with notch in the center of the stir zone, and a HAZ/TMAZ specimen representing the longitudinal specimen orientation.

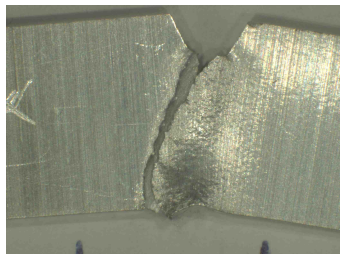

(a) Base metal. Transverse specimen orientation.

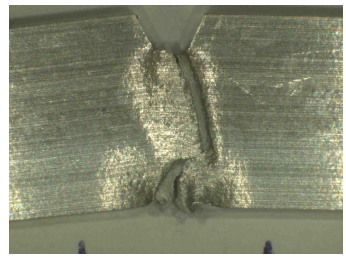

(b) Base metal. Longitudinal specimen orientation.

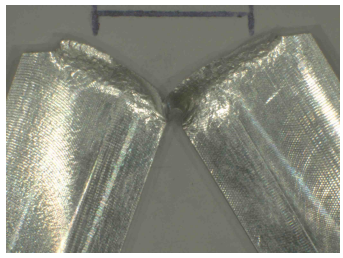

(c) Stir zone (SZ)

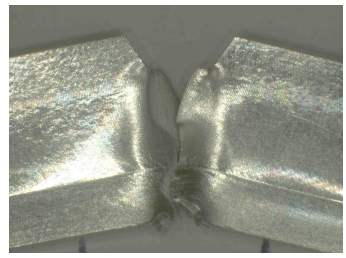

(d) HAZ/TMAZ

Figure 4.37: Macro images of the FSW Charpy V-notch specimens after testing.

It i evident from Figure 4.37 that all specimens exhibit different fracture appearances. The BM specimen shown in Figure 4.37a has a fracture path diagonal to the extrusion direction. While the other BM specimen (Figure 4.37b) and the HAZ/TMAZ specimen (Figure 4.37d) have more uneven fracture paths. These specimens have the notch orientated transverse to the extrusion direction. Still, some similarities in the fracture paths can be found at the end of the crack. The major difference is the location of the notch, where parts of the HAZ/TMAZ specimen notch is located at the end of the stir zone. The SZ Charpy specimen (Figure 4.37c) was the only specimen still being unbroken after testing (this is true for two of three parallels). All the specimens show signs of compression at the end of the crack.

In general, the fracture appearances of the FS Charpy specimens are different compared to the GMA Charpy specimens. Also the base metal specimens are different.

Figure 4.38 shows the energy absorption of the selected FS Charpy specimens obtained using the Charpy V-notch test. In addition, the results for all the specimens tested can be found in Table A.10 in the Appendix.

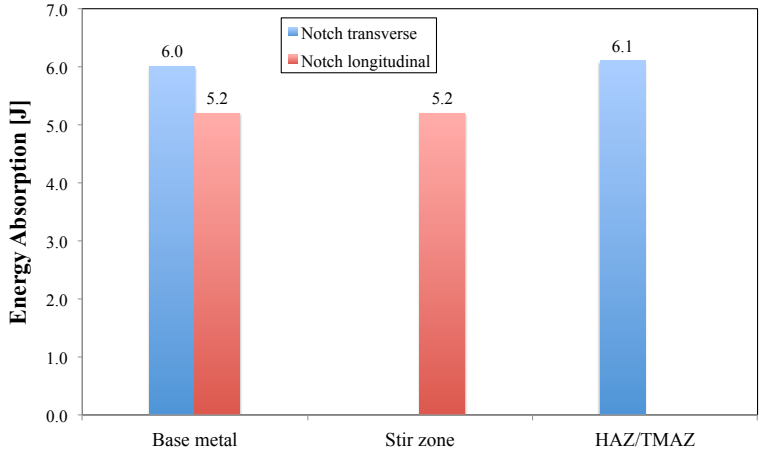

Figure 4.38: Energy absorption of the FSW Charpy specimens presented in Figure 4.37.

It is evident from Figure Figure 4.38 that the BM specimen with the notch orientated transverse to the extrusion direction, and the HAZ/TMAZ specimen absorbed most energy, with measured values of 6.0 and 6.1 J, respectively. As already mentioned, the SZ specimen was still unbroken after testing, although the energy absorption was lower compared to many of the other specimens.

Despite some differences in fracture appearance, the base metal Charpy specimens for both FSW and GMAW had similar values of energy absorption, with only a slight difference between the BM specimens with the notch orientated transverse to the extrusion direction. The SZ specimen absorbed more energy compared to the FZ specimen. And the HAZ/TMAZ specimen absorbed more energy compared to the GMAW HAZ specimen.

Figures 4.39 to 4.42 show the fracture surfaces of the FSW Charpy specimens (presented above) after testing. The figures include an overview of the fracture surfaces with an outlined area at higher magnification. This area corresponds to the notch, where fracture initiates.

Figures 4.39 shows the fracture surface overview of the BM Charpy specimen representing the transverse specimen orientation.

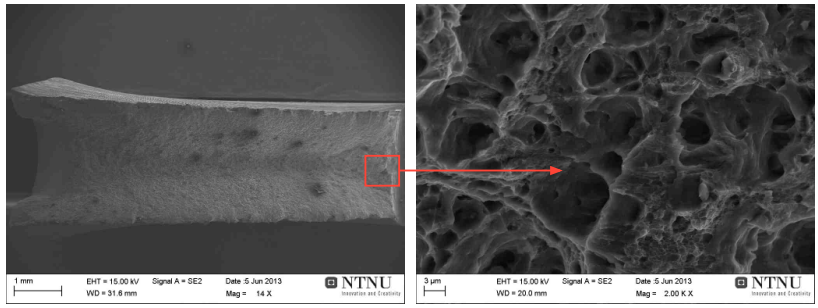

Figure 4.39: Fracture surface of the BM specimen representing the transverse specimen orientation, including an outlined area of the notch at high magnification. The crack propagates from right to left. (The scale bars in lower left corner are 1mm and 3 μm, respectively).

The overview of the BM specimen in Figure 4.39 shows little or no signs of contraction (reduction in area) at the specimen surface. Still, there is some degree of compression at the end of the crack. A vague line can be seen from which the crack initiates and propagates throughout the specimen. The crack has propagated in the same manner as for the GMAW BM Charpy specimen representing the same specimen orientation (see Figure 4.32). The fracture surface at the notch is covered by relatively large dimples being surrounded by smaller dimples in-between the large ones.

Figure 4.40 shows the fracture surface overview of the BM Charpy specimen representing the longitudinal specimen orientation.

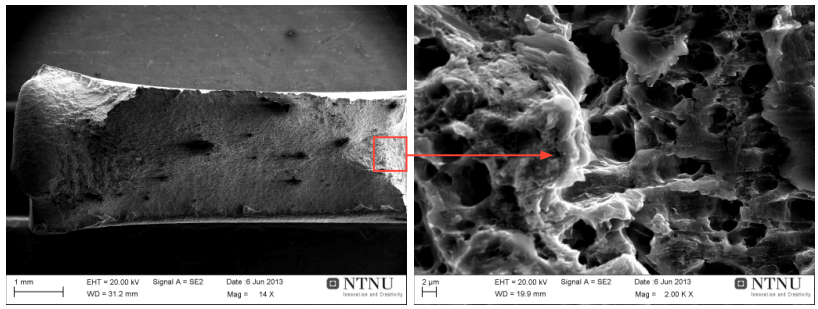

Figure 4.40: Fracture surface of the BM specimen representing the longitudinal specimen orientation, including an outlined area of the area of the notch high magnification. The crack propagates from right to left. (The bars in lower left corner are 1mm and 2 μm, respectively).

In Figure 4.40, the point where the crack has initiated is visible. The specimen has experienced little reduction in area, but there are some signs of contraction/expansion at the end of the crack. It appears that the close-up of the fracture surface at the crack opening have

been taken closer to the bottom of the notch. In this area less plastic deformation can be observed.

Figure 4.41 shows the fracture surface overview of the SZ Charpy specimen, where the notch is located in the joint.

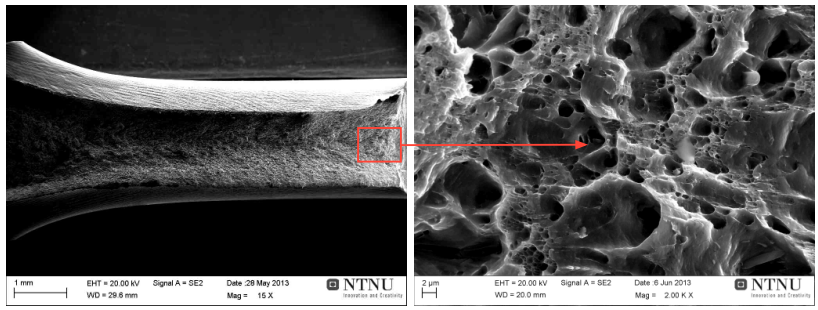

Figure 4.41: Fracture surface of the SZ specimen, including an outlined area at high magnification. The crack propagates from right to left. (The scale bars in lower left corner are 1mm and 2 μm, respectively).

The overview of the SZ specimen fracture surface in Figure 4.41 shows that the specimen surface across the whole specimen has undergone plastic deformation during testing. This is confirmed by the visible reduction in area, and the obvious compression/expansion at the end of the crack. As stated previously, this specimen was still intact after testing, which explains the large expansion at the edge of the crack. The fracture surface at the crack opening is covered with different types of dimples, i.e. some large dimples (5-10 μm) being surrounded by smaller ones in-between.

Figure 4.42 shows a fracture surface overview of the HAZ/TMAZ Charpy specimen representing the longitudinal direction.

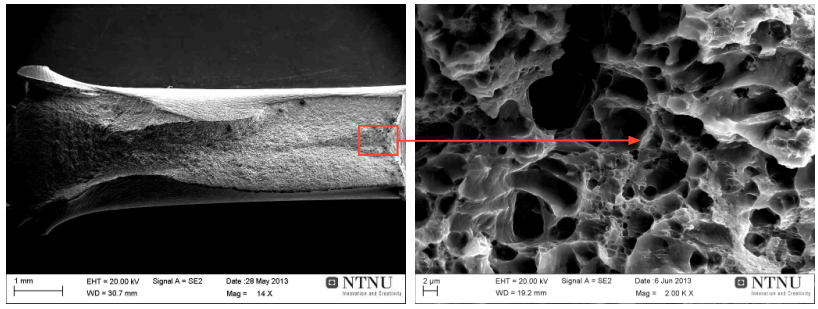

Figure 4.42: Fracture surface of the HAZ/TMAZ Charpy specimen representing the longitudinal specimen orientation. The crack propagates from right to left. (The bar in the lower left corner is 1mm and 2 μm,respectively.

It follows from Figure 4.42 that the surface has been affected by the test to a different extent across the specimen. Reduction in area is most evident towards the end of the crack, where severe compression/expansion has plastically deformed the surrounding material. At the notch, the fracture surface is covered by dimples similar to the FZ specimen. The largest dimples are not present in the HAZ/TMAZ specimen. The crack has propagated from the center of the notch.

Figure 4.43 shows the fracture surfaces of the same FSW Charpy specimens presented above. These images are representative of the fracture surfaces in the center of the specimens, at a certain distance away from the notch.

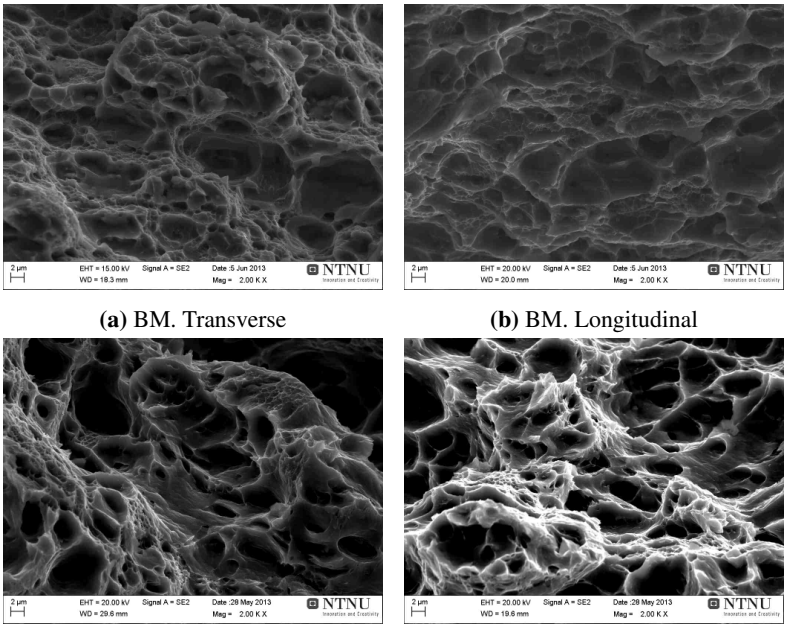

(a) BM. Transverse **(b)** BM. Longitudinal

(c) Stir zone **(d)** HAZ/TMAZ

Figure 4.43: Fracture surfaces images of the FSW Charpy V-notch specimens after testing. (The scale bar in the lower left corner is 2 μm)

The transverse BM Charpy specimen in Figure 4.43a appears to have a fracture surface covered by dimples of different sizes. Some larger dimples with faceted appearance are surrounded by smaller dimples. The same is also observed for the longitudinal BM specimen. But in this case the fracture surface has a higher density of large dimples. The SZ and HAZ/TMAZ Charpy specimens (Figures 4.43c and 4.43d) appear to have similar fracture surfaces despite the pertinent difference in the energy absorption. Both specimens have a high density of small dimples surrounding the larger dimples, but the HAZ/TMAZ specimen has an overall higher dimple density.

Chapter 5

Discussion

In the following chapters, the results from the hardness, tensile and Charpy V-notch testing will be discussed and analyzed. The mechanical properties of the GMA and FS weldments obtained in the tensile and the Charpy V-notch testing will be compared. The hardness profiles have been used to calculate the HAZ yield stress profiles, and the results will be compared with the yield stress measured in the tensile testing. This analysis is accompanied by a case study of the load-bearing capacity of the joints.

5.1 Comparison of mechanical properties between the GMA and the FS weldments

To keep the HAZ and the HAZ/TMAZ tensile specimens separated, the HAZ/TMAZ tensile specimens, as defined in the results, have been redefined as TMAZ.

Figure 5.1 shows a comparison in the average stress at offset yield between the GMAW and FSW tensile specimens representing the transverse and the longitudinal direction, respectively.

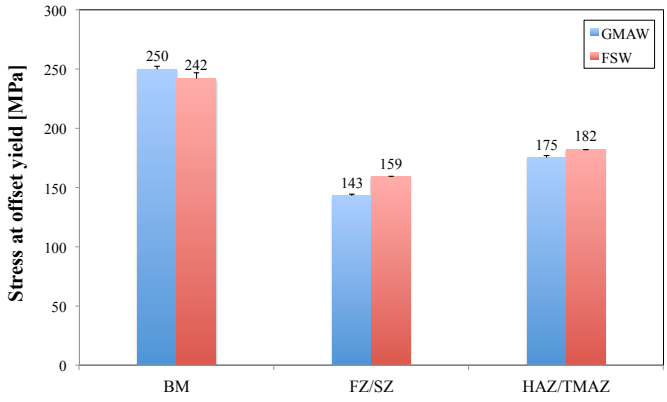

(a) Transverse

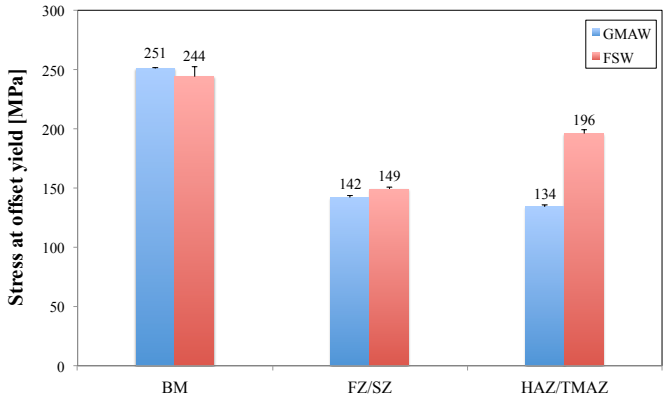

(b) Longitudinal

Figure 5.1: Average stress at offset yield for the FS and the GMA tensile specimens representing the transverse and the longitudinal direction, respectively. (The error bars represent the standard deviation).

The yield stress for the BM tensile specimens, shown in Figure 5.1a and 5.1b, indicates a small but significant difference in the base metal yield stress in both directions. This can be a result of the sheets being heat-treated separately. And this is a general observation of the base metal, also in the following results. Moreover, it is evident that the welds experience severe strength reduction in the HAZ, as confirmed by the cross-weld tensile specimens. The strength reduction in the GMA and the FS welds was approximately 43 and 34%, respectively. The HAZ/TMAZ specimens tested in the transverse direction were similar to the FZ/SZ specimens. The difference was that the HAZ/TMAZ tensile specimens only covered one side of the weld. Based on this, it is not certain that all the parallels covered the softest part of the HAZ. Therefore, the calculations of strength reduction are based on the FZ/SZ tensile specimens representing the transverse direction.

The HAZ and the TMAZ tensile specimens tested in the longitudinal direction were supposed to sample the weakest part of HAZ. But it was not possible to cut the samples from the sheets without including parts of the weld zone. The FZ and the SZ tensile specimens representing the longitudinal direction were also slightly undefined, since the dimensions of the specimens were too large to only cover the weld. This can explain some of the varying results obtained for the HAZ/TMAZ and the FZ/SZ specimens tested in the longitudinal direction.

Figure 5.2 shows the average tensile strength for the FS and the GMA welds in the transverse and the longitudinal direction, respectively.

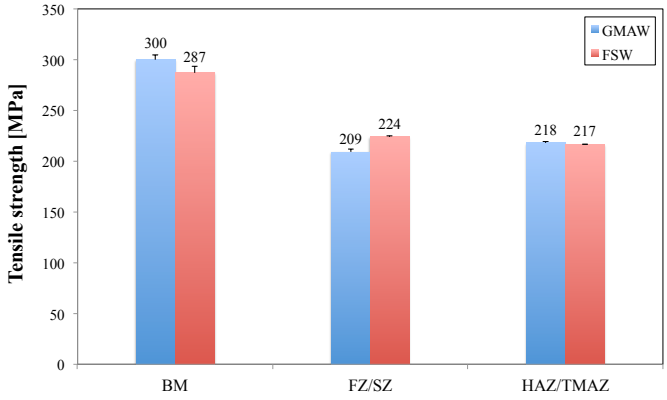

(a) Transverse

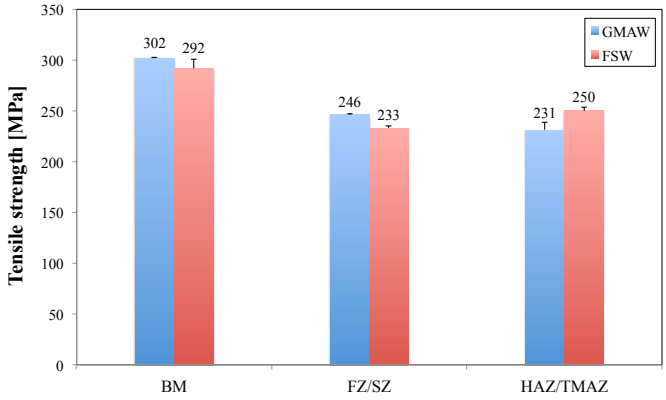

(b) Longitudinal

Figure 5.2: Average tensile strength for the FS and the GMA welds in the transverse and the longitudinal direction, respectively. (The error bars represent the standard deviation).

As shown in Figure 5.2, there are no major differences in tensile strength between the two types of welds. But a strength reduction in the welds is also evident here. The reduction in tensile strength for the GMA and the FS weld is approximately 30 and 22%,

respectively.

Tensile strength reflects the work hardening behavior of the material, i.e. the maximum stress before it breaks. In engineering design yield stress is more important, since it is a measure of the materials ability to deform plastically.

Figure 5.3 shows the average strain at fracture for the FS and the GMA tensile specimens representing the transverse and the longitudinal direction, respectively.

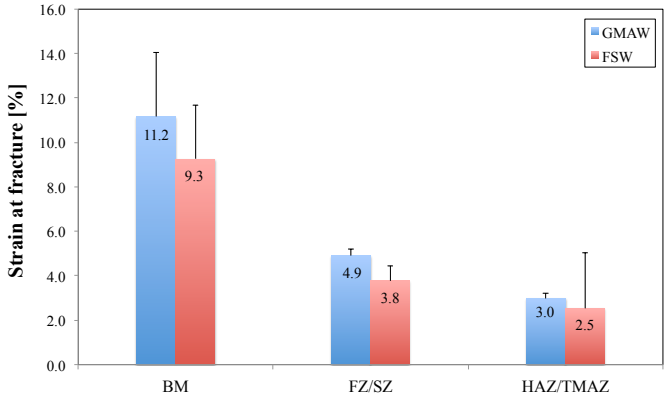

(a) Transverse

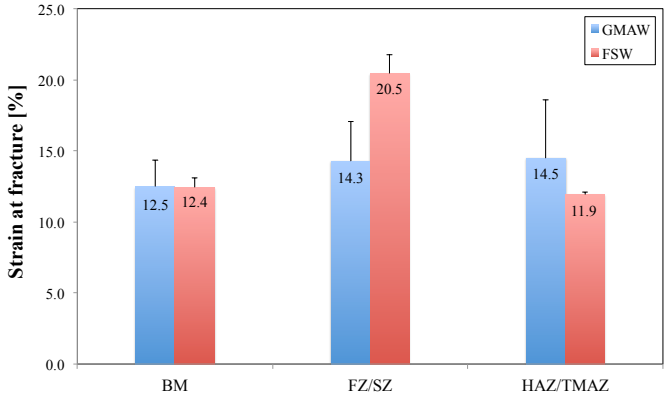

(b) Longitudinal

Figure 5.3: Average strain at fracture for the FS and the GMA tensile specimens representing the transverse and the the longitudinal direction, respectively. Note that the axis have different scaling. (The error bars represent the standard deviation).

As shown in Figure 5.3, a reduction in strain at fracture can be observed for the cross-weld tensile specimens. In this case the reduction in strain at fracture for the GMA and the FS weldments is 56 and 59%, respectively. This shows that the FS welds fracture first, which is slightly deviant when considering the higher HAZ strength levels observed for these

weldments. Furthermore, it can be observed from Figure 5.3b that the joints have a higher strain at fracture compared to the base metal.

Figure 5.4 shows the average reduction in area for the FS and the GMA tensile specimens representing the transverse and the longitudinal direction, respectively.

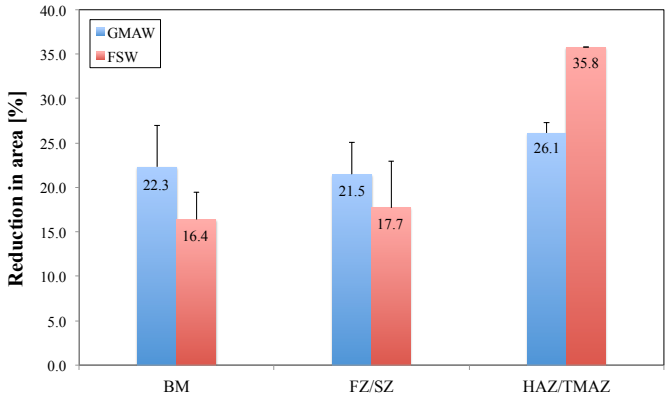

(a) Transverse

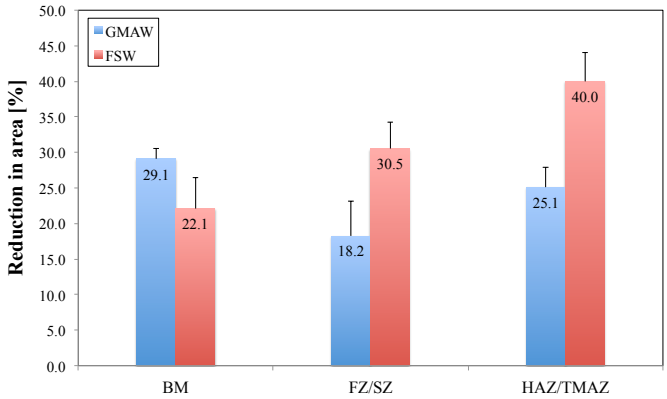

(b) Longitudinal

Figure 5.4: Average reduction in area for the FS and the GMA tensile specimens representing the transverse and the the longitudinal direction, respectively. (The error bars represent the standard deviation).

The reduction in area is a more accurate measure of ductility compared to strain at fracture, since it accounts for the material contraction in both directions of the specimen. As shown in Figure 5.13a, the reduction in area for the cross-weld specimens is close to that of the base metal. The FS welds show even higher values compared to the base metal. This shows that low strain at fracture found for the cross-weld specimens is not necessarily a sign of low ductility.

Figure 5.5 shows the average energy absorption of the GMA and the FS Charpy V-notch specimen.

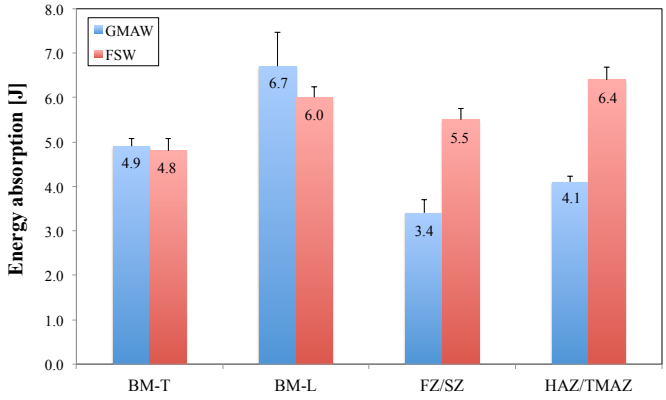

Figure 5.5: Average energy absorption of the FS and the GMA Charpy V-notch specimen.

As shown in Figure 5.5, the average energy absorption of the GMA and the FS weldments is in general very low. But it gives a basis for comparing the base metal and the welds. As expected, the FZ specimen absorbed less energy compared to all the other specimens. This is basically because the fusion zone is in a so-called as-cast state, which affects the ductility.

Table 5.1 summarizes the reduction/increase in mechanical properties of the GMA and the FS weldments, considering the differences between the cross-weld tensile specimens and the base metal. Here, red numbers represent reduction, while blue numbers represent increase.

Table 5.1: Summary of the reduction/increase in mechanical properties of the joints, based on an evaluation of the cross-weld tensile specimens.

Reduction/increase [%]	**Welding technique**	
	GMAW	**FSW**
Yield stress	43	30
Tensile strength	30	22
Strain at fracture	56	59
Reduction in area	0.36	0.8
Energy absorption	0.31	0.15

Table 5.1 shows that the FS weldments in general have better mechanical properties compared to the GMA weldments. And even a small increase in the reduction in area of the FS cross-weld tensile specimens can be observed. The same is also true for the energy absorption in the welds.

5.2 Hardness profiles and yield stress

5.2.1 Comparison of the hardness profiles

Figure 5.6 shows a comparison of the resulting hardness profiles for the GMA and the FS weldments, where the total width of the HAZ is indicated by the dashed lines.

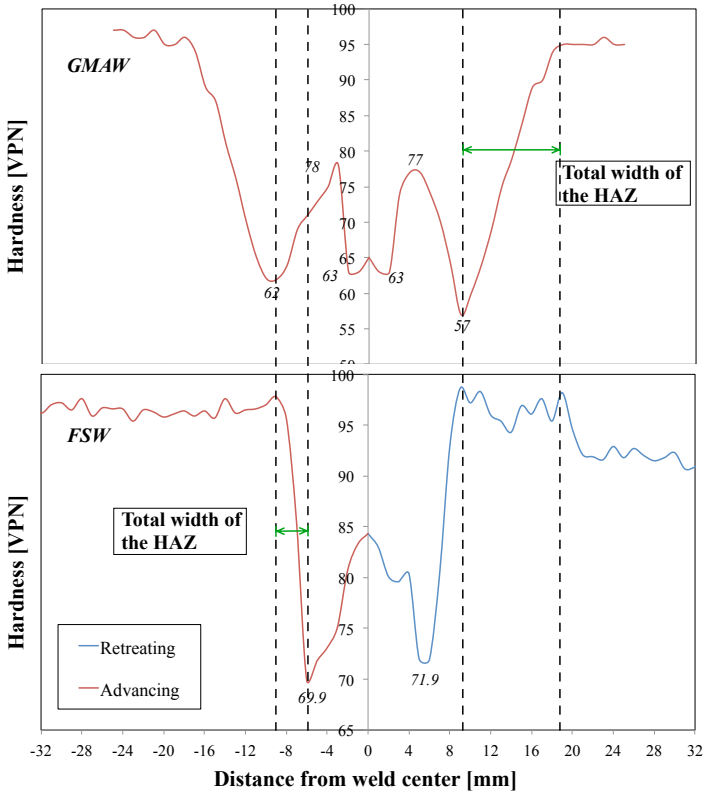

Figure 5.6: Comparison of the hardness profiles for the GMA and the FS weldments. The dashed lines are indicating the total width of the HAZ.

This comparison shows that the HAZ for the GMA weldments is much wider than for the FS weldments. The minimum HAZ hardness of the GMA weldments is located at the

same distance from the center of the weld where full recovery of the base metal hardness of the FS weldments can be observed. But in despite of the large difference in the width of the HAZ, both welding techniques give a considerable HAZ strength reduction.

In Figure 5.7, a macro image of a GMA welded tensile specimen oriented transverse to the welding direction is shown.

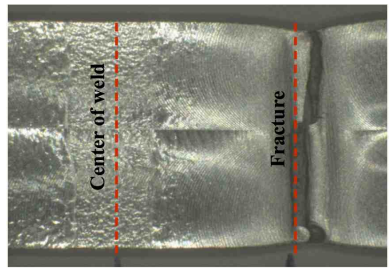

Figure 5.7: Macro image of a GMA tensile specimen oriented transverse to the welding direction. The dashed lines indicate the location of the center of the weld and the location of the fracture.

It is evident from Figure 5.7 that the fracture is located approximately 10 mm from the center of the weld. This corresponds to the location of the minimum HAZ hardness from the hardness profile.

Figure 5.8 shows a macro image of a FS tensile specimen oriented transverse to the welding direction. The location of the fracture is indicated in the image.

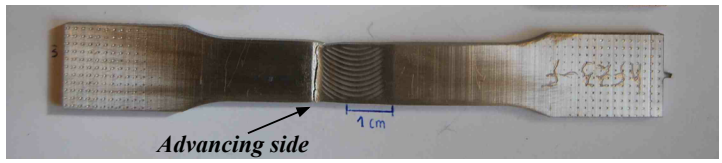

Figure 5.8: Macro image of a FS tensile specimen oriented transverse to the welding direction. The location of the fracture is indicated.

In agreement with the HAZ hardness profile in Figure 5.6, necking of the transverse SZ tensile specimens occurs in the weakest part of the weld (at or close to the HAZ/TMAZ boundary). This is true for all the cross-weld SZ tensile specimens tested (see Figure A.11b in the Appendix), and it is supported by observations of others [14, 46].

The pertinent difference in the HAZ width between GMAW and FSW can also be explained by considering the peak temperature distribution around the welds. Figures 5.9 and 5.10 show schematic illustrations of the response of a peak-aged Al-Mg-Si alloy to GMAW and FSW, respectively. The sketches are correlations between the peak-temperature (T_p) distribution around the weld and the quasi-binary Al-Mg_2Si phase diagram. A final sketch of the strength profile after complete natural ageing is also included.

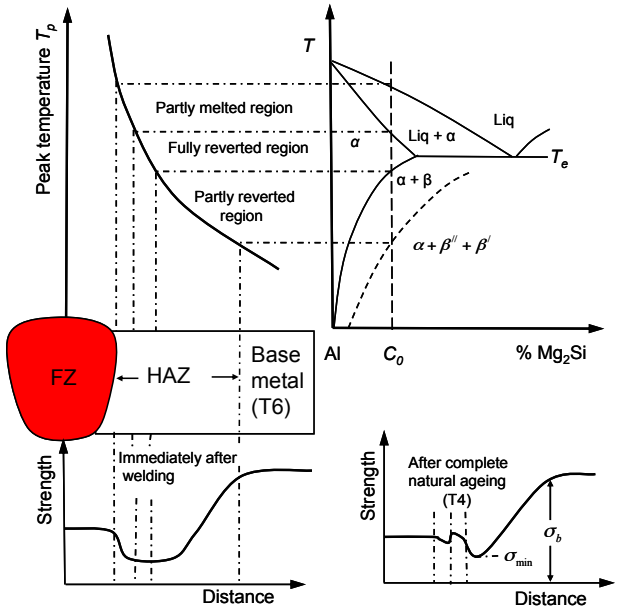

Figure 5.9: Schematic illustration of the response of a peak-aged Al-Mg-Si alloy to GMAW [5].

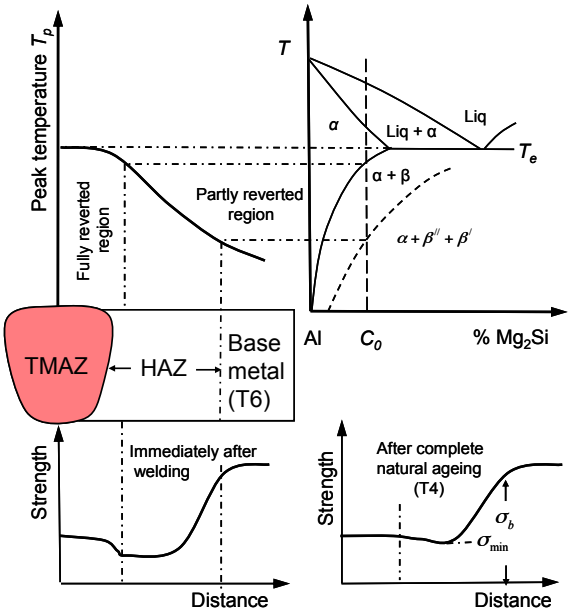

Figure 5.10: Schematic illustration of the response of a peak-aged Al-Mg-Si alloy to FSW [5].

In GMA weldments, as illustrated in Figure 5.9, the hardening β'' and β' precipitates present in the partly reverted region, after artificial ageing, become thermodynamically unstable and start to dissolve. This is causing a strength reduction in the material close to/at the fusion line [5]. This can be observed in Figure 5.6, at the point where the hardness drops to 63 HV. In addition, some strength recovery may occur between the fusion line and the minimum HAZ hardness, due to following natural ageing of the material in as-welded condition. This is also observed in Figure 5.6, at the point where the hardness reach approximately 77 HV.

In the FS weldments, as illustrated in Figure 5.10, the FZ is replaced by a TMAZ where the partly melted region is eliminated. This is because the peak temperature in FSW, in practice, never exceeds the eutectic temperature T_e [5, 14]. By eliminating the partly reverted region, the total width of the HAZ in FS weldments becomes smaller compared that observed in the GMA weldments.

5.2.2 Relationship between hardness profiles and yield stress

Figure 5.11 shows the resulting yield stress profiles based on the HAZ hardness profiles, using Equation 2.3 found in Chapter 2. The figure includes plotted values for the base metal yield stress σ_b, and the minimum HAZ yield stress σ_{min}. In addition, all the calculated yield stress values can be found in Tables A.11 and A.12 in the Appendix.

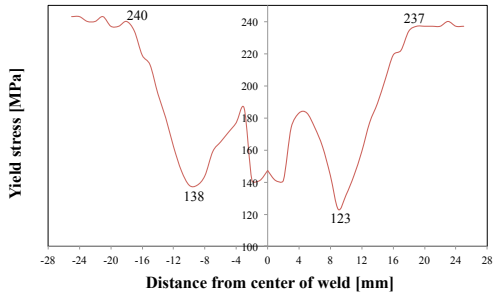

(a) GMAW

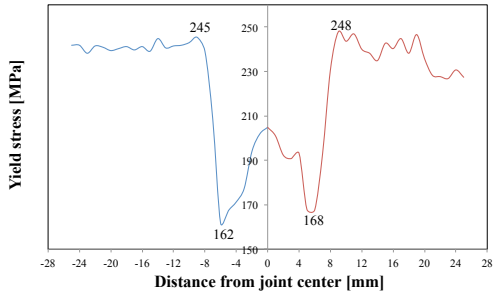

(b) FSW

Figure 5.11: Yield stress profiles based on the GMA and the FS hardness profiles.

Table 5.2 summarizes the base metal yield stress σ_b and the minimum HAZ yield stress σ_{min} found in the yield stress profiles and measured from the tensile testing.

Table 5.2: Summary of the yield stress calculated from the HAZ hardness profiles and measured from the tensile testing of the GMA and the FS welds.

	Yield stress [MPa]			
	From yield stress profiles		**From tensile testing**	
	σ_b	σ_{min}	σ_b	σ_{min}
GMAW	239	131	250	143
FSW	247	165	242	159

From Table 5.2, it is observed that the base metal yield strength σ_b and the minimum HAZ yield strength σ_{min} calculated from the hardness profiles, is in accordance with the yield stress measured for the BM and FZ/SZ the tensile specimens representing the transverse direction. Slightly higher minimum HAZ yield stress σ_{min} can be found for the FS weldments, both from the yield stress profiles and the tensile testing.

Table 5.3 summarizes the total strength reduction in the GMA and the FS weldments. The calculations are based on the yield strength found for the metal yield strenght σ_b and the minimum HAZ yield strength σ_{min} from the yield stress profiles and from the transverse tensile specimens.

Table 5.3: Total strength reduction based on the yield stress found in the yield stress profiles and measured for the tensile specimens representing the transverse direction.

	Strength reduction [%]	
	From yield stress profiles	**From tensile testing**
GMAW	45	43
FSW	33	34

From Table 5.3 it is evident that both welding techniques give a significant strength reduction in the as-welded condition. This must be accounted for in mechanical design.

5.3 Load-bearing capacity of GMA and FS welds

Figure 5.12 shows the assumed dimensions of the AA6082-T6 sheets to be tested subsequent to GMA and FS welding. The figure represents the weldments perpendicular and parallel to the weld.

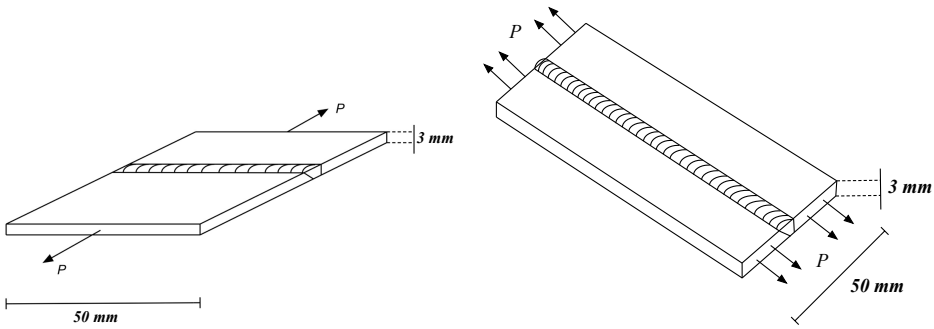

(a) Loading perpendicular to weld **(b)** Loading parallel to weld

Figure 5.12: Assumed dimensions of the AA6082 sheets subsequent to GMA and FS welding, where the loading is perpendicular and parallel to the weld, respectively.

The sheets illustrated in Figure 5.12, together with the base metal yield stress σ_b and the minimum HAZ yield stress σ_{min} from the tensile testing (found in Table 5.2), are being used as a basis in the calculations of load-bearing capacity and the necessary increase in cross-sectional area ΔA.

5.3.1 Loading perpendicular to weld

When the loading is perpendicular to the weld, as shown in Figure 5.12a, the load-bearing capacity can be calculated by inserting the minimum HAZ yield stress σ_{min} and the cross-sectional area (dW) into Equation 2.5. The load-bearing capacity of the GMA and FS weldmenst is 22 (21.5) and 24 (23.9) kN, respectively.

ΔA is the necessary increase in cross-sectional area to maintain the load-bearing capacity after HAZ softening. The general expression for the base metal load is:

$$P = \sigma_b A$$

and from Equation 2.5:

$$P = \sigma_{min} dW = \sigma_{min}(A + \Delta A)$$

which leads to

$$\sigma_{min}(A + \Delta A) = \sigma_b A$$

This in turn, gives the expression for the necessary increase in cross-sectional area ΔA when the loading is perpendicular to the weld:

$$\frac{\Delta A}{A} = \frac{\sigma_b}{\sigma_{min}} - 1 \tag{5.1}$$

When using Equation 5.1, the necessary increase in cross-sectional area for the GMA and the FS weldments becomes 75 and 52%, respectively.

5.3.2 Loading parallel to weld

Figure 5.13 shows the the equivalent half width the reduced strength zone y_{red}^{eq} of minimum strength σ_{min} based on the yield stress profiles of the GMA and the weldments.

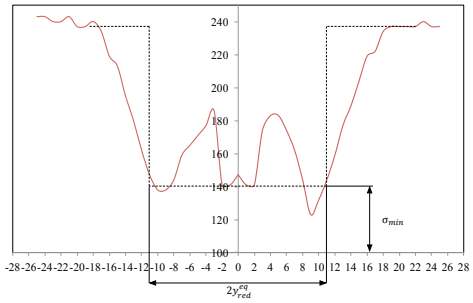

(a) GMAW

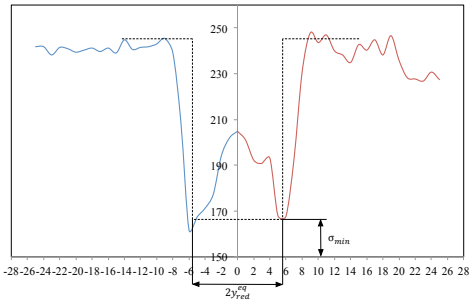

(b) FSW

Figure 5.13: Approximate equivalent half width of reduced strength zone y_{red}^{eq} of minimum strength σ_{min}, based on the yield stress profiles of the GMA and the FS weldments.

From Figure 5.13, the equivalent half width of reduced strength zone y_{red}^{eq} for the GMA and the FS welds corresponds to 11 and 6 mm, respectively. y_{red}^{eq} can be further used when calculating the load-bearing capacity when the loading is parallel to the weld.

When the loading is parallel to the weld, as shown in Figure 5.12b, the load-bearing capacity can be calculated based on the reduced cross-sectional area A_{red}. The values needed for calculating the reduced cross-sectional area A_{red} are summarized in Table 5.4.

Table 5.4: Values to be inserted when calculating the reduced cross-sectional area A_{red}.

	GMAW	FSW
A	150	150
σ_b	250	242
σ_{min}	143	159
y_{red}^{eq}	11	6
β	0.57	0.66

When inserting the values from Table 5.4 into Equation 2.6, the reduced cross-sectional area A_{red} for the GMA and the FS weldments is 122 and 138 mm^2, respectively. The the reduced cross-sectional area A_{red} replaces the cross-sectional area A (dW) from Equation 2.5, and the minimum HAZ yield stress σ_{min} is replaced by the base metal strength σ_b. The load-bearing capacity of the GMA and the FS welds with loading parallel to the weld is 31 (30.5) and 33 (33.4) kN, respectively.

Equation 2.6 is used as a basis when finding the expression for the necessary increase in cross-sectional area ΔA:

$$A_{red} = A - 2y_{red}^{eq}d(1-\beta)$$

and

$$A = A_{red} + \Delta A = dW_0$$

where

$$A_{red} = A_{red} + \Delta A - 2y_{red}^{eq}d(1-\beta)$$

This in turn, gives the expression for the necessary increase in cross-sectional area ΔA when the loading i parallel to the weld:

$$\frac{\Delta A}{A} = \frac{2y_{red}^{eq} d(1-\beta)}{W_0} \tag{5.2}$$

W_0 is the total width of the sheets. When using Equation 5.2, the necessary increase in cross-sectional area for the GMA and the FS weldments becomes 57 and 24%, respectively.

Table 5.5: Summary of the load-bearing capacity and the necessary increase in cross-sectional area ΔA for the GMA and the FS weldments with loading perpendicular and parallel to the weld.

Loading	GMAW	FSW
Perpendicular		
P [kN]	22	24
ΔA/A [%]	75	52
Parallel		
P [kN]	31	33
ΔA/A [%]	57	24

From table 5.5, it is evident that the FS welds exhibit higher capacity compared to the GMA welds, under otherwise identical conditions.

Chapter 6

Conclusion

The results from the hardness, and the mechanical testing can be summarized as follows:

- The results from the hardness testing show that HAZ softening is significant both for the GMA and the FS weldments. Still, the total HAZ width of the FS weldments is much smaller compared to that observed for the GMA weldments. And the FS welds have overall higher strength in the stir zone and the HAZ, compared to that observed in the corresponding zones (fusion zone and HAZ) of the GMA weldments.
- The base metal yield strength σ_b and the minimum HAZ yield strength σ_{min} calculated from the GMA and the FS HAZ hardness profiles, is in accordance with the yield strength measured for the tensile specimens tested transverse to the welding/extrusion direction. The total strength reduction in the GMA and the FS weldments is 43 and 34 $\%$, respectively. This significant strength reduction in the HAZ must be accounted for in mechanical design.
- It has been concluded that the FS weldments in general have slightly better mechanical properties compared to the GMA weldments. And even a small increase in reduction in area can be observed for the FS welds compared to the base metal. From the fracture strain data, it appears that the fracture in the FS cross-weld tensile specimens occur at an earlier point compared to the GMA cross-weld specimens. But the deviations in the strain at fracture measurements must be taken into considerations.
- The FS welds have higher ductility compared to the GMA welds. This is based on the measured reduction in area of the FZ/SZ tensile specimens representing the longitudinal direction, and the energy absorption observed for the welds. In addition, the fracture surfaces of the FS welds is covered with a higher density of small dimples, which in turn is a sign of better ductility.
- The load-bearing capacity has been calculated for the GMA and the FS welds with loading both perpendicular and longitudinal to the weld. The calculated load-bearing capacity for the GMA and the FS welds with loading perpendicular to the weld is 22

and 24 kN, respectively. The corresponding necessary increase in the cross-sectional area ΔA is 75 and 52%, respectively. When the loading is parallel to the weld, the load-bearing capacity of the GMA and FS weldments is to 31 and 33 kN, respectively. The corresponding necessary increase in the cross-sectional area ΔA was 57 and 24%, respectively. This shows that the FS weldments exhibit higher capacity compared to the GMA weldments under identical conditions.

Chapter 7

Bibliography

[1] D.R. Askeland, P.P. Fulay, and W.J. Wright. *The Science and Engineering of Materials*. Cengage Learning, 2010.

[2] O.R. Myhr, A.O. Kluken, S. Klokkehaug, H.G. Fjær, and Ø. Grong. Modeling of microstructure evolution, residual stresses and distortions in 6082-t6 aluminum weldments. *Welding Journal*, 77:286–292, 1998.

[3] A.R. Eivani and A. Karimi Taheri. Modeling age hardening kinetics of an al–mg–si–cu aluminum alloy. *Journal of Materials Processing Technology*, 205(1–3):388 – 393, 2008.

[4] J.R. Davis, J. R. Davis & Associates, and ASM International. Handbook Committee. *Aluminum and Aluminum Alloys*. Asm Specialty Handbook. Asm International, 1993.

[5] Ø. Grong. Recent advances in solid-state joining of aluminum. *Welding Journal*, 91:26–33, 2012.

[6] Ø. Grong. *Metallurgical modelling of welding*. Materials modelling series. Institute of Materials, 1997.

[7] R.R. Ambriz and V. Mayagoitia. *Welding of Aluminum Alloys, Recent Trends in Processing and Degradation of Aluminium Alloys*. InTech, 2011.

[8] R. Kumar, U. Dilthey, D.K. Dwivedi, and P.K. Ghosh. Thin sheet welding of al 6082 alloy by ac pulse-gma and ac wave pulse-gma welding. *Materials and Design*, 30(2):306 – 313, 2009.

[9] R. Liu, Z. Dong, and Y. Pan. Solidification crack susceptibility of aluminum alloy weld metals. *Transactions of Nonferrous Metals Society of China*, 16:110–116, 2006.

[10] C.E. Cross, W.T. Tack, L.W. Loechel, and L.S. Kramer. *Aluminium Weldability and Hot Tearing Theory*, pages 275–282. Asm International, 1990.

[11] K. Prasad Rao, N. Ramanaiah, and N. Viswanathan. Partially melted zone cracking in aa6061 welds. *Materials and Design*, 29(1):179 – 186, 2008.

[12] R. Hermann, S.S. Birley, and P. Holdway. Liquation cracking in aluminium alloy welds. *Materials Science and Engineering: A*, 212(2):247 – 255, 1996.

[13] P.D. Lee, R.C. Atwood, R.J. Dashwood, and H. Nagaumi. Modeling of porosity formation in direct chill cast aluminum–magnesium alloys. *Materials Science and Engineering: A*, 328(1–2):213 – 222, 2002.

[14] P.L. Threadgill, A.J. Leonard, H.R. Shercliff, and P.J. Withers. Friction stir welding of aluminium alloys. *International Materials Reviews*, 54(2):49–93, 2009.

[15] J.E. Hatch. *Aluminum: Properties and Physical Metallurgy*. A S M International, 1984.

[16] O. Reiso and Norges Tekniske Hogskole. *The Effect of Microstructure on the Extrudability of Some Aluminium Alloys*. Doktoravhandling (Norges tekniske høgskole). Norwegian Institute of Technology, 1992.

[17] C. Hsu, K.A.Q. O'Reilly, B. Cantor, and R. Hamerton. Non-equilibrium reactions in 6xxx series al alloys. *Materials Science and Engineering: A*, 304–306(0):119 – 124, 2001.

[18] Sedat Karabay, Muzaffer Zeren, and Muharrem Yilmaz. Investigation extrusion ratio effect on mechanical behaviour of extruded alloy aa-6063. *Journal of Materials Processing Technology*, 135(1):101 – 108, 2003.

[19] N.C.W. Kuijpers, W.H. Kool, and S. Van der Zwaag. Dsc study on mg-si phases in as cast aa6xxx. *Materials Science Forum*, 396-402(2):675–680, 2002.

[20] S. Zajac, B. Bengtsson, and C. Jönsson. Influence of cooling after homogenisation and reheating to extrusion on extrudability and final properties of aa 6063 and aa6082 alloys. *Materials Science Forum*, 396-402(1):399–404, 2002.

[21] Snorre Kjørstad Fjeldbo, Yanjun Li, Knut Marthinsen, and Trond Furu. Through-process sensitivity analysis on the effect of process variables on strength in extruded al–mg–si alloys. *Journal of Materials Processing Technology*, 212(1):171 – 180, 2012.

[22] K.O. Pedersen, O.-G. Lademo, T. Berstad, T. Furu, and O.S. Hopperstad. Influence of texture and grain structure on strain localisation and formability for almgsi alloys. *Journal of Materials Processing Technology*, 200(1–3):77 – 93, 2008.

[23] Y. Chen, K.O. Pedersen, A.H. Clausen, and O.S. Hopperstad. An experimental study on the dynamic fracture of extruded aa6xxx and aa7xxx aluminium alloys. *Materials Science and Engineering: A*, 523(1–2):253 – 262, 2009.

[24] T. Khaled. An outsider looks at friction stir welding. Technical report, 2005.

[25] O.R. Myhr, Ø. Grong, H.G. Fjær, and C.D. Marioara. Modelling of the microstruc-

ture and strength evolution in al–mg–si alloys during multistage thermal processing. *Acta Materialia*, 52(17):4997 – 5008, 2004.

[26] A. Simar, Y. Bréchet, B. de Meester, A. Denquin, C. Gallais, and T. Pardoen. Integrated modeling of friction stir welding of 6xxx series al alloys: Process, microstructure and properties. *Progress in Materials Science*, 57(1):95 – 183, 2012.

[27] Peng Dong, Hongmei Li, Daqian Sun, Wenbiao Gong, and Jie Liu. Effects of welding speed on the microstructure and hardness in friction stir welding joints of 6005a-t6 aluminum alloy. *Materials and Design*, 45(0):524 – 531, 2013.

[28] O.R. Myhr. Welding of aluminium. Lecture at NTNU, 2009.

[29] H. Guo, J. Hu, and H.L. Tsai. Formation of weld crater in gmaw of aluminum alloys. *International Journal of Heat and Mass Transfer*, 52(23–24):5533 – 5546, 2009.

[30] European Aluminium Association. The aluminium automotive manual.

[31] T. Udumphol. The weld microstructure. Lecture at Suranaree University of Technology, 2007.

[32] N. Shanmuga Sundaram and N. Murugan. Tensile behavior of dissimilar friction stir welded joints of aluminium alloys. *Materials and Design*, 31(9):4184 – 4193, 2010.

[33] A. Kostrivas and J.C. Lippold. Fusion boundary microstructure evolution in aluminum alloys. *Welding in the World*, 50(11-12):23–34, 2006.

[34] S.A. David, S.S Babu, and J.M. Vitek. Welding: Solidification and microstrucure. *JOM*, 55(6):14–20, 2003.

[35] O. Runnerstam and K. Persson. The importance of a good quality gas shield. *Svetsaren*, 50(3):24–27, 1995.

[36] P.B. Dickerson. Weld discontinuities - causes and cures. *Welding Journal*, 77(6):37–42, 1998.

[37] A. Farzadi, S. Serajzadeh, and A.H. Kokabi. Investigation of weld pool in aluminum alloys: Geometry and solidification microstructure. *International Journal of Thermal Sciences*, 49(5):809 – 819, 2010.

[38] A. Gutierrez and J.C. Lippold. A proposed mechanism for equiaxed grain formation along the fusion boundary in aluminum-copper-lithium alloys. *Welding Journal*, 77(3):123–132, 1998.

[39] Ø. Grong. Guidance about the report, 2013.

[40] Hidetoshi Fujii, Ling Cui, Masakatsu Maeda, and Kiyoshi Nogi. Effect of tool shape on mechanical properties and microstructure of friction stir welded aluminum alloys. *Materials Science and Engineering: A*, 419(1–2):25 – 31, 2006.

[41] C. Gallais, A. Simar, D. Fabregue, A. Denquin, G. Lapasset, B. Meester, Y. Brechet, and T. Pardoen. Multiscale analysis of the strength and ductility of aa 6056 alu-

minum friction stir welds. *Metallurgical and Materials Transactions A*, 38(5):964–981, 2007.

[42] K.J. Colligan. *Welding Journal*, 78(7):229–237, 1999.

[43] G. Liu, L.E. Murr, C-S. Niou, J.C. McClure, and F.R. Vega. Microstructural aspects of the friction-stir welding of 6061-t6 aluminum. *Scripta Materialia*, 37(3):355 – 361, 1997.

[44] E. Nes and K. Marthinsen. *Modeling the Evolution in Microstructure and Properties During Plastic Deformation of F.c.c.-metals and Alloys: An Approach Towards a Unified Model*, pages 176–193. Elsevier, 2002.

[45] D.A. Price, S.W. Williams, A. Wescott, C.J.C. Harrison, A. Rezai, A. Steuer, M. Peel, P. Staron, and M. Kocak. Distortion control in welding by mechanical tensioning. *Science and Technology of Welding & Joining*, 12(7):620–633, 2007.

[46] H.J. Lui, H. Fuji, M. Maeda, and K. Nogi. *Materials Science and Technology*, 20:103–105, 2004.

[47] J. Altenkirch, A. Steuwer, M. Peel, D.G. Richards, and P.J. Withers. The effect of tensioning and sectioning on residual stresses in aluminium {AA7749} friction stir welds. *Materials Science and Engineering: A*, 488(1–2):16 – 24, 2008.

[48] S. Brinkmann, A. von Strombeck, C. Schilling, J.F. dos Santos, D. Lohwasser, and M. Kocak. Mechanical and toughness properties of robotic fsw repair welds in 6061-t6 aluminium alloys. In *2nd International Symposium on Friction Stir Welding*, 2000.

[49] Grong Ø. Myhr O.R. Novel modelling approach to optimisation of welding conditions and heat treatment schedules for age hardening al alloys. *Science and Technology of Welding & Joining*, 14(4):321–332, 2009.

[50] F. Mazzolani. *Aluminium Alloy Structures*. Taylor & Francis, 2002.

[51] T. Pettersen and T. Furu. Materials certificate for the alloy aa6082: Preparation and characterization of industrial starting material. Technical report, Hydro Aluminium, R&D Materials Technology.

Appendix

Samples for tensile and Charpy V-notch test

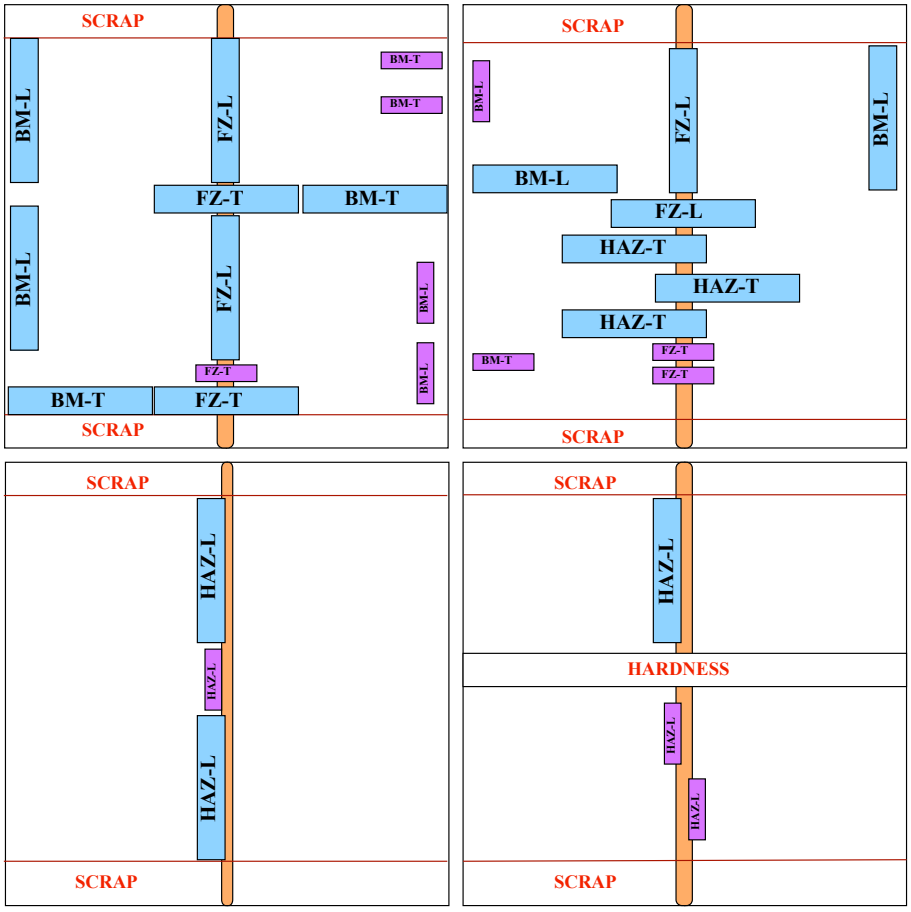

Figure A.1: Location and orientation of specimens used for the tensile and Charpy V-notch testing of the GMAW weldments.

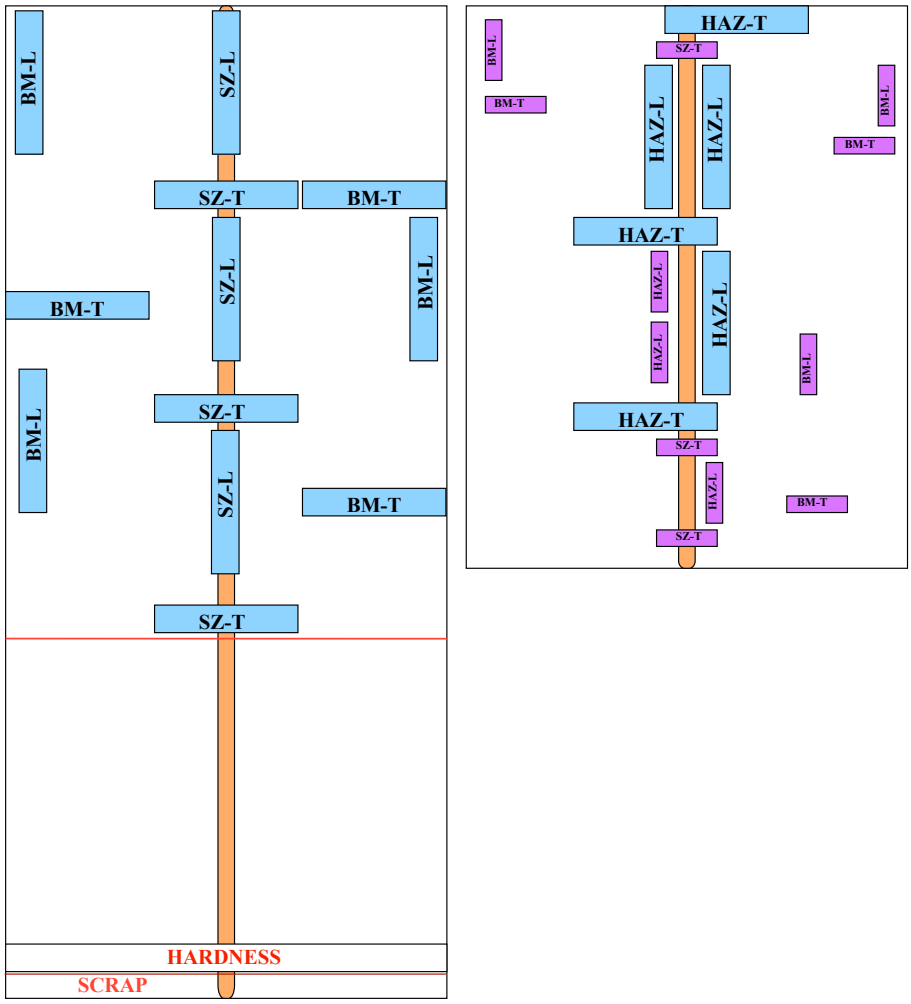

Figure A.2: Location of samples used for the tensile and Charpy V-notch testing of the FS welded plates.

Hardness measurements of the GMA and the FS weldments

Table A.1: Individual hardness measurements of the GMA weldments.

Distance [mm]	Hardness [HV]	Distance [mm]	Hardness [HV]
0	65	0	65
-1	63	1	63
-2	63	2	63
-3	78	3	74
-4	75	4	77
-5	73	5	77
-6	71	6	74
-7	69	7	70
-8	64	8	64
-9	62	9	57
-10	62	10	60
-11	65	11	64
-12	70	12	69
-13	76	13	75
-14	81	14	79
-15	87	15	84
-16	89	16	89
-17	94	17	90
-18	96	18	94
-19	95	19	95
-20	95	20	95
-21	97	21	95
-22	96	22	95
-23	96	23	96
-24	97	24	95
-25	97	25	95

Table A.2: Individual hardness measurements of the FS weldments.

Advancing side		Retreating side	
Distance [mm]	**Hardness [HV]**	**Distance [mm]**	**Hardness [HV]**
0	84.3	0	84.3
-1	83.3	1	83.0
-2	80.7	2	80.1
-3	75.1	3	79.6
-4	73.1	4	80.4
-5	71.8	5	72.0
-6	69.9	6	71.9
-7	85.5	7	80.3
-8	95.7	8	92.9
-9	97.8	9	98.6
-10	97.0	10	97.2
-11	96.6	11	98.3
-12	96.5	12	96.0
-13	96.2	13	95.4
-14	97.6	14	94.3
-15	95.7	15	96.9
-16	96.4	16	96.1
-17	95.9	17	97.6
-18	96.4	18	95.4
-19	96.1	19	98.2
-20	95.8	20	94.6
-21	96.3	21	92.1
-22	96.5	22	91.9
-23	95.4	23	91.6
-24	96.6	24	92.9
-25	96.6	25	91.8

Stress-strain curves and mechanical properties of the GMA weldments

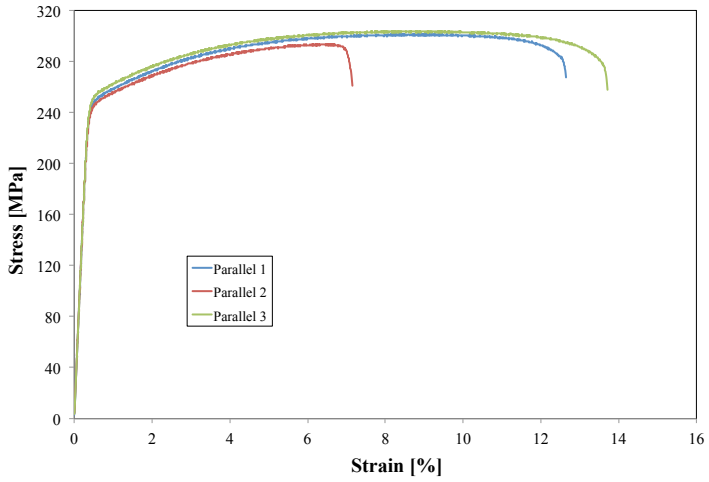

(a)

(b)

Figure A.3: Stress-strain curves for the base metal tensile specimens tested transverse to the extrusion direction. Included is also a macro image of the test specimens subsequent to testing. (Parallel 1 is presented in the report).

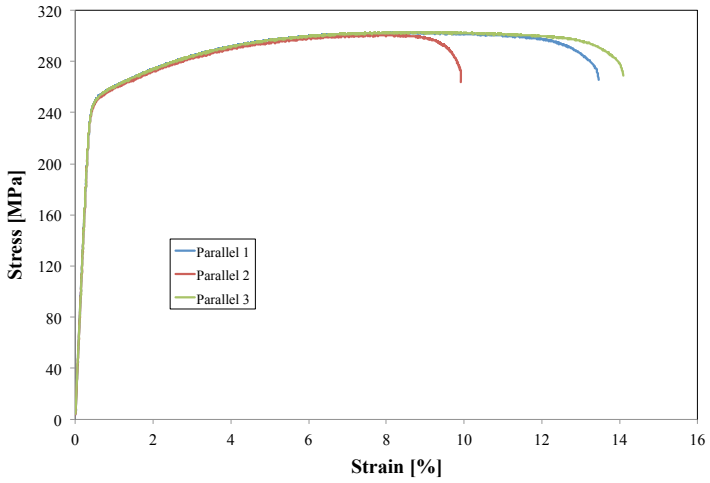

(a)

(b)

Figure A.4: Stress-strain curves for the base metal tensile specimens tested longitudinal to the extrusion direction. Included is also a macro image of the specimens subsequent to testing. (Parallel 1 is presented in the report).

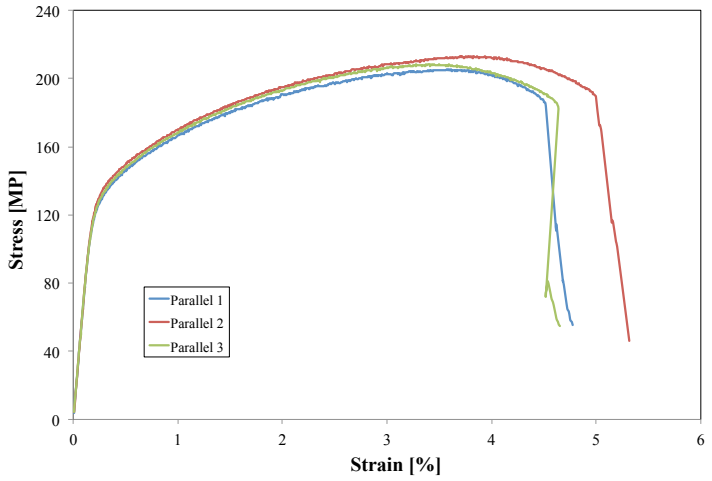

(a)

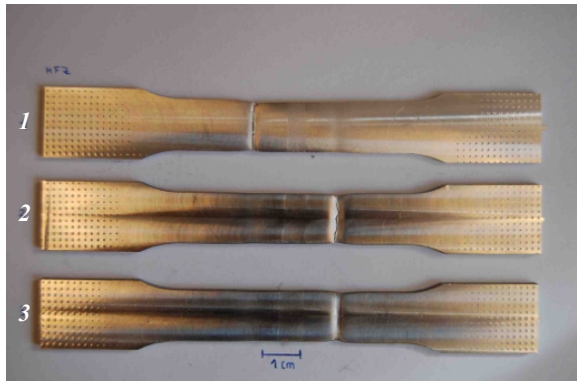

(b)

Figure A.5: Stress-strain curves for the fusion zone tensile specimens tested transverse to the weld. Included is also a macro image of the specimens subsequent to testing. (Parallel 1 is presented in the report).

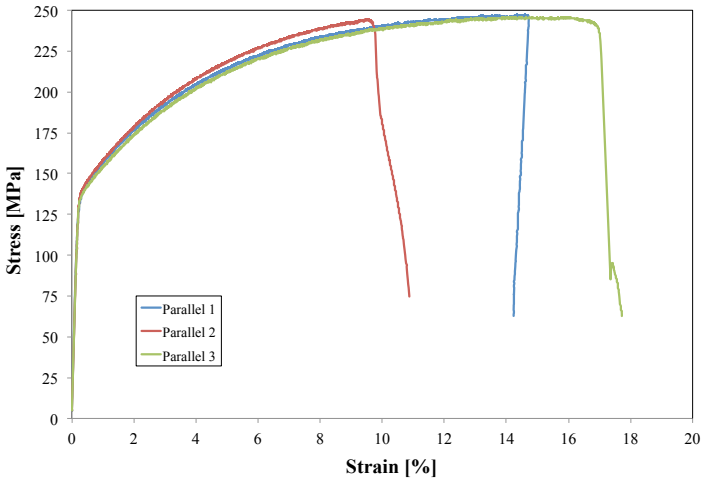

(a)

(b)

Figure A.6: Stress-strain curves for the fusion zone tensile specimens longitudinal to the welding/extrusion direction. Included is also a macro image of the specimens subsequent to testing. (Parallel 1 is presented in the report).

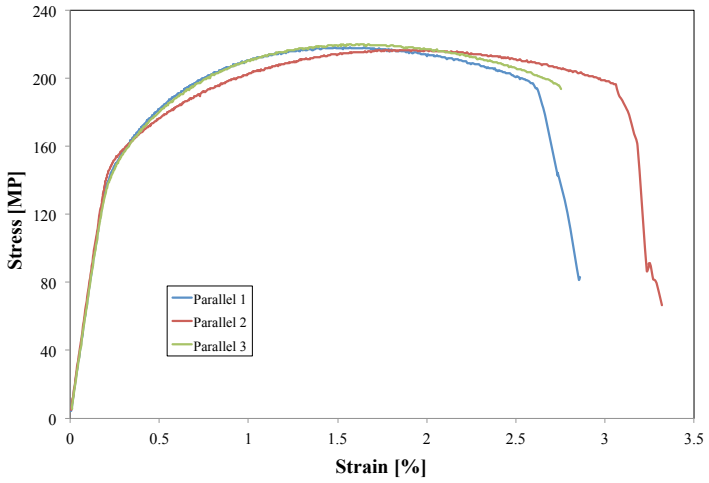

(a)

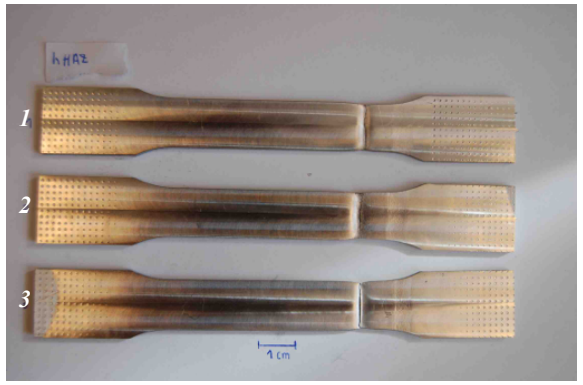

(b)

Figure A.7: Stress-strain curves for the HAZ tensile specimens tested transverse to the welding/extrusion direction. Included is also a macro image of the specimens subsequent to testing. (Parallel 2 is presented in the report).

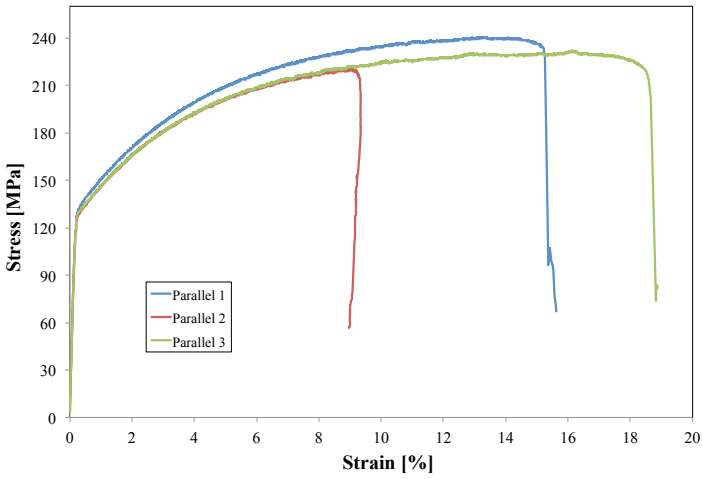

(a)

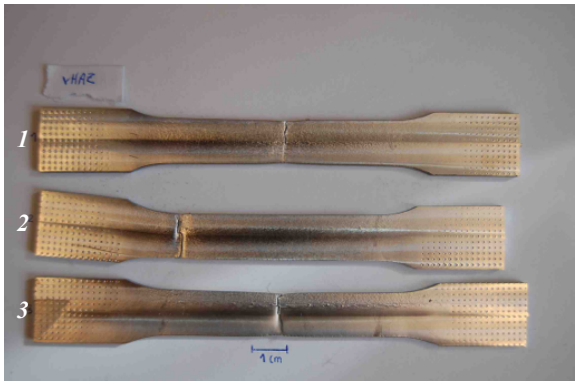

(b)

Figure A.8: Stress-strain curves for the HAZ tensile specimens tested longitudinal to the welding/extrusion direction. Included is also a macro image of the specimens subsequent to testing. (Parallel 1 is presented in the report).

Table A.3: Tensile properties of the GMA weldments.

Location/orientation	Tensile properties [MPa]	
Base metal	**Stress at offset yield**	**Tensile strength**
Transverse	250.0	301.4
	247.1	293.6
	253.8	303.9
Longitudinal	251.4	302.7
	249.5	300.8
	251.5	303.1
Fusion zone		
Transverse	140.6	205.3
	144.9	213.2
	143.1	208.5
Longitudinal	141.5	247.3
	143.3	244.4
	140.1	245.9
HAZ		
Transverse	177.1	218.2
	171.6	216.7
	175.5	220.0
Longitudinal	136.1	240.4
	131.8	220.3
	132.5	232.0

Table A.4: Strain at fracture for the GMA weldments.

Location/orientation	**Strain at fracture [%]**	
Base metal	**Last measured value**	**Defined by extensometer**
Transverse	12.65	...
	7.15	...
	13.71	...
Longitudinal	13.46	...
	9.92	...
	14.10	...
Fusion zone		
Transverse	4.78	4.5
	5.32	5.1
	4.65	4.6
Longitudinal	14.24	14.7
	10.88	...
	17.73	17.1
HAZ		
Transverse	2.86	2.7
	3.32	3.2
	2.75	...
Longitudinal	15.62	15.3
	8.98	9.3
	18.87	18.7

Table A.5: Reduction in area for the GMA weldments, including data for the cross-sectional area before and after testing.

Location/orientation	**Cross-sectional area [mm^2]**		
Base metal	**Before A_i**	**After A_f**	**Reduction in area**
Transverse	38.47	29.41	23.6
	38.73	32.50	16.1
	37.91	27.55	27.4
Longitudinal	38.60	27.08	29.9
	39.28	27.35	30.4
	38.63	28.16	27.1
Fusion zone			
Transverse	24.83	20.73	16.5
	30.86	23.75	23.0
	29.71	22.32	24.9
Longitudinal	25.09	22.01	12.3
	31.15	25.62	17.7
	27.16	20.52	24.5
HAZ			
Transverse	28.78	21.59	25.0
	32.28	24.00	25.6
	28.71	20.74	27.8
Longitudinal	29.84	22.68	24.0
	33.06	25.72	22.2
	33.17	23.54	29.0

Stress-strain curves and mechanical properties of the FS weldments

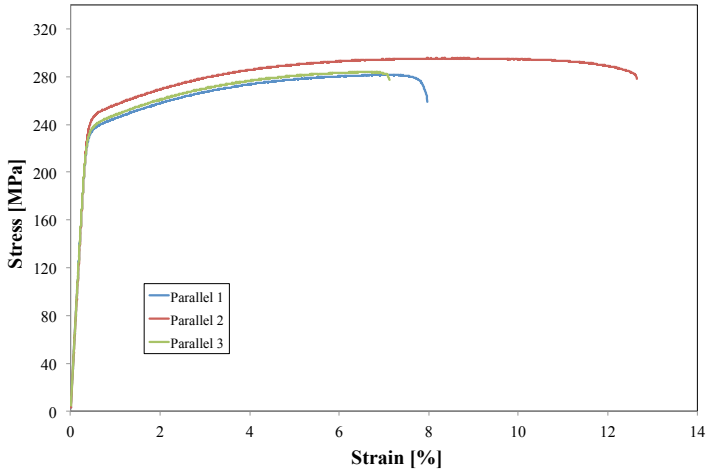

(a)

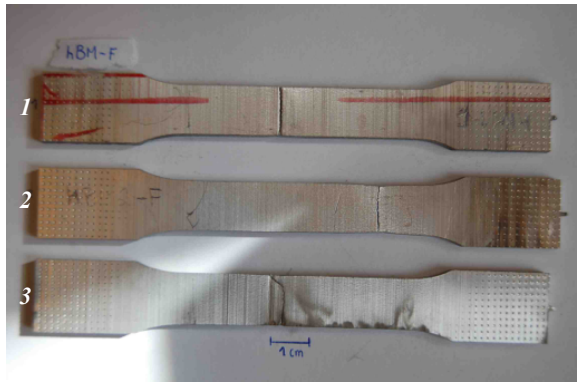

(b)

Figure A.9: Stress-strain curves for the base metal tensile specimens tested transverse to the welding/extrusion direction. Included is also a macro image of the test specimens subsequent to testing. (Parallel 2 is presented in the report).

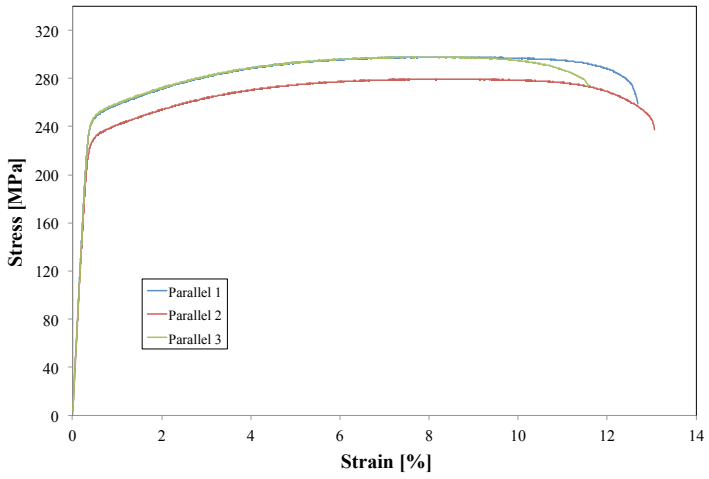

(a)

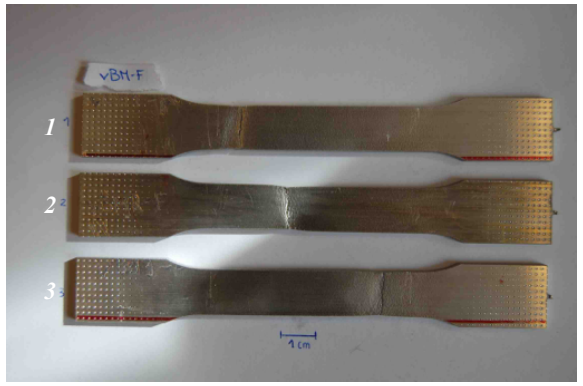

(b)

Figure A.10: Stress-strain curves for the base metal tensile specimens tested longitudinal to the welding/extrusion direction. Included is also a macro image of the test specimens subsequent to testing. (Parallel 1 is presented in the report).

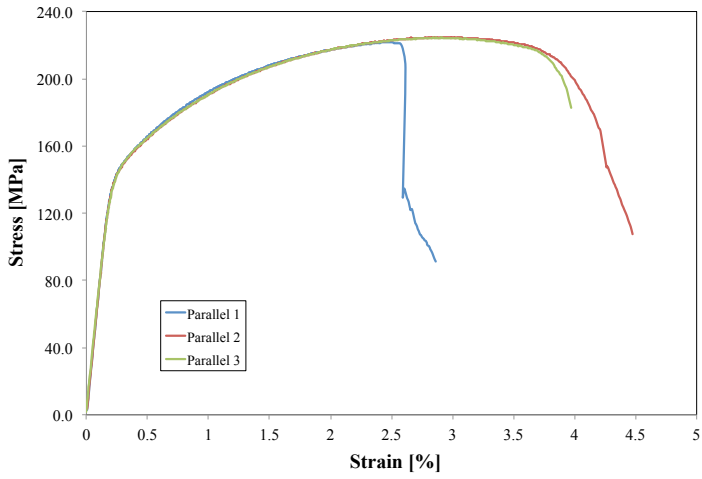

(a)

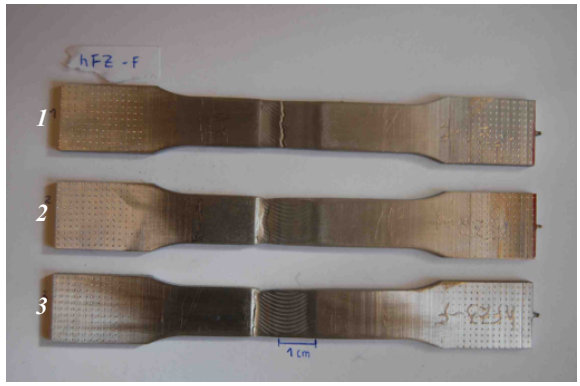

(b)

Figure A.11: Stress-strain curves for the SZ tensile specimens tested transverse to the welding direction. Included is also a macro image of the specimens subsequent to testing. (Parallel 3 is presented in the report)

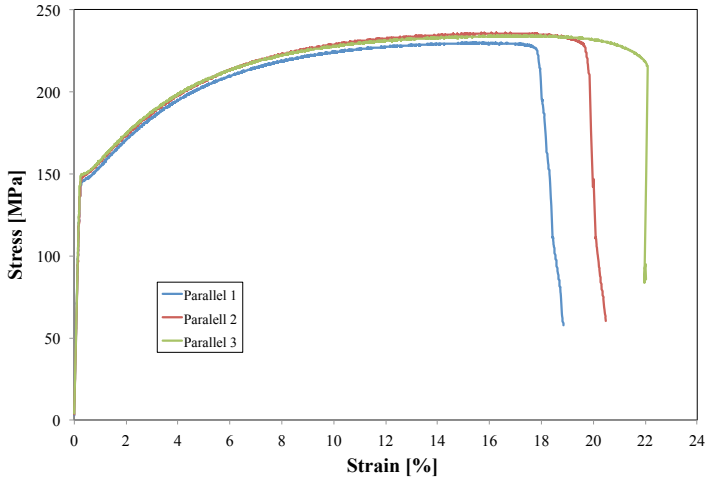

(a)

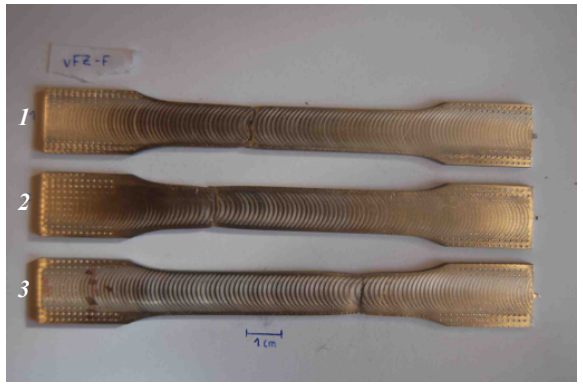

(b)

Figure A.12: Stress-strain curves for the SZ tensile specimens tested longitudinal to the welding direction. Included i also a macro image of the specimens subsequent to testing. (Parallel 2 is presented in the report).

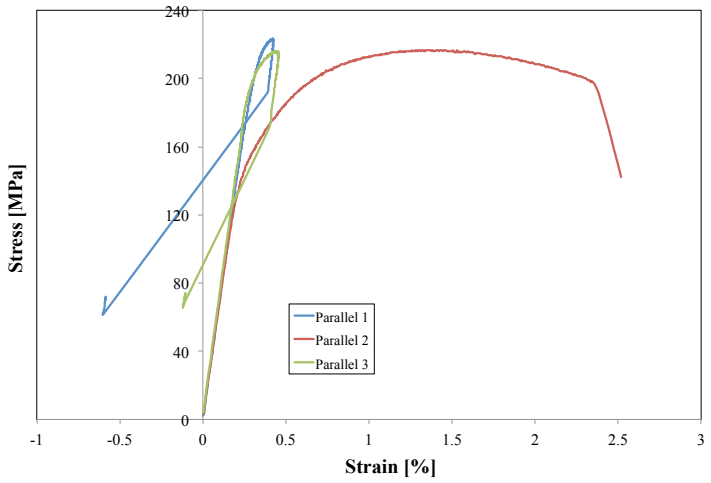

(a)

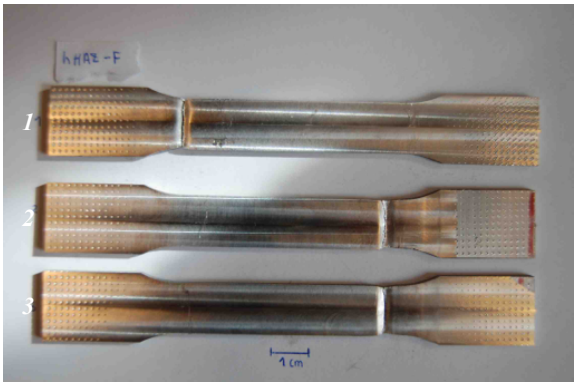

(b)

Figure A.13: Stress-strain curves for the HAZ/TMAZ tensile specimens tested transverse to the welding/extrusion direction. Included is also a macro image of the specimens subsequent to testing. (Parallel 2 is presented in the report).

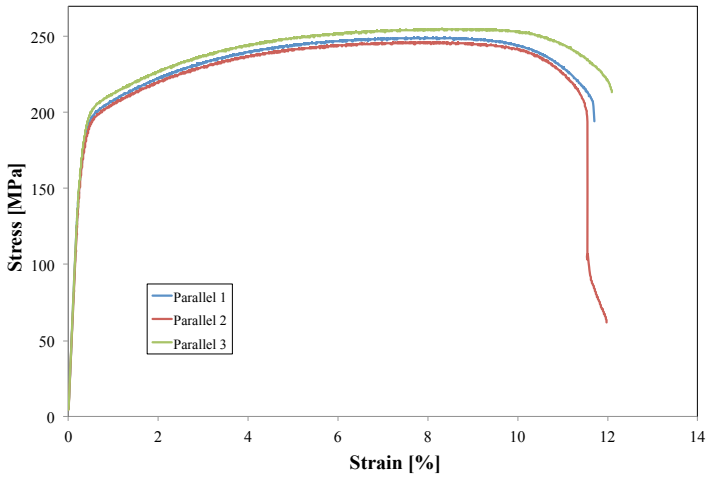

(a)

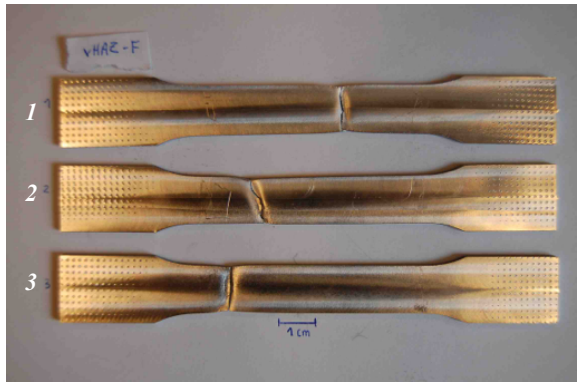

(b)

Figure A.14: Stress-strain curves for the HAZ/TMAZ tensile specimens tested longitudinal to the welding/extrusion direction. included is also a macro image of the specimens subsequent to testing. (Parallel 1 is presented in the report).

Table A.6: Tensile properties of the FS weldments.

Location/orientation	Tensile properties [MPa]	
Base metal	**Stress at offset yield**	**Tensile strength**
Transverse	237.0	281.6
	248.1	295.5
	239.9	284.0
Longitudinal	249.1	298.0
	232.5	279.8
	250.5	297.9
Stir zone		
Transverse	159.1	222.0
	158.2	224.9
	160.0	224.4
Longitudinal	146.3	229.8
	149.3	235.9
	150.4	234.2
HAZ/TMAZ		
Transverse	...	223.5
	182.2	216.7
	...	216.1
Longitudinal	195.0	249.5
	192.8	246.4
	200.0	255.4

Table A.7: Strain at fracture for the FS weldments.

Location/orientation	**Strain at fracture [%]**	
Base metal	**Last measured value**	**Defined by extensometer**
Transverse	7.97	...
	12.66	...
	7.13	...
Longitudinal	12.69	...
	13.06	...
	11.58	...
Stir zone		
Transverse	2.86	2.6
	4.48	4.2
	3.97	...
Longitudinal	18.85	18.4
	20.48	19.8
	22.03	22.1
HAZ/TMAZ		
Transverse	0.39	0.4
	2.52	...
	0.40	0.5
Longitudinal	11.71	...
	11.98	11.6
	12.10	...

Table A.8: Reduction in area for the FS weldments.

Location/orientation	**Cross-sectional area [mm^2]**		
Base metal	**Before A_i**	**After A_f**	**Reduction in area**
Transverse	38.19	31.68	17.1
	38.21	30.66	19.8
	37.89	33.26	12.2
Longitudinal	38.15	31.15	18.4
	38.57	27.69	28.2
	38.47	30.88	19.7
Stir zone			
Transverse	37.26	33.33	10.6
	37.26	28.63	23.2
	37.32	30.12	19.3
Longitudinal	37.90	28.35	25.2
	38.22	25.97	32.1
	37.89	25.56	34.2
HAZ/TMAZ			
Transverse	32.86	23.43	28.7
	32.89	19.74	40.2
	32.33	17.98	44.4
Longitudinal	31.46	17.93	43.0
	29.98	17.18	42.7
	33.18	21.81	34.3

Additional fracture surface images of the GMA tensile specimens

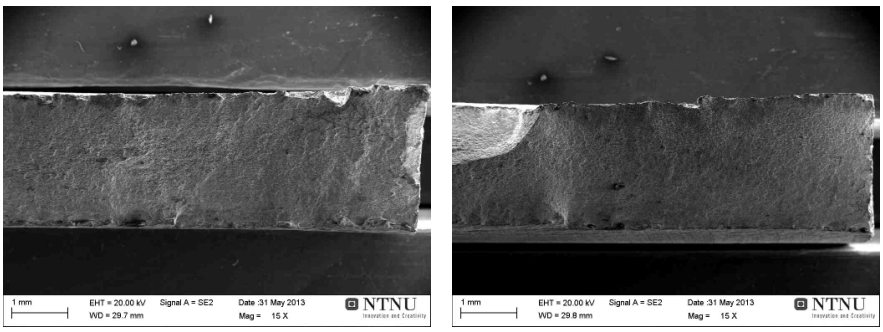

(a) **(b)**

Figure A.15: Additional fracture surface overview of the BM tensile specimens representing the (a) transverse and (b) longitudinal direction.

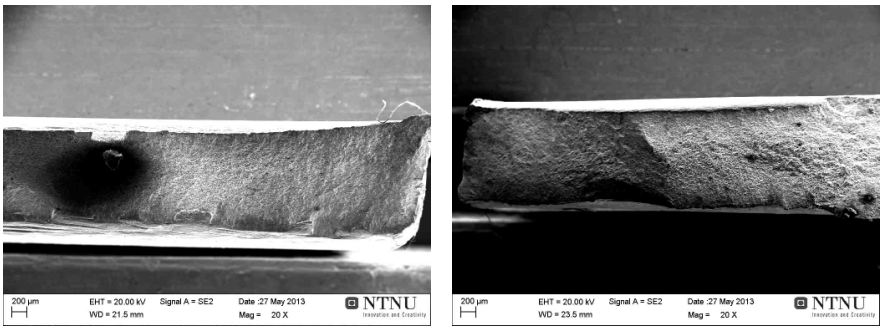

(a) **(b)**

Figure A.16: Additional fracture surface overview of the FZ tensile specimens representing the (a) transverse and (b) longitudinal direction.

Additional fracture surface images of the FS tensile specimens

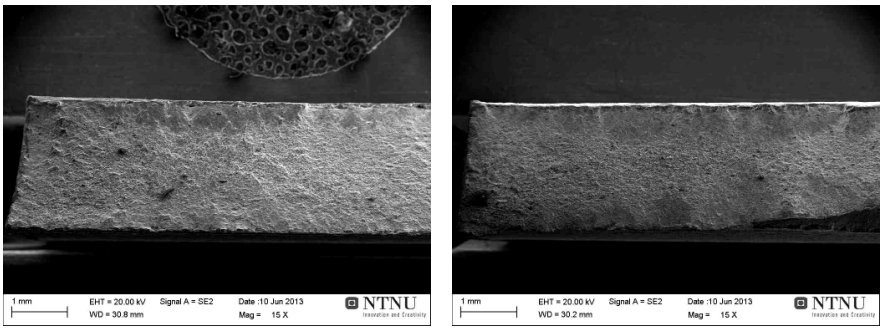

(a) **(b)**

Figure A.17: Additional overview of the BM tensile specimens representing the (a) transverse, and the (b) longitudinal direction.

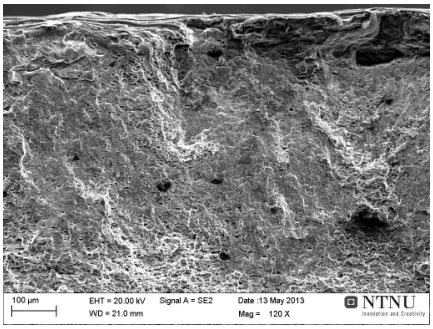

Figure A.18: Surface of the BM tensile specimen representing the transverse direction.

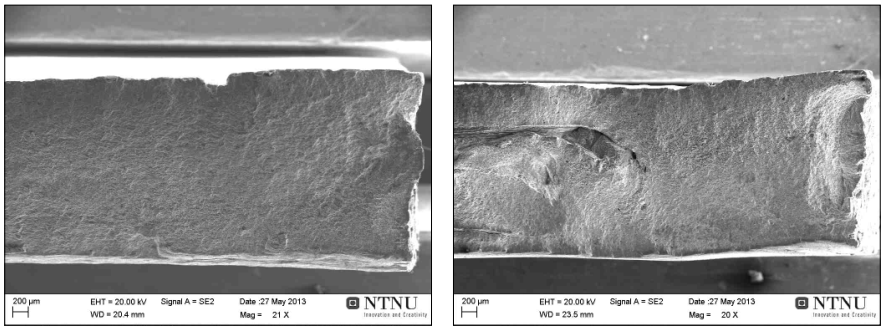

(a) **(b)**

Figure A.19: Additional overview of the SZ tensile specimens representing the (a) transverse, and the (b) longitudinal direction.

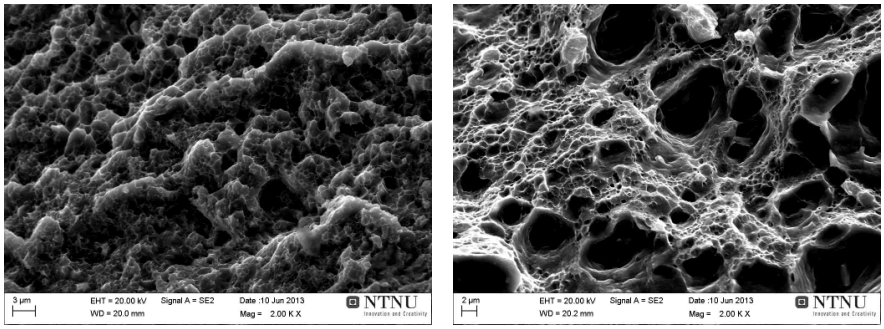

(a) **(b)**

Figure A.20: Additional overview of the fracture surface found in the SZ tensile specimens representing the longitudinal direction.

Charpy V-notch results

Table A.9: Charpy V-notch results for the GMA weldments.

Location/notch orientaion	Energy absorption [J]
Base metal	
Transverse	7.16
	7.25
	5.56
Longitudinal	5.07
	4.98
	4.65
Fusion zone	
Transverse	...
	...
	...
Longitudinal	3.02
	3.42
	3.75
HAZ	
Transverse	4.24
	4.16
	3.91
Longitudinal	...
	...
	...

Table A.10: Charpy V-notch results for the FS weldments.

Location/notch orientation	Energy absorption [J]
Base metal	
Transverse	5.98
	6.32
	5.73
Longitudinal	5.23
	4.57
	4.73
Stir zone	
Transverse	...
	...
	...
Longitudinal	5.73
	5.15
	5.65
HAZ	
Transverse	6.07
	6.74
	6.23
Longitudinal	...
	...

Yield stress calculations based on the HAZ hardness profiles

Table A.11: Calculated yield stress from the GMAW HAZ hardness profiles

From weld center [mm]	Yield Stress [Mpa]	
0	147	147
1	141	141
2	141	141
3	186	174
4	177	183
5	171	183
6	165	174
7	159	162
8	144	144
9	138	123
10	138	132
11	147	144
12	162	159
13	180	177
14	195	189
15	213	204
16	219	219
17	234	222
18	240	234
19	237	237
20	237	237
21	243	237
22	240	237
23	240	240
24	243	237
25	243	237

Table A.12: Calculated yield stress from the FSW hardness profiles.

From weld center [mm]	Yield stress [Mpa]	
0	205	205
1	202	201
2	194	192
3	177	191
4	171	193
5	167	168
6	162	168
7	209	193
8	239	231
9	245	248
10	243	244
11	242	247
12	242	240
13	241	238
14	245	235
15	239	243
16	241	240
17	240	245
18	241	238
19	240	247
20	239	236
21	241	228
22	242	228
23	238	227
24	242	231
25	242	227